Towards an improved Turbulence Closure Scheme by analysing ICON Model Simulations

Inaugural-Dissertation

zur

Erlangung des Doktorgrades
der Mathematisch-Naturwissenschaftlichen Fakultät
der Universität zu Köln

vorgelegt von

Stefanie Neske

aus Großröhrsdorf

Köln, 2017

Berichterstatter: Prof. Dr. Yaping Shao

PD Dr. Hendrik Elbern

Tag der mündlichen Prüfung: 24.04.2017

Simulations are believed by no one except those who conducted them.
Experimental results are believed by everyone except those who conducted them.

— Anonymous

Abstract

With the progress in supercomputer performance, efforts have been made to perform global weather prediction simulations at very high resolutions to reduce model uncertainties by explicitly resolving some of the scales which had to be parameterized before. This potential leads to newly developed models like ICON (**ICO**sahedral **N**onhydrostatic), but their advantages are accompanied by challenges such that the existing parameterizations and well-established schemes may no longer be adequate. The main aim of this thesis is to analyse whether the well-known Smagorinsky turbulence scheme implemented in ICON is scale consistent upon all resolutions and to contribute to an improved closure better suitable for weather and climate prediction with the scale-adaptive grid of the ICON model. To this end, the turbulence scheme is evaluated using ICON model data and further it is examined how subgrid fluxes behave by using methods like wavelet analysis or a direct comparison between modeled parameters and desired parameters.

Two kinds of data sets are used for the analysis. The first one was operated within the framework of the **H**igh **D**efinition **C**louds and **P**recipitation $[HD(CP)^2]$ project. The simulation period was from 24th of April 2013 until 26th of April 2013, whereas the first and the last day serve as representatives for two different weather situations. Three nested domains with different grid resolutions were selected, analysed separately and compared with each other in order to investigate whether the ICON model output is scale dependent or independent. For the second data set, new simulations have been conducted for the 24th April 2013 with an additional higher resolved nesting domain resulting in four resolutions available for comparison.

The analysis of both data sets demonstrates that the turbulence parameterization strongly depends on scale and that the runs on different resolutions substantially disagree in their flux estimates. The results suggest that the closure requires improvement in order to exploit all advantages and new possibilities of the ICON model. Different kinds of analysis methods were used with the focus to better understand the behaviour of the subgrid fluxes. The results point out that eddies of sizes close to the grid scale have the largest influence on the subgrid fluxes. This contradicts the K-theory, which assumes that small eddies have the largest influence on the subgrid flux. Since K-theory is the basis of the closure used in the ICON model and that is also basis of many other closures, this concept has to be questioned. Considering the energy spectrum for turbulence and the grid sizes of the available data sets, points out that the closure probably just captures the smaller scales up to about 200 m grid size. Accordingly, the closure does not seem to be sufficient for most of the resolutions used in this thesis.

As a result of this thesis, two hypotheses for an improved turbulence closure are proposed. An improved closure directly influences the quality of the ICON model weather and climate prediction capability. Furthermore, it can also be a useful enhancement for other scientists to improve weather prediction models.

Zusammenfassung

Der stetige Fortschritt in Computerleistung und -effizienz führt dazu, dass Klimamodellierung in immer höheren Auflösungen durchgeführt wird, um Ungenauigkeiten zu reduzieren und Skalen direkt aufzulösen, die bisher parametrisiert werden mussten. Die neuen Möglichkeiten führen zu neu entwickelten Modellen, wie ICON (**ICO**sahedral **N**onhydrostatic), die neue Herausforderungen an Parametrisierungen und andere standardisierte Prozesse stellen. Deshalb wurde in dieser Arbeit die Smagorinsky Turbulenzparametrisierung analysiert, welche in dem ICON Modell implementiert ist, um zu einer möglichen Verbesserung dessen beizutragen und mit einer skalenunabhängigen Schließung die Wettervorhersagen noch weiter zu optimieren. Dazu wird zunächst die bestehende Parametrisierung anhand von Modelldaten evaluiert und Methoden genutzt, wie zum Beispiel die Wavelet-Analyse oder die direkte Gegenüberstellung von gewünschtem Parameter zu modelliertem Parameter, um die Vorgänge der subskaligen Flüsse besser verstehen zu können.

Zwei verschiedene Datensätze werden für die Auswertung benutzt. Der erste stammt aus einer innerhalb des **H**igh **D**efinition **C**louds and **P**recipitation [$HD(CP)^2$] Projektes durchgeführten Simulation für den 24. bis 26. April 2013, wobei der erste und der letzte Tag sehr unterschiedliche Wettersituationen repräsentieren. Die Simulation besteht aus drei genesteten Gebieten mit unterschiedlichen Gitterauflösungen, die jeweils getrennt voneinander betrachtet und miteinander verglichen werden, um die Skalenabhängigkeit oder -unabhängigkeit des Modells zu untersuchen. Für den zweiten Datensatz wurden neue Simulationen mit Hilfe des ICON Modells für den 24. April 2013 durchgeführt. Diese Simulationen enthalten ein weiteres, noch höher aufgelöstes Modellgebiet, sodass vier unterschiedliche Gitterauflösungen zur Verfügung stehen.

Die Analysen zeigen eine Skalenabhängigkeit der Turbulenzparametrisierung, die verbessert werden sollte, um die neu gewonnenen Möglichkeiten des ICON Modells optimal nutzen zu können und dabei verlässliche Daten zu simulieren. Zur Verbesserung der Schließung wurden einige Untersuchungen mit dem Fokus auf ein besseres Verständnis der subskaligen Flüsse durchgeführt. Die Ergebnisse zeigen, dass die Wirbel, die der Größe der Gitterauflösung am ähnlichsten sind, den größten Einfluss auf den subskaligen Fluss haben. Dies widerspricht der als Grundlage für die Parametrisierung genutzten K-Theorie, welche besagt, dass die kleinen Wirbel den größten Beitrag leisten. Eine zusätzliche Betrachtung des turbulenten Energiespektrums mit einer Größeneinordnung der benutzten Gitterweiten führt zu der Annahme, dass die Schließung nur die kleineren Skalen bis ca. 200 m berücksichtigt, sodass die Schließung in dieser Form nicht ausreichend für die in dieser Arbeit verwendeten Auflösungen zu sein scheint.

Als Resultat dieser Dissertation werden zwei Hypothesen für eine Verbesserung der Turbulenzparametrisierung gefunden. Eine neu angepasste Schließung trägt direkt zur Verbesserung der Klima- und Wettervorhersagen mittels des ICON Modells bei. Eine Verbesserung kann auch auf andere Modelle übertragen werden und demnach auch für andere Wissenschaftler einen hilfreichen und interessanten neuen Ansatz darstellen.

Contents

1 Motivation

Traditional weather and climate models are constructed based on the fundamental assumption that atmospheric motion can be separated into a mean and a turbulent component, or from the numerical perspective, a grid resolved and a subgrid component by means of Reynolds averaging or filtering. Since the grid-resolved scales are directly simulated by the model, subgrid scales have to be parameterized in order to produce a realistic output. Parameterizations of the subgrid components are necessary in order to close the problem of representing these components in general circulation models and directly contribute to high quality model output with an adequate representation of the atmosphere. Thus, parameterizations are of great importance in terms of weather forecasting since they have to represent different scales and phenomena in dependence of grid size and model domain (e.g. topography). For future numerical models, like ICON (**ICO**sahedral **N**onhydrostatic), using unstructured-adaptive grid, the multi-scale modeling capacity strongly depends on scale consistency of subgrid closures and the parameterizations of turbulent fluxes. Heinze et al. [2017] and Milovac et al. [2016] pointed out that parameterizations of land-atmosphere exchanges as well as the planetary boundary layer turbulence are still suffering from significant systematic errors. They also emphasized the need of an investigation and possible improvement of the representation of turbulence and land-atmosphere exchange in weather forecasting models.

Due to progresses in supercomputer performance, efforts have been made to perform global simulations at high resolution to reduce the model uncertainties by explicitly resolving some of the scales which had to be parameterized so far. Much effort on this has been done in the **H**igh **D**efinition **C**louds and **P**recipitation for advancing **C**limate **P**rediction [$HD(CP)^2$] project, in which, i.a., the ICON model is optimized for large eddy simulations. Zängl et al. [2015] prognosed that by the end of this decade, operational numerical weather prediction (NWP) for the globe will reach resolutions for which a non-hydrostatic dynamical core becomes necessary. Up to now, NWP models use a set of governing equations with hydrostatic assumptions, because the scales they represent are coarse enough to assume hydrostatic balance. As a consequence, several research institutions and weather prediction centers have developed or will develop non-hydrostatic global atmospheric models as these will reach mesh sizes of non-hydrostatic scales in the near future. Another result of this development is that future high-performance computing will rely on massively parallel algorithms working on $\mathcal{O}(10^4 - 10^6)$ cores [Zängl et al., 2015]. This pushes aside spectral transform models and regular latitude-longitude grids as they impose limits on scalability because of their need for extensive (global) communication. Some additional reasons, described in more detail in Zängl et al. [2015], lead to more and more global non-hydrostatic models that are based on icosahedral grids and other comparable ones like cubed-sphere grids. Most of the recent developments include means of using non-uniform resolution like grid stretching, mesh refinement, conventional one-way and two-way nesting or related options to be able to run the models on limited-area domains.

As a result, the overall trend for developing new weather prediction models evolves towards unified modeling systems in order to spend the available resources for model development more efficiently and to keep the ever increasing technical complexity of the software infrastructure like I/O and parallelization manageable [Zängl et al., 2015]. Beside the significantly increased progress of the last years, this trend exposes that there is still a limit existing, especially in terms of memory and computer capacity as well as the necessity of further development and a large amount of human power to be invested. Heinze et al. [2017] state numbers of 50 TB (terabyte) model output with 16 TB restart files for one day of simulation with ICON. Output frequencies of 10 seconds up to 1 hour are chosen to cover all 1 D (dimensional) profiles as well as 2 D and 3 D snapshots for an adequate and comprehensive model evaluation. They also emphasize the need of a good scaling behaviour of ICON in order to be able to use the hardware resources of high performance computing (HPC) systems in an optimal way. To this end, a major refactoring of the ICON model code has been executed, at which all global fields were substituted with distributed data structures and by parallelizing the corresponding algorithms [Heinze et al., 2017].

Zängl et al. [2015] tested the non-hydrostatic dynamical core of ICON successfully, Dipankar et al. [2015] and Heinze et al. [2017] evaluated the performance of the ICON model in large-eddy simulation (LES) configuration (called ICON-LEM [Large Eddy Model]) with focus on the comparison with observations and other well-established models. A classical idealized configuration of a dry convective and a cumulus topped boundary layer with doubly periodic horizontal boundary conditions and flat geometries is chosen in case of Dipankar et al. [2015] and a real case configuration with prescribed lateral boundary conditions and a nesting approach is simulated in case of Heinze et al. [2017]. Both found that ICON captures the mean flow characteristics well and some quantities, e.g., the variability of cloud water matches observations better than the reference models. Another purpose of Heinze et al. [2017] was to investigate whether ICON-LEM is able to be a good basis for parameterization development and further improvement of important aspects of processes that have to be parameterized even in a high-resolution setup. Despite some problems with, e.g., too large and too frequent small cumulus clouds, it is concluded that the model is appropriate for parameterization studies due to reliable representation of the mean characteristics, but also needs some further improvements like already stated above. They add the recommendation to use the highest resolution (156 m) when using model output to asses turbulent and moist processes and when evaluating and developing climate model parameterizations since the coarser resolved model variants fail to reproduce aspects of small- to meso-scale variability of moist processes. Furthermore, they found that the peak sensible and latent heat fluxes are considerably higher in the ICON model as in the reference model. Thus, ICON provides more energy input at the surface with an overestimation of about 100-200 Wm^{-2}, which can lead to larger thermals, stronger turbulence and a deeper planetary boundary layer (PBL). Moreover, Heinze et al. [2017] express the need of further improvements at the implementation of the Smagorinsky turbulence closure used in ICON due to overestimation of wind speed for the ICON model, whereas other well-established models show a better performance.

This thesis will contribute to the investigation of the newly developed ICON model in large-eddy simulation configuration with focus on the scale consistency of the Smagorinsky turbulence closure at different resolutions. This is of special interest, because the scale adaptive grid allows a grid refinement during a simulation if, e.g., an area of particular interest is spotted. In order to cope with the changing grid resolution, it would be of great advantage for the turbulence closure to be consistent at the scales used, since different phenomena of different sizes are of importance for the closure depending on the utilized grid size.

ICON model data of two sources are analysed with focus on the scale consistency of the Smagorinsky turbulence closure scheme at different resolutions. As a starting point, data simulated within the framework of $HD(CP)^2$ were investigated, which covers regions over Germany and neighbouring countries for three nested domains. This simulation is called “Status Simulation” and with a time period of three days it is one of the first simulations that was analysed and available for the project members. The second data set used was also conducted with ICON in LES configuration and is based on a similar setup to the one of the “Status Simulation”. Four nested domains were chosen with one more step of grid refinement as was employed for the other data set. Patterns of important and representative quantities like, e.g., potential temperature and vertical velocity are visualized and briefly compared to observations to make sure that the data set used reasonably reproduces the atmosphere. Accordingly, total heat fluxes of all resolutions are examined as representatives for turbulence. Each grid size is analysed separately and afterwards compared against each other in order to asses the scale consistency of the ICON model. Some methods are developed and used to further investigate the turbulent behaviour of subgrid scales for being able to understand the underlying processes that have to be parameterized in a better way. In combination with theoretical considerations, two hypotheses of an improved turbulence closure scheme can be proposed.

The structure of this thesis is as follows: Chapter 2 introduces the general closure problem and gives an overview of the existing closure types. Its structure is based on Stull [1988] and most of the information is extracted from that book. Section 2.3 reveals some specific closures that are of importance for this thesis. The structure of grids and some general information of the ICON model is described in Chapter 3. Section 3.3 gives a more detailed description of the model in its LES mode configuration, because this configuration is used in this thesis. Chapter 4 describes the model data setup, evaluation of the usability of the data together with a short outline of the weather situation during the simulation days. Chapter 5 gives an overview of the methods used during data analysis. Results are given in Chapter 6, which is subdivided in three sections. Section 6.1 deals with the examination of data with respect to model quality in general, whereas Section 6.2 is more specifically concentrating on the model consistency upon different model resolutions. In order to explore the flux behaviour in more detail and to investigate which scales contribute most to the subgrid fluxes, Section 6.3 shows methods like wavelet analysis in combination with theoretical considerations. Based on these, two hypotheses for an improved turbulence parameterization are formulated. Conclusions are given in Chapter 7, which includes a short summary and discussion of the results and an outlook.

2 Closure Theory

2.1 The Closure Problem

The set of governing equations for the atmosphere is well known, but unfortunately they have more unknown variables than equations, primarily due to turbulence. A variable is considered to be unknown if there is no prognostic or diagnostic equation describing it [Pielke, 2002]. Thus, the problem is that this set of fundamental equations is mathematically not closed, otherwise it would be necessary that the number of unknowns equals the number of equations. The result is the need of a closure. Using only a finite number of equations and approximate the remaining unknowns by known quantities is the concept behind closures. These closures are named by the highest order of the prognostic equations that are retained, e.g., first order closure retains the first order moment equation and the second moments are parameterized. Some of the closure approximations utilize only a portion of the equations available within the particular moment category and the result can be classified as half-order closure, one-and-a-half- order closure or zero-order closure, depending on the moment category. For example, if equations for turbulent kinetic energy and temperature and moisture variance are used along with the first moment equations, the result is classified as one-and-a-half-order closure [Stull, 1988].

There are two major closure types that consider the role of small and large eddies in a different way. These types are named as local and nonlocal closures, where none of them are exact, but both seem to work well for the physical tasks for which the parameterizations are designed [Stull, 1988]. A local closure parameterizes an unknown quantity at any point in space by values and/or gradients of known quantities at the same point. Thus, it assumes turbulence to be analogous to molecular diffusion. The nonlocal closure parameterizes the unknown quantity at one point by values of known quantities at many points in space. That means nonlocal closures assume turbulence to be a superposition of eddies, each of them transporting fluid like an advection process [Pielke and Pearce, 1994]. Generally, the higher the order of the local or nonlocal closure is, it yields the more accurate solutions, but is accompanied by added expense and complexity.

In general, a parameterization is an approximation to nature. The aim is to describe a value in nature with some artificially constructed approximation in a hopefully adequate way. This requires human interpretation and creativity, which means that it is possible that different investigators propose different parameterizations for the same unknown quantity. Sometimes, a parameterization is necessary because of the too complicated known physics for some particular application, limited by cost or computer barriers. An other reason to propose a parameterization might be that the true physics have not yet been discovered. There are some rules, which every working parameterization of an unknown has to fulfill [Stull, 1988]:

- the parameterization should be physically reasonable
- it has to have the same dimensions as the unknown
- it has to have the same tensor properties
- it has to have the same symmetries
- it should be invariant under an arbitrary transformation of coordinate systems
- it should be invariant under a Galilean transformation
- it should satisfy the same budget equations and constraints.

2.2 Closure Types

This section gives a short overview of the theory of the many different closure types, subdivided in local and nonlocal closures (cf. Section 2.1). Some specific closures are described in more detail in Section 2.3. They all have their own features and close the governing equations for turbulence in order to be able to do forecasting, diagnostics and many other possible applications.

2.2.1 Zero and half-order Closure

The zero-order closure retains no prognostic equation, not even the equations for mean quantities. They are parameterized directly as a function of space and time. This is neither a local nor a nonlocal closure, because they avoid the parameterization of turbulence entirely. Whereas the half-order closure uses a subset of the first moment equations. A variation of this approximation is the so-called bulk method.

2.2.2 Local Closure — First-order Closure

A first-order closure retains the prognostic equations for the zero-order mean variables such as wind, temperature and humidity in which the unknowns are the second moments. To close the ensued set of equations, turbulent fluxes have to be parameterized. If ξ is any variable that can be separated into a mean and a turbulent component $\xi = \overline{\xi} + \xi'$, one possible first-order closure approximation for the flux $\overline{u'_j\xi'}$ is:

$$\overline{u'_j\xi'} = -K\frac{\partial\overline{\xi}}{\partial x_j}, \tag{1}$$

where the parameter K is a scalar with units m^2s^{-1}. For positive K, the flux flows down the local gradient of $\overline{\xi}$. This parameterization is often called the gradient transport theory or **K-theory**. It is one of the simplest approximations but fails if eddies of large size are present in the flow, hence it is called a small-eddy closure technique. Within this theory, all information about turbulence is included in the turbulent diffusion coefficient, K. Sometimes, different K values are associated with different variables. A subscript m is used for momentum, resulting in K_m as the eddy viscosity. Subscripts K_H and K_E stand for the eddy diffusivities for heat and moisture, respectively. An empirical expression for the relation of these parameters for statistically neutral conditions yields:

$$K_H = K_E = 1.35K_m, \tag{2}$$

at which there is no clear reason why K_m is smaller than the other K-values [Stull, 1988]. But a constant K is not a good approximation to nature, Stull [1988] suggests to parameterize it as a function of known variables like $\overline{\Theta}$, $\overline{U}$ and $\overline{V}$ or of their gradients. There are many existing approaches to determine K, see Section 2.3 for some examples.

As stated in the previous paragraph, the K-theory is not recommended for convective mixed layers where large eddies can transport heat, regardless of local gradients in the background atmosphere [Pielke and Pearce, 1994]. But despite its limitations it is an often used parameterization of turbulent fluxes in meteorological modelling. As a result, there is a large variety of different formulations for the eddy diffusivity, K, respectively adapted to the special applications used. A lot of them are published in literature, e.g., Smagorinsky [1963] and Lilly [1962]. Most of the parameterizations for K are either empirical formulations based on experimental data or semi-empirical formulations which can be derived from prognostic equations for second order moments [Pielke and Pearce, 1994].

Mixing-Length Theory

The mixing-length theory after Prandtl assumes turbulence in a statically neutral environment with a linear mean humidity gradient in the vertical. Due to turbulence, a parcel of air moves upward by an amount z' towards some reference level Z. During this movement there is no mixing or other changes in the value of a property, e.g., humidity, q, within the parcel. The result is a different humidity of the parcel from the surrounding environment. Suppose this difference is q', then:

$$q' = -\frac{\partial \overline{q}}{\partial z} z'. \tag{3}$$

If there is also a linear background mean wind profile, a similar equation can be written for u':

$$u' = -\frac{\partial \overline{U}}{\partial z} z'. \tag{4}$$

The parcel must have had a vertical velocity w' to move upward the distance z' and if the nature of turbulence is such that w' is proportional to u', then it is expected that

$$w' = -cu', \tag{5}$$

for $\frac{\partial \overline{U}}{\partial z} > 0$ and positive for $\frac{\partial \overline{U}}{\partial z} < 0$, with c as a constant of proportionality. Substituting equation (4) in the above expression (5) yields:

$$w' = c \left| \frac{\partial \overline{U}}{\partial z} \right| z'. \tag{6}$$

It shows that the magnitude of the shear seems to be important. The kinematic eddy flux of moisture $R = w'q'$ can be expressed by multiplying equations (3) and (6) and average over the spectrum of different size eddies z':

$$R = -\overline{c(z')^2} \left| \frac{\partial \overline{U}}{\partial z} \right| \left(\frac{\partial \overline{q}}{\partial z} \right). \tag{7}$$

$\overline{(z')^2}$ can be seen as the variance of parcel displacement distance and the square root of it is a measure of the average distance a parcel moves in the mixing process that generated flux R. A mixing length, l, can be defined by $l^2 = \overline{c(z')^2}$. Thus, the moisture flux is calculated as:

$$R = -l^2 \left| \frac{\partial \overline{U}}{\partial z} \right| \left(\frac{\partial \overline{q}}{\partial z} \right). \tag{8}$$

This expression is directly analogous to K-theory if

$$K_E = l^2 \left| \frac{\partial \overline{U}}{\partial z} \right| \tag{9}$$

resulting in

$$R = -K_E \left(\frac{\partial \overline{q}}{\partial z} \right). \tag{10}$$

According to equation (9), mixing-length theory shows that the magnitude of K_E should increase as the shear and the mixing length increases. In this theory, the shear might be a measure of intensity of turbulence and the mixing length is a measure of the ability of turbulence to cause mixing.

The size of turbulent eddies is limited by the earth's surface in the surface layer and therefore it is sometimes assumed that $l^2 = \kappa^2 z^2$, where κ is the von Kármán constant. Following expression results for the surface layer:

$$K_E = \kappa^2 z^2 \left| \frac{\partial \overline{U}}{\partial z} \right| . \tag{11}$$

Another often used expression for the mixing length in a neutral atmosphere is proposed by Blackadar [1962]:

$$\frac{1}{l_N} = \frac{1}{\kappa z} + \frac{1}{l_\infty}, \tag{12}$$

where l_∞ represents the value that is reached in the free atmosphere.

There are some limitations of the relative basic mixing-length theory. Only if turbulence is generated mechanically, the relation between w' and z' can be used. The theory is also limited to a statically neutral atmosphere with linear gradients of wind and moisture. The latter is only given over small distances in the real atmosphere so that the mixing-length theory is only a small-eddy theory.

As pointed out before, the eddy viscosity, K, should not be kept constant, but be parameterized as a function of the flow, in which the parameterization has to satisfy following constraints [Stull, 1988]:

- $K = 0$ where there is no turbulence
- $K = 0$ at the surface ($z = 0$)
- K increases as the average turbulent kinetic energy (TKE), e, increases
- K varies with static stability.

Another constraint, which has to be satisfied only if the analogy with viscosity is used [Stull, 1988], is that K should be non-negative. The normal concept of an eddy-viscosity or small-eddy theory is such that a turbulent flux flows down the gradient and such a transport is associated with positive K values. But in the real atmosphere, it is common that there are occasions in which the transport appears to flow up the gradient (counter-gradient). This could be physically explained by the fact that there are larger eddies associated with the rise of warm air parcels that transport heat from hot surroundings to cold ones, regardless of the local gradient of the background environment. According to this, one has to resort to negative values of K when attempting to use small-eddy K-theory in large-eddy convective boundary layers. Thus, it is not recommended to use K-theory in convective mixed layers.

2.2.3 Local Closure — One-and-a-half-order Closure

This type of closure retains the prognostic equations for the zero-order statistics such as mean wind, temperature and humidity and additionally the variances of those variables. As an example, an idealized scenario of a dry environment, horizontally homogeneous and with no subsidence is considered. The unknowns that arose include second moments, third moments and dissipation. That seems to worsen the problem, but the knowledge of the TKE and temperature variance gives a measure of the intensity and effectiveness of turbulence. Hence, this information could be used within improved parameterizations for the eddy diffusivity $K_m(\overline{e}, \overline{\theta'^2})$. The second correlation terms are approximated as functions of gradients of mean values and the triple correlation terms as functions of second correlations. It can be concluded that a one-and-a-half-order closure is very similar to a first-order closure, they both depend on local gradients and known values. Dissipation rates are sometimes used as a measure of the intensity of turbulence, because the viscous dissipation terms of TKE and temperature variance are modeled as being proportional to their respective variables. More intense turbulence dissipates faster than weaker turbulence.

In most of the resulting sets of possible parameterizations some factors Λ emerge, which are empirical length-scale parameters that are often chosen by trial and error, thus are rather arbitrary. A closure, which avoids the Λ-uncertainty, is the $\overline{e}-\varepsilon$ closure (or $k-\varepsilon$ closure) which avoids the Λ uncertainty by including a highly-parameterized prognostic equation for the dissipation rate in addition to the equation for the TKE. Within this closure the equation for K containing Λ is parameterized in following way:

$$K = \frac{c_{\varepsilon_5}\overline{e}}{\varepsilon}, \tag{13}$$

with $c_{\varepsilon_5} = 0.3$. Examples for the use of this closure assumption are simulations of boundary layer evolution, flow over changing roughness and topography and sea-breeze fronts [Stull, 1988]. Advantages of higher-order closures are that they create nearly well-mixed layers during the daytime which increase in depth with time. At night, there is a development of a stable layer near the ground with nocturnal jet formation. Results also show that the turbulence intensity increases to large values during the day and smaller ones at night. There are some limitations of this assumption, namely that it provides no information on turbulence intensity or temperature variance. Furthermore, it has difficulties with well mixed layers that have zero gradients of mean variables.

2.2.4 Local Closure — Second-order Closure

The set of retained equations in the second-order closure contains those from the one-and-a-half-order assumption and moreover, second moment terms. Thus, appearing third-order moments have to be parameterized. If the same idealized example as in the case of one-and-a-half-order closure is used, the unknowns include pressure-correlation terms, third moments and dissipation terms. When using the full second-order set of equations, they could produce forecasts of mean variables and variances with a better accuracy as the first order and the one-and-a-half-order closure. And more importantly, they could also produce forecasts of fluxes and other covariances that the lower order schemes can not forecast.

2.2.5 Local Closure — Third-order Closure

For this type of closure, prognostic equations for the triple-correlation terms are retained, while parameterizations have to be found for the fourth-order correlations, the pressure-correlations and for viscous dissipation. Generally, it is assumed that equations for lower-order variables become more accurate as higher the closure approximation is. But higher-order moments are extremely difficult to measure in the real atmosphere, so there is just a little knowledge of how these moments behave. Thus, it is really hard to suggest a good closure and ends up with the result of crude approximations in third-order closure models.

2.2.6 Nonlocal Closure — Transilient Turbulence Theory

Nonlocal closure considers the concept of larger-size eddies to transport fluid across finite distances before the smaller eddies have the chance to cause mixing.

For a better understanding of the transilient turbulence theory, a one-dimensional column of air is imagined, which is separated into equally sized grid boxes. A superposition of eddies causes mixing between all the boxes. There is a reference box i with an average concentration of passive tracer, $\overline{\xi_i}$. If c_{ij} represents the fraction of air in box i that came from box j during a time interval Δt, one can find the new concentration in box i by summing up the mixing from all N grid boxes in the column:

$$\overline{\xi_i}(t+\Delta t) = \sum_{j=1}^{N} c_{ij}(t,\Delta t)\overline{\xi_j}(t). \tag{14}$$

c_{ij} is an $N \times N$ matrix of mixing coefficients and is called a transilient matrix. During the movement of the parcels from one grid to another, the air will not only carry the tracer concentration with it, but also heat, momentum, moisture and other measures of the state of the fluid. Hence, equation (14) could be used for any of these variables with unchanged transilient matrix and different $\overline{\xi_j}$. Each of the elements should be $0 \leq c_{ij} \leq 1$ and each row and column of the matrix must sum up to one. A numerical forecast based on transilient turbulence theory is absolutely numerical stable for any time step size and grid spacing. The unknowns for this problem are the c_{ij} coefficients that have to be parameterized. Two closure assumptions have been used to solve this problem in literature: first, the a priori method that utilizes knowledge or assumptions about the frequency distribution of turbulent velocities or about the turbulence spectrum. The second one is a responsive approach in which the transilient coefficients change in response to changes in the mean flow [Stull, 1988].

2.2.7 Nonlocal Closure — Spectral Diffusivity Theory

Starting point of this theory is the approximation of the flux $\overline{w'\xi'}$ by K-theory and then put this definition into the conservation equation for a passive tracer. The assumption is that K is independent of z and varies with eddy size. With k as wavenumber of the eddy, the spectral decomposed diffusion equation yields:

$$\frac{\partial\overline{\xi}(k)}{\partial t} = K(k)\frac{\partial^2\overline{\xi}(k)}{\partial z^2}, \tag{15}$$

where $K(k)$ is called spectral turbulent diffusivity. The turbulent diffusivity transfer function $\Xi(z, Z, t)$ is defined as:

$$\Xi(z, Z, t) = \frac{1}{2\pi}\int_{-\infty}^{+\infty} K(k, t)exp[ik(z - Z)]\,dk, \tag{16}$$

for mixing between level Z and level z, which is the point of interest. For this closure, the unknowns are either $K(k)$ or Ξ. A possible parameterization could be an a priori approach like used by Berkowicz and Prahm [1979] [Stull, 1988].

2.3 Specific Closures

After the rather general information about closures in Section 2.2, this section is about specific closures which can be classified into the above described types of approaches and are of special importance for this thesis. They are developed for certain conditions and often extended because of improved knowledge or computer performance.

2.3.1 Smagorinsky Scheme

The Smagorinsky scheme [Smagorinsky, 1963] is a commonly used parameterization scheme which is implemented in ICON (with the stability extension due to Lilly (1962), see Section 2.3.2). It is a first-order turbulence closure scheme using eddy viscosity coefficients proposed by Smagorinsky in 1963 to describe the unresolved (subgrid) scales. This closure is based on the assumption that production of subgrid scale turbulent kinetic energy and dissipation of isotropic turbulence energy are in balance at the characteristic eddy size [Germano et al., 1991].

Starting point for the Smagorinsky scheme is the filtered Navier-Stokes equation, which can be written as

$$\frac{\partial \overline{u_i}}{\partial t} + \frac{\partial}{\partial x_j}(\overline{u}_i\overline{u}_j) = -\frac{1}{\rho}\frac{\partial \overline{p}}{\partial x_i} + \frac{1}{\rho}\frac{\partial \tau_{ij}^R}{\partial x_j} + \nu\nabla^2\overline{u_i}, \tag{17}$$

with

$$\nabla^2\overline{u_i} = \Delta\overline{u_i} = \frac{\partial^2\overline{u_i}}{\partial x_i^2} \tag{18}$$

and

$$\tau_{ij}^R = \rho(\overline{u}_i\overline{u}_j - \overline{u_i u_j}) \tag{19}$$

as the so called residual stress tensor that only results out of the applied filter. The Einstein summation convention applies to repeat indices [Dipankar et al., 2015]. The filtered equation now only contains eddies of size L (filter width) and above, such that equation (17) is integrated on a grid of size $\sim L$. Only the unresolved scales remain to be parameterized with an eddy-viscosity model. The residual stress tensor can be written as (for further details see Davidson [2004]):

$$\tau_{ij}^R = 2\rho K\overline{D}_{ij} + \frac{1}{3}\delta_{ij}\tau_{kk}^R, \tag{20}$$

with K as the eddy viscosity of the residual motion and $\overline{D}_{ij}$ is the averaged strain-rate tensor. $\overline{D}_{ij}$ can be calculated with the help of the grid-scale strain rate [Langhans et al., 2011]:

$$D_{ij} = \frac{1}{2}\left(\frac{\partial u_i}{\partial x_j} + \frac{\partial u_j}{\partial x_i}\right), \tag{21}$$

with u_i as the large-scale velocity. Applying equation (20) into equation (17) yields to:

$$\frac{\partial \overline{u}_i}{\partial t} + \frac{\partial}{\partial x_j}(\overline{u}_i \overline{u}_j) = -\frac{1}{\rho}\frac{\partial \overline{p}^*}{\partial x_i} + 2\frac{\partial}{\partial x_j}[(\nu + K)\overline{D}_{ij}], \tag{22}$$

with $\overline{p}^*$ as a modified pressure.

The remaining quantity to parameterize in equation (22) is K. On basis of physical arguments, it is assumed that the most energetic eddies of the unresolved scale are those of a scale comparable to L. Due to dimensional reasons a description for K should be [Davidson, 2004]:

$$K \sim L(v_L^2)^{1/2}, \tag{23}$$

where $(v_L^2)^{1/2}$ is the kinetic energy of eddies of size L. Smagorinsky now takes this kinetic energy as the order of $L^2(\overline{D}_{ij}\overline{D}_{ij})$ and introduces a dimensionless constant, c_s, which yields to:

$$K = c_s^2 L^2 (2\overline{D}_{ij}\overline{D}_{ij})^{1/2}. \tag{24}$$

c_s is an empirical non-dimensional constant at grid-scale with a value of ~ 0.1. With the help of equation (24), e.g., the parameterized fluxes can be calculated like described in Section 2.2.2 for a first order closure.

2.3.2 Lilly's extension of the Smagorinsky Scheme

Lilly [1962] extended the above described closure scheme of Smagorinsky (cf. Section 2.3.1) by taking also buoyancy production or consumption into account when looking at the subgrid energy balance. Thus, it can describe turbulence in unstably stratified atmospheric boundary layers. The inclusion of the stratification effect is done by adding a new parameter, the flux Richardson number, in the calculation of the eddy viscosity [Young et al., 2003]. The flux Richardson number (Ri_f) is defined as the ratio between the subgrid buoyant energy production to the rate of mechanical production of subgrid energy [Mason, 1989] and can be written as:

$$Ri_f = \frac{\frac{g}{\theta_v}(\overline{w'\theta_v'})}{(\overline{u'w'})\frac{\partial \overline{U}}{\partial z} + (\overline{v'w'})\frac{\partial \overline{V}}{\partial z}}, \tag{25}$$

with θ_v as virtual temperature and the assumption of horizontal homogeneity and neglected subsidence. Different values of Ri_f indicate different stratification:

- $Ri_f > 0$ indicates a statically stable stratified layer
- $Ri_f < 0$ indicates a statically unstable stratified layer
- $Ri_f = 0$ is a neutral stratification.

Implementing this flux Richardson number into the Smagorinsky scheme yields the expression for Lilly's eddy viscosity:

$$K = \lambda^2 D_{ij}(1 - Ri_f)^{1/2}, \tag{26}$$

with λ as a length scale, which depends on the grid-scale and the Smagorinsky constant c_s.

Within this formulation, Lilly also showed the former new idea that the Smagorinsky coefficient, c_s, could be related to the phenomenology of three-dimensional homogeneous isotropic turbulence, meaning to determine this value [Huang et al., 2007]. How to compute the coefficients can be, e.g., seen in Bou-Zeid et al. [2008], where also the dependence of the coefficients as a function of scale is analysed.

2.3.3 Dynamic Smagorinsky Model

Germano et al. [1991] introduced a formulation of the Smagorinsky constant, c_s (cf. Section 2.3.1), where it is no longer a constant and defined as a function of position and time by using information about local flow conditions. To this end, two filters with different width are necessary, a grid- and a test-filter, whereat the test-filter must be greater than the grid-filter. A subgrid scale stress tensor, τ_{ij}, is defined which has to be modeled to account for the effects of the small scales:

$$\tau_{ij} = \overline{u_i u_j} - \overline{u}_i \overline{u}_j. \tag{27}$$

The closure for the grid-filter can be written as:

$$\tau_{ij} - \frac{1}{3}\delta_{ij}\tau_{kk} = -2c_s^2 \overline{L}^2 |\overline{D}| \overline{D}_{ij}, \tag{28}$$

with $|\overline{D}| = (2\overline{D}_{mn}\overline{D}_{mn})^{1/2}$ (cf. Section 2.3.1).

The same is done for the test-filter, which is indicated by a tilde ($\sim$), and with the subgrid stress of the test-filter, $T_{ij} = \widetilde{\overline{u_i u_j}} - \tilde{\overline{u}}_i \tilde{\overline{u}}_j$, follows:

$$T_{ij} - \frac{1}{3}\delta_{ij}T_{kk} = -2c_s^2 \widetilde{\overline{L}}^2 |\widetilde{\overline{D}}| \widetilde{\overline{D}}_{ij}, \tag{29}$$

with $|\widetilde{\overline{D}}| = (2\widetilde{\overline{D}}_{mn}\widetilde{\overline{D}}_{mn})^{1/2}$ and $\widetilde{L}^2$ the test- filter scale. Consistency between equation (28) and equation (29) depends on a proper local choice of c_s [Lilly, 1992], which can be shown by subtracting the test-scale average of the grid-filter stress from T_{ij}, called the resolved turbulent stress $\mathcal{L}$:

$$\mathcal{L}_{ij} = T_{ij} - \widetilde{\tau}_{ij}. \tag{30}$$

Contracting this with $\overline{D}_{ij}$ and inserting equation (28) and equation (29) into equation (30) yields:

$$\mathcal{L}_{ij}\overline{D}_{ij} = -2c_s(\widetilde{\overline{L}}^2 |\widetilde{\overline{D}}| \widetilde{\overline{D}}_{ij}\overline{D}_{ij} - \overline{L}^2 |\widetilde{\overline{D}}| \widetilde{\overline{D}}_{ij}\overline{D}_{ij}), \tag{31}$$

showing that $c_s(x, y, z, t)$ is the remaining unknown and is only a function of y and t for the channel flow [Germano et al., 1991].

This model requires the use of spatial averaging to sustain c_s values within a realistic range, what limits its application to flows over complex realistic surfaces [Huang et al., 2007]. It also assumes scale invariance of the coefficient, c_s, which means that it does not depend on filter-scale. But the advantage of this dynamical model is that it uses the resolved scales to obtain the model coefficient during the simulation and thus avoiding to prescribe or tune the coefficient like it is done in many other models [Meneveau and Katz, 2000].

3 ICON Model

The development of the **ICO**sahedral **N**on-hydrostatic general circulation model (ICON) was initiated by the Max Planck Institute for Meteorology (MPI-M) and the German Weather Service (DWD). It is a unified modeling system for climate and weather forecast with the purpose to better utilize the potential of new generations of high performance computing, to represent the increasingly important fluid conservation properties better, to provide a more consistent basis for coupling atmosphere and ocean as well as representing subgrid-scale heterogeneity over land and to allow regionalization and limited area implementations. Particularly, the ICON dynamical core solves the fully compressible non-hydrostatic governing equations for simulations at very high horizontal resolution [Giorgetta and Korn, 2015]. ICON offers three basic packages:

1. Climate modelling
2. Numerical weather prediction (NWP)
3. Large-eddy simulations (LES), called ICON-LEM (Large Eddy Model).

Packages 1. and 2. were designed for subgrid-scale processes on scales of hundreds of kilometers up to about tens of kilometers and were the first operative packages of ICON. Using ICON at scales of $\mathcal{O}(100m)$ needed a new LES package which has been added to the model. ICON was developed towards LES applications mainly within the framework of the $HD(CP)^2$ project in order to improve the understanding of cloud and precipitation processes and their implications for climate predictions better by utilizing very high (horizontal spacing of up to $\sim$ 100 m) resolution and thereby resolving processes which had to be parameterized until then. Some additional aims were the improvement of ground, in situ and satellite based observations of cloud and precipitation events in order to evaluate the model. The project is now on its second phase and the focus changed towards using the former developed LES package. With the help of new results, the project tries to answer questions related to cloud formation, investigation of the controlling factors for boundary layer clouds and to explore to what extend convective organization is important for climate (see the project webpage $HD(CP)^2$ [2016] for more details). Dipankar et al. [2015] found that ICON, as being a unified modeling system, undergoes some compromises in the LES configuration (cf. Section 3.3) in comparison to well-established LES models like the PArallelized Large eddy simulation Model (PALM) [Raasch and Schröter, 2001] or UCLA-LES (University of California, Los Angeles = UCLA) [Stevens et al., 2005]. ICON-LES is mostly second-order accurate in space whereas the others are fifth-order accurate in numerics, but it has a fairly good eddy-resolving capability [Dipankar et al., 2015]. The mean flow characteristics are captured satisfactorily by the turbulence scheme.

ICON went operational as global numerical weather prediction model at the DWD in 2015 and they are one of only fourteen weather services of the world using a global NWP model [Deutscher Wetterdienst, 2016b]. Furthermore, many external users employ ICON forecasts as basis for their products, e.g., regional hydrological offices use precipitation fields for flood forecasting, and others use them as lateral boundary conditions for limited-area forecasts.

All the equations employed in ICON are based on the prognostic variables suggested by Gassmann and Herzog [2008] and the two-dimensional Lamb transformation is used to convert the nonlinear momentum advection into a vector-invariant form [Zängl et al., 2015]. The prognostic variables are the horizontal velocity component normal to the triangle edges (v_n), the vertical wind component (w), density (ρ), the density potential temperature (θ_ρ), which is also referred to as virtual potential temperature (θ_v) and the specific masses and number densities of tracers q_i, with $i = 1, 2, .., N_t$ and N_t as the total number of tracers, which depends on the microphysics scheme used. The tracers include, e.g., water vapor (q_v), liquid water (q_l) and snow (q_s). When coupled with moisture physics, ρ is the full air density including liquid and solid condensates and θ_ρ is calculated in the following way:

$$\theta_\rho = T_\rho \left(\frac{p_{00}}{p}\right)^{\frac{R_d}{c_{pd}}} = \frac{T_\rho}{\Pi}. \tag{32}$$

p_{00} is the reference pressure, Π the Exner function and $T_\rho = T\alpha$ the density temperature with:

$$\alpha = [1 + \left(\frac{R_v}{R_d} - 1\right) q_v - q_c], \tag{33}$$

where q_c is the contribution due to liquid and solid condensates, R_d and R_v are gas constants for dry air and water vapor, respectively, and c_{pd} is the isobaric specific heat capacity of dry air.

The basic equation system used in ICON is the following [Zängl et al., 2015]:

$$\frac{\partial v_n}{\partial t} + \frac{\partial K_h}{\partial n} + (\zeta + f)v_t + w\frac{\partial v_n}{\partial z} = -c_{pd}\theta_v \frac{\partial \Pi}{\partial n} + F(v_n), \tag{34}$$

$$\frac{\partial w}{\partial t} + \boldsymbol{v_h} \cdot \nabla w + w\frac{\partial w}{\partial z} = -c_{pd}\theta_v \frac{\partial \Pi}{\partial z} - g, \tag{35}$$

$$\frac{\partial \rho}{\partial t} + \nabla \cdot (\boldsymbol{v}\rho) = 0, \tag{36}$$

$$\frac{\partial \rho\theta_v}{\partial t} + \nabla \cdot (\boldsymbol{v}\rho\theta_v) = \tilde{Q}, \tag{37}$$

with $K_h = \frac{1}{2}(v_n^2 + v_t^2)$ the horizontal part of the kinetic energy per mass unit and v_t as the reconstructed tangential velocity component. $\boldsymbol{v_h}$ and $\boldsymbol{v}$ denote the horizontal and full three dimensional velocity components, respectively, ζ is the vertical vorticity component, f the Coriolis parameter and g the gravitational acceleration. $\frac{\partial}{\partial n}$ denotes a horizontal derivative in the edge-normal direction, i.e., between two adjacent mass points. Furthermore, $F(v_n)$ denotes source terms for horizontal momentum and $\tilde{Q}$ is an appropriately formulated diabatic heat source term. Full details of the set of equations can be seen in Zängl et al. [2015] and Wan et al. [2013].

The three dimensional spherical grid of ICON consists of the horizontal grid (see Section 3.1) and the vertical grid (see Section 3.2). Whereas the horizontal grid discretizes the sphere surface on a triangular or hexagonal grid, a set of horizontal layers discretizes the vertical dimension along the sphere radius [Linardakis et al., 2011]. Section 3.3 gives some more detailed information on the LES package, because it is of particular interest for this thesis and the modeled data. The following two sections state some important information regarding the grid structure of the unstructured triangular grid. Details on the numerical implementation and the dynamical core itself can be seen, e.g., in Zängl et al. [2015] and Dipankar et al. [2015] as this would go beyond the scope of this thesis.

3.1 Horizontal Grid

A major advantage of this model is its grid with triangular grid cells. They are obtained via the Delaunay-Voronoi triangulation, whose structures can be seen in Figure 1. The pink coloured primal Delaunay cell corresponds to the dual graph of the yellow coloured Voronoi cell. The dual edges of the Voronoi cell are orthongonal to and bisect the primal Delaunay cell edges in this case (for more detailed information see Wan et al. [2013]). It allows C-grid type discretization and local refinement in selected areas, in global as well as in regional setting [Giorgetta and Korn, 2015]. Furthermore, icosahedral grids provide a nearly homogeneous coverage of the globe, whereas traditional latitude-longitude grids encounter the so-called pole problem related to the convergence of meridians in latitude-longitude grids, which exhibits severe challenges on a computationally efficient implementation [Deutscher Wetterdienst, 2016b].

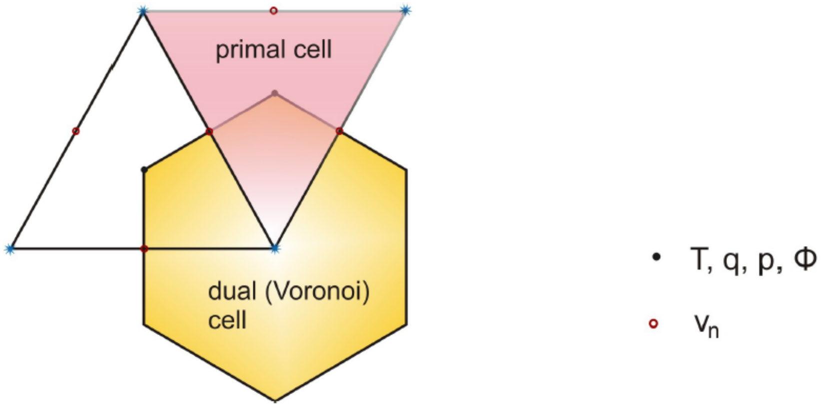

Figure 1. Horizontal grid with primal Delaunay (triangular) and dual Voronoi cell (hexagonal). Note that the dual edges are orthogonal to and bisect the primal edges. With indicated location of T = temperature, q = any scalar, e.g., mixing ratios, p = pressure, Φ = geopotential, v_n = horizontal velocity component normal to the triangle edges. Source Linardakis et al. [2011].

The grid operates in a way that an original icosahedron (cf. Figure 2(a)) is projected onto a sphere, while this spherical icosahedron (cf. Figure 2(b)) consists of 20 equilateral spherical triangles. As a next step the edges of each triangle are bisected into n equal sections. Figure 2(c) shows an example for one triangle where the edges are bisected into equal halves. Using great circle arcs to connect the new edge points yield n^2 spherical triangles within the original triangle. The denotation of the grids in ICON are constructed by an initial root division into n sections (Rn), which is followed by k recursive edge bisection steps (Bk), resulting in a $RnBk$ grid [Linardakis et al., 2011]. Figures 2(d) and (e) show examples for $R2B0$ and $R2B2$ grids. By comparing Figures 2(e) and (f), the advantage of the grid 2(e) is directly visible. It avoids the

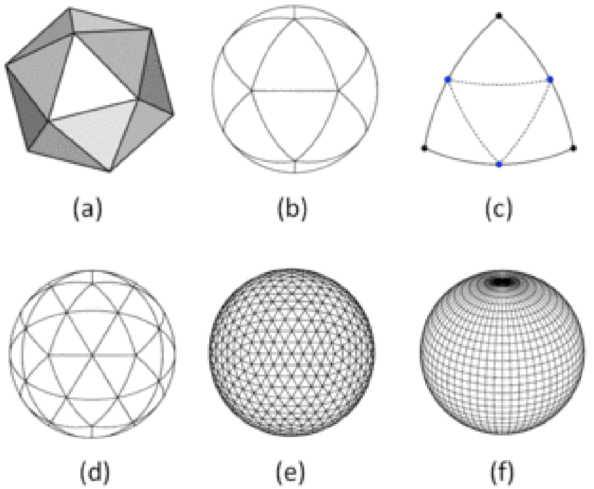

Figure 2. Construction of ICON model grid. The icosahedron (a) is projected onto a sphere, which results in (b). (c) shows that the edges of each triangle are bisected into equal halves. Refining (b) with the method of (c) yields the first spherical icosahedron (d). After two more refining steps, grid (e) is obtained. (f) shows the polar singularities of latitude-longitude grids in direct comparison to the avoidance of that in (e) for the ICON grid. Source [M. Giorgetta, P. Korn and G. Zängl, 2017].

polar singularities of latitude-longitude grids (cf. Figure 2(f)) and it allows a high uniformity in resolution over the whole sphere [Giorgetta et al., 2011]. The grid can be either viewed such as it consists of triangular or hexagonal cells [Wan et al., 2013]. Another advantage of this kind of grid is that it avoids high Courant numbers at the poles, like they occur in latitude-longitude grids. Furthermore, it is highly suitable for grid refinement purposes which is of great interest for the $HD(CP)^2$ project and many other users to improve regional climate and weather prediction and to use ICON as a forecasting model [Griewank, 2009].

Different ways of discretization of the horizontal grid can be seen in Figure 3. Grid properties can be optimized following Heikes and Randall [1995a] (with its basics in Heikes and Randall [1995b]) or Tomita et al. [2002], but was not applied in this figure. In contrary to, e.g., ECHAM or GME (Generic Modeling Environment), the ICON grid can also have regional refinement whereas the former can only cover the whole globe [M. Giorgetta – MPI-M Website, 2016]. An example of this regional refined ICON grid is shown in Figure 4. It is a twofold refined regional grid with the light blue grid indicating the icosahedron defined base grid with 20 triangular faces, 30 edges and 12 vertices. The dark blue grid is the first refinement in which the edge centers form new vertices. The green grid depicts an additional grid refinement only carried out for the northern hemisphere. The red grid shows another refinement step over Europe, based on the green grid.

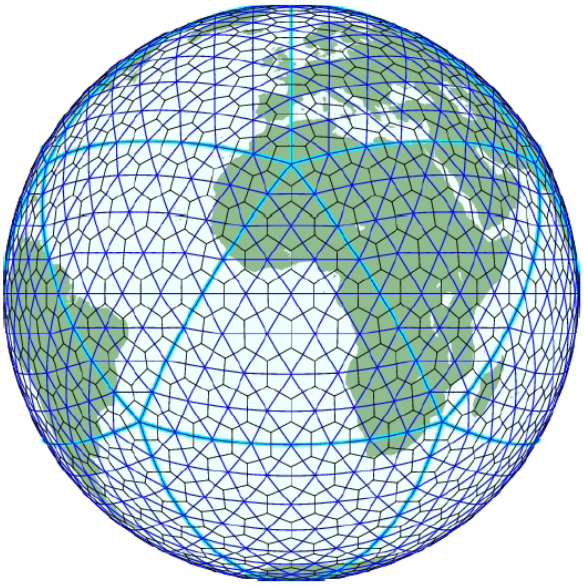

Figure 3. Icon horizontal grid with light blue lines representing the projection of the original icosahedron edges (cf. also Figure 2(d), dark blue lines show the triangle grid (Delaunay) after three edge bisections (R2B02), black lines depict the dual hexagonal grid (Voronoi). Source Linardakis et al. [2011].

Another specialty of the unstructured grid is that the term 'resolution' refers to the square root of the mean cell area in the icosahedral grid of ICON, which is equivalent to about 1.5 times the resolution on a corresponding rectangular grid [Heinze et al., 2017]. For a given resolution $RnBk$, the total number of cells (n_c) is [Zängl et al., 2015]:

$$n_c = 20n^2 4^k. \tag{38}$$

Number of edges (n_e) and number of vertices (n_v) can also be computed:

$$n_e = 30n^2 4^k, \quad n_v = 10n^2 4^k + 2. \tag{39}$$

The effective grid resolution $\overline{\Delta x}$ is defined as:

$$\overline{\Delta x} = \sqrt{\overline{a_c}} = \sqrt{\frac{\pi}{5}}\frac{r_e}{n2^k}, \tag{40}$$

where $\overline{a_c}$ denotes the average cell area and r_e is the Earth's radius. Wan et al. [2013] use a different definition, because the average cell center distances are smaller by a factor of about $\sqrt{4/3}$ on a triangular grid due to having only three nearest neighbours for every cell point. As an example, the $R2B06$ grid has 327680 cells, 491520 edges and an effective grid resolution of $39.5km$. For further examples see Zängl et al. [2015].

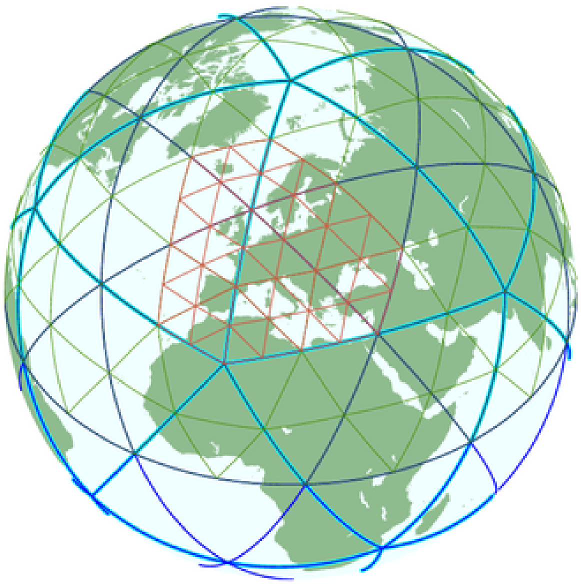

Figure 4. Different horizontal grid refinements of the ICON model. Light blue lines shows the icosahedron base grid with 20 triangular faces, 30 edges and 12 vertices. Dark blue lines indicate the first refinement step based on the light blue lines. The green grid depicts a further refinement step only for the northern hemisphere. Red lines further refines the green grid over Europe. Source Linardakis et al. [2011].

3.2 Vertical Grid

After having already described the horizontal grid in detail above (cf. Section 3.1), the vertical grid needs to be clarified. It consists of a set of layers where each of the layers carries the horizontal two dimensional grid structure. The vertical coordinates have a height-based terrain-following hybrid structure and the smooth level vertical (SLEVE) coordinate implementation [Leuenberger et al., 2010] is used [Heinze et al., 2017]. In case of the hydrostatical dynamical core, pressure-based vertical coordinates are used and in the non-hydrostatical case the vertical coordinates are height-based [Linardakis et al., 2011]. Vertical grid staggering is implemented in ICON and can be controlled by the use of namelist parameters. By specifying model top height and number of height levels in combination with the stretching factor, the model calculates all vertical levels. The stretching factor influences the thickness of model levels. Values smaller than one increase the layer thickness near the model top [Namelist Overview, 2015]. Additional parameters that define structure and thickness of model levels are, e.g., the minimum layer thickness of the lowermost model level and the parameter called 'flat_height' which sets the height above which the coordinate surfaces are flat [Namelist Overview, 2015].

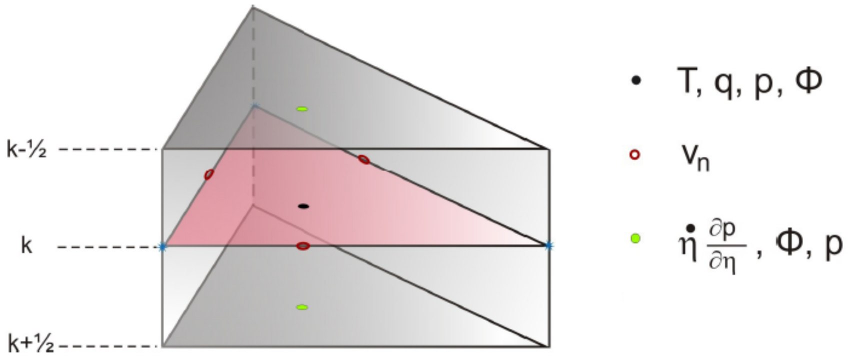

Figure 5. Vertical structure of the primal Delaunay grid. Half levels ($k \pm 1/2$) correspond to η levels. All variables as in Figure 1 and additional $\dot{\eta}\frac{\partial p}{\partial \eta}$ = vertical velocity on η coordinates. Source Linardakis et al. [2011].

Of great importance for this thesis is the location of the quantities on the grid. Most of the variables are mapped on the grid cell centers, edge centers and vertices. Figures 1 and 5 show the location of most of the diagnostic and prognostic variables at the horizontal and vertical grid. Utilized variables for this thesis is, at first, the potential temperature θ $[K]$, which is stored at the center of the triangle (circumcenter) of the primal grid on full level. Vertical velocity w $[m/s]$ and the turbulent diffusion coefficient for heat K $[m^2/s]$ are also important and stored at the circumcenters of the primal grid, but on half levels. They have to be interpolated on full levels for calculations in combination with θ.

3.3 ICON-LEM

ICON in LES configuration was developed for improving the understanding of moist processes as well as their parameterization in climate models by using simulation results [Heinze et al., 2017]. It was not the purpose to be an alternative to standard LES models which are primarily designed for boundary layer studies. The aim was to employ the unified nature of ICON by using its eddy-resolving abilities in order to better understand the processes that are parameterized in the numerical weather forecast or climate configuration. Dipankar et al. [2015] stated that it is difficult to implement higher-accuracy schemes on an unstructured icosahedral grid and therefore some compromises come along with the LES package. Whilst standard LES models, using structured orthogonal grids, allow an easy implementation of higher-accuracy schemes, the conservative discretization of the three-dimensional turbulence scheme on the ICON grid and its coupling to the model dynamics puts some restrictions in order to ensure a reasonable computational cost. It is described as being nontrivial to implement the three dimensional turbulence scheme on a triangular grid on a conservative basis and involves several interpolation operations.

As already stated in Section 3, the two other physics packages (NWP and climate modeling) were designed for subgrid-scale processes of much coarser resolutions than LES uses. Therefore, some parameterizations of them are invalid and must be turned off, because they are already resolved by the LES grid sizes. On the other hand, there are new approaches necessary for representing the subgrid-scale turbulence and more complex microphysical processes had to be introduced [Dipankar et al., 2015]. The parameterizations that had to be turned off:

- convection schemes
- subgrid-scale orographic effects (blocking and gravity wave drag)
- non-orographic gravity wave drag.

And new introduced parameterizations for ICON-LES mode:

- new subgrid-scale turbulence scheme based on classical Smagorinsky [Smagorinsky, 1963] scheme with modifications by Lilly [Lilly, 1962] in order to account for thermal stratification (see also Section 2.3.1 and 2.3.2)
- a double-moment microphysics scheme based on Seifert and Beheng [2001]
- instead of the default diagnostic cloud fraction scheme, a simple "all-or-nothing" scheme is used which assumes a cloud fraction of either 1 or 0 within a grid box
- the default artificial numerical dissipation for LES studies is reduced to fourth order for the momentum equations.

Turbulent fields are filtered as

$$\phi = \tilde{\phi} + \phi' \tag{41}$$

for any quantity ϕ in the model. $\tilde{\phi} = \frac{\overline{\rho\phi}}{\overline{\rho}}$ is the Favre filtering density-weighted filtering operation [Hinze, 1975]. It is used to simplify the filtered compressible Navier-Stokes equations in LES and thereby reducing the number of unknown terms in the momentum and energy equations. The overbar indicates filtering in the traditional manner as used in incompressible flows. The velocity vector $(v_n,\, v_t,\, w)$ forms a right-handed system. Following system results for the ICON-LES model:

$$\frac{\partial \tilde{v}_n}{\partial t} + \frac{\partial(\tilde{\boldsymbol{v}}_{\boldsymbol{h}} \cdot \tilde{\boldsymbol{v}}_{\boldsymbol{h}}/2)}{\partial n} - (\zeta + f)\tilde{v}_t + \tilde{w}\frac{\partial \tilde{v}_n}{\partial z} = -c_{pd}\tilde{\theta}_\rho \frac{\partial \overline{\pi}}{\partial n} + Q_{v_n}, \tag{42}$$

$$\frac{\partial \tilde{w}}{\partial t} + \tilde{\boldsymbol{v}}_{\boldsymbol{h}} \cdot \boldsymbol{\nabla}_{\boldsymbol{h}} \tilde{w} + \tilde{w}\frac{\partial \tilde{w}}{\partial z} = -c_{pd}\tilde{\theta}_\rho \frac{\partial \overline{\pi}}{\partial z} - g + Q_w, \tag{43}$$

$$\frac{\partial \overline{\rho}}{\partial t} + \nabla \cdot (\tilde{\boldsymbol{v}}\overline{\rho}) = 0. \tag{44}$$

The turbulent parametrization terms Q_{v_k} are calculated as the divergence of the subgrid-scale stress tensor τ_{kl}:

$$Q_{v_k} = \left(\frac{\partial \tilde{v}_k}{\partial t}\right)_{turb} = \frac{1}{\overline{\rho}}\frac{\partial \tau_{kl}}{\partial x_l}, \tag{45}$$

where x_l represents the respective orthogonal axes (x_1, x_2, x_3) which were used as $n = x_1$ and $z = x_3$ before, the same holds for the velocity components (v_1, v_2, v_3) which were used as $v_n = v_1$, $v_t = v_2$ and $w = v_3$ in the text above and are represented in equation (45) as v_k. The subgrid-scale stress tensor is parameterized as following [Lilly, 1962]:

$$\tau_{kl} = K_m\left(\tilde{S}_{kl} - \frac{1}{3}\tilde{S}_{mm}\delta_{kl}\right), \tag{46}$$

with K_m as the subgrid viscosity:

$$K_m = 2\lambda^2\tilde{\rho}|S|\left(1 - \frac{Ri}{Pr_t}\right)^{1/2} \quad \text{for} \quad 1 - \frac{Ri}{Pr_t} > 0. \tag{47}$$

λ is proportional to the grid volume $\Delta = (\Delta_1\Delta_2\Delta_3)^{1/3}$ and the Smagorinsky constant c_s. It is varied in the vertical in following manner:

$$\frac{1}{\lambda^2} = \frac{1}{(c_s\Delta)^2} + \frac{1}{(\kappa x_3)^2}. \tag{48}$$

κ is the von Kármán constant, Pr_t the turbulent Prandtl number and $|S| = (\tilde{S}_{mn}\tilde{S}_{mn})^{1/2}$ with $\tilde{S}_{kl}$ as the Favre-filtered rate of strain tensor:

$$\tilde{S}_{kl} = \frac{1}{2}\left(\frac{\partial \tilde{v}_k}{\partial x_l} + \frac{\partial \tilde{v}_l}{\partial x_k}\right). \tag{49}$$

The Richardson number (Ri) is calculated as:

$$Ri = \begin{cases} \frac{N_m^2}{|S|^2} & \text{for saturated air} \\ \\ \frac{N^2}{|S|^2} & \text{for unsaturated air,} \end{cases} \tag{50}$$

with N and N_m denoting the dry and moist Brunt Väisäla frequency [Dipankar et al., 2015]:

$$N^2 = \frac{g}{\theta}\frac{\partial\theta}{\partial x_3}, \tag{51}$$

$$N_m^2 = \left[N^2 + \frac{g}{T}(\Gamma_m - \Gamma_d)\right]\left(1 + \frac{L_v q_{sat}}{R_d T}\right). \tag{52}$$

Γ_m and Γ_d denote the moist and the dry adiabatic lapsrate, respectively, L_v is latent heat of vaporization.

There are slow-physics and fast-physics forcing for the budget equations of the tracers. An example for slow-physics is radiation, fast-physics are, i.e., saturation adjustment, cloud microphysics and turbulence. Slow-physics tendencies are stored to be integrated with the governing equation, because they are called less frequently compared to the fast-physics. Fast-physics are called every physics time step in order to sequentially update the prognostic variables and so they do not need to provide tendencies to the governing equations. Note that Q_{v_n} and Q_w in equations (42) and (43) are categorized as fast-physics. More details on sequential coupling between the turbulence parameterization and the dynamics can be seen in Dipankar et al. [2015] or Zängl et al. [2015] and more general details on the LES configuration of ICON additionally in Heinze et al. [2017].

4 Data

This chapter deals with the characteristics of the model data used for this thesis. Two different simulations are used. The first choice was the so called “Status Simulation” which was conducted within the framework of $HD(CP)^2$. It was the first ’big’ data set being available for all project members and delivering decent results. After some analysis (see Chapter 6 for results) and a deeper look into the data it was decided to operate a new simulation with different output and an additional resolution, adapted to the needs of this thesis. More details on that can be found in Section 4.2 and the drivers for the decision are pointed out in Chapter 6.

In Section 4.1, some general information about the configuration of the simulation for the $HD(CP)^2$ project are stated and Section 4.2 gives details about the new simulation. They include an evaluation of the model simulations with regard to the purposes of this thesis and some problems encountered with the own simulation. Section 4.3 gives a short description of the predominant weather situation at the simulation days, which are helpful for the interpretation of the results.

4.1 Prior Simulation

Basis for diagnosing data output from ICON is a simulation made within the framework of the $HD(CP)^2$ project which is called “Status Simulation”. A three day nested simulation was conducted for a region over almost whole Germany. The simulation period starts at 24.04.2013 00:00 UTC until 26.04.2013 23:59 UTC. Three days with different kinds of weather situations (see Section 4.3 for predominant characteristics at these days). There are three domains of different grid resolutions and their locations can be seen in Figure 6. For the parent domain (DOM01, black circle) a grid resolution of 1.25 km was chosen, such that for the first refinement or so-called nested domain (DOM02, blue circle) a grid size of 625 m results and the smallest domain (DOM03,

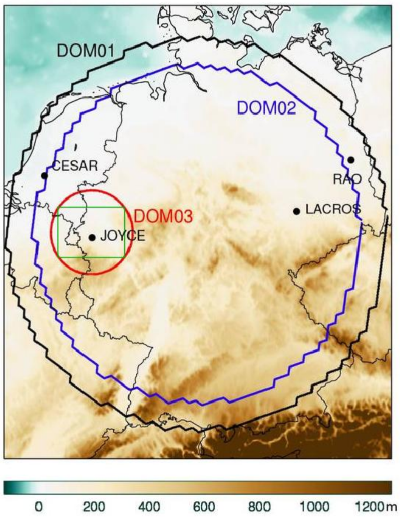

Figure 6. Nested domains for ICON-LEM "Status Simulation" conducted within the $HD(CP)^2$ project. DOM01 (1250 m resolution), DOM02 (625 m resolution) and DOM03 (312 m resolution). Black dots show supersites of the measurement campaigns of the project. Green box shows common domain cutout used for this thesis. Contours show the height above sea level [m]. Source Universität Hamburg [2017].

red circle) reveals a resolution of 312 m. The maximum horizontal extend is about 800 km x 785 km for the biggest domain, 690 km x 670 km for the middle domain and 170 km x 160 km for the smallest domain. Non-hydrostatic dynamics with NWP forcing of the dynamics and transport by parameterized processes without convection as well as the three dimensional Smagorinsky turbulence closure (Section 2.3.1) were chosen. Lateral boundary and initial conditions were data from the COnsortium for small-scale MOdelling (COSMO) numerical weather prediction model which has a resolution of 2.8 km in the COSMO-DE configuration with a domain area over the region of Germany, Switzerland, Austria and parts of some neighbouring countries [Deutscher Wetterdienst, 2016a]. COSMO-DE data was interpolated on all grids by using a radial basis function (RBF) interpolation algorithm (cf. Ruppert [2007] or Peixoto and Barros [2014]) and three dimensional variables are interpolated vertically during initialisation [Heinze et al., 2017]. At the lateral boundaries of the parent domain, the numerical simulation of the model is relaxed towards hourly COSMO-DE analyses in a 20 km wide nudging zone, which is performed on the prognostic variables (cf. Section 3). In case of the "Status Simulation" data, the online nudging zone width of the nested domains is 8 grid points wide, whereby all prognostic variables are nudged at the outer boundary of the nesting domains (cf. Heinze et al. [2017]). Feedback from the refined to the parent domain is turned on for all nested domains, at which each nest gives feedback to the respectively greater domain in which it is embedded. Concerning

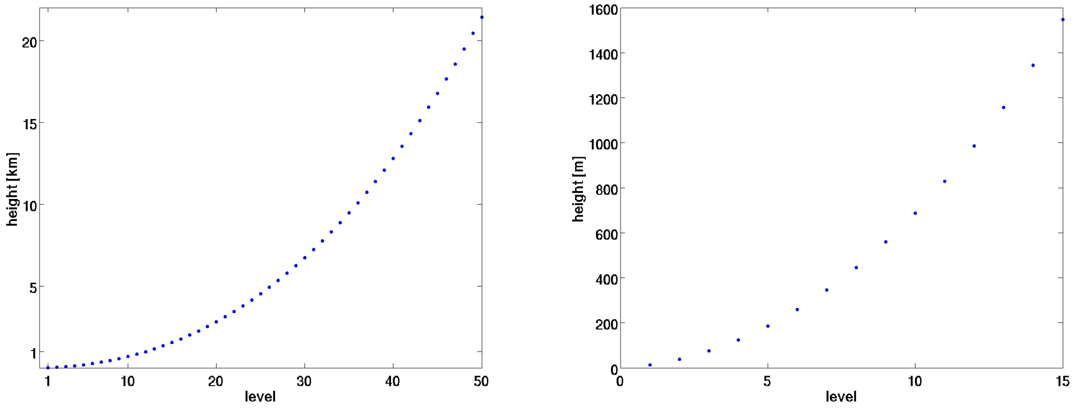

(a) all height levels **(b)** height levels in boundary layer

Figure 7. Height levels for “Status Simulation“ data for (a) all levels [km] and (b) the lower 15 levels [m].

microphysics, the double moment mixed-phase bulk microphysical parameterization scheme by Seifert and Beheng [2001] was used. For radiation, the Rapid Radiation Transfer Model (RRTM) was applied (cf. Mlawer et al. [1995]). For the multi-layer land-surface scheme TERRA (cf. Doms et al. [2011]) the land-surface parameterization without subgrid land-cover variability was chosen [Heinze et al., 2017]. TERRA is also used in COSMO-DE in the same configuration as in ICON, such that no vertical interpolation of the soil variables is necessary. The time invariant data at the lower boundary is taken from observational data sets and gridded on all three ICON grids separately with a pre-processor [Smiatek et al., 2008]. Land use data, topography and soil type specifications are used from dedicated high-resolution observational data sets. A smoothing of the topography is not applied as it was done for Heinze et al. [2017] or the own simulation conducted later (details on that in Section 4.2). The maximum height difference between adjacent grid points can be specified and is chosen to be 3000 m for all domains in this data set.

There are 51 vertical half-levels (50 full levels) going up to a maximum height of 21 km. A stretching factor of 0.9 was utilized and a ’flat_height’ parameter of 16 km (see Section 3.2 for details on the parameters) result in height levels above ground that are shown in Figures 7(a) for all height levels and in Figure 7(b) for the lower 15 levels that are of particular interest for this thesis. Noticeable is that the stretching factor of 0.9 does not have much influence on the grid staggering. Consequently, levels near the surface show a similar spacing as at the model top. Usually, level spacing decreases near the surface since the most important processes occur in the lower 1000 m.

The simulation time step is ten seconds. For the following reasons, different output frequencies are chosen. For slow processes like radiation, e.g., related variables are stored every 3 hours to limit output sizes. Quantities of fast changing processes are stored every half an hour or hourly. The important quantities for this thesis have a temporal resolution of half an hour for vertical velocity, w, and potential temperature, θ, but just hourly for the turbulent diffusion coefficient, K. Hence, subgrid and total heat fluxes have a temporal resolution of one hour since their calculation includes K (cf. Section 5.1).

Evaluation

Desirable for the studies of this thesis would be bigger domains, especially for the one with the highest resolution (cf. DOM03 of Figure 6). For a good comparison, all domains would have the size of the biggest domain with three different resolutions; the finest at a resolution of about 10 m. Such kind of simulation would cost too much computing time and storing capacity. Thus, it was originally decided to analyse the existing simulation, instead of putting too much resources in generating a new one. Furthermore, analysing data simulated within the framework of $HD(CP)^2$ is a quality proof for the project and gives more reliability of the data for this thesis, if the proof is positive. Of course, this will cause some limitations in interpretation and analysis towards an improved subgrid closure.

Another disadvantage of this simulation are circular domains which are a result of the icosahedral grid of the ICON model. A quadratic cutout is used, which reduces the amount of available data. But data near the boundaries have not a good quality and therefore it is necessary to cut some data at the borders of the domain. For reasons of comparison, the cutout is chosen to have an equal domain for all three resolutions. Due to the fact that DOM03 is much smaller than the others, DOM01 and DOM02 lose a huge amount of data. Hence, a cutout of nearly DOM03 is used (see green box in Figure 6) which extend is from $5.3°E$ to $7.5°E$ longitude and from $50.7°N$ to $51.3°N$ latitude. Table 1 shows the horizontal and vertical number of grid points for each resolution after some small changes due to insufficient data at the edges of the potential temperature field. The x-direction is about twice as big as the y-direction. Additionally, data is interpolated from unstructured grid to a latitude-longitude grid, in order to make the analysis and the common rectangular cutout domain more intuitive as using the unstructured data is more difficult to handle. Hence, interpolation uncertainties have to be considered while interpreting results.

Subgrid scale and also resolved quantities like the subgrid potential temperature flux or resolved potential temperature flux, are of big importance for this thesis. They were not stored in the framework of the $HD(CP)^2$ project to keep the output size manageable. Hence, they have to be calculated by using the equations which the model uses internally. This can be done with the help of the turbulent diffusion coefficient for

Table 1. Number of horizontal (x x y) and vertical grid points for equal cutout domain of "Status Simulation" data for all resolutions.

Resolution	**Horizontal grid points**	**Vertical grid points**
1250 m	126 x 48 = 6048	50
625 m	252 x 95 = 23940	50
312 m	496 x 188 = 93248	50

heat and some other prognostic variables (see Section 5), which are available as direct output. But any calculation adds additional uncertainties to the results, because of the difference between output time and internal calculation time. This has to be kept in mind when analysing the data.

4.2 Model Setup

Due to insufficient or not fully comprehensible data available from the “Status Simulation” (henceforth also named StatSim), it was decided to conduct own simulations with the ICON model. The domains of the new simulations are thought to have more area in common in order to have more data that can be analysed. One reason for limiting the area of the parent domain is the additional nesting step with a grid resolution of 156 m. This resolution offers to resolve more processes which leads to a more reliable investigation of the old and the improved subgrid scheme. In addition, the Smagorinsky subgrid closure works better on this scales and was developed for grid sizes around that magnitude. Furthermore, the StatSim data is rather old and was conducted for first analysis purposes within the project. The model and especially the LES package is improved and extended now. The ICON $HD(CP)^2$ branch was used in the version ’hdcp2-20150930’ for the new simulations.

In order to operate the new simulations, many things have to be taken into account and thought of twice. At first, it must be very clear how the simulation is set up. Domain sizes, nudging zone, center of domains, etc. are all very important points and have to be reviewed several times, because they have a huge influence on the running time, memory size (output size) and initialization time. The general idea was to be as close as possible to the StatSim setup in order to have a good basis for a comparison to this data set. Due to the big parent domain of the StatSim and the very small common area of the resolutions (cf. Figure 6), it was clear that the domain sizes could not be the same. Too much area would be wasted with such a huge parent domain. Nevertheless, the domains of the new simulation have an overlap to the often evaluated areas of the $HD(CP)^2$ project, namely they are all centered around the city Jülich. Latitude of Jülich is at 50.91° North and longitude at 6.41° East. Jülich was the supersite of the first measurement campaign of HOPE [$\mathbf{H}D(CP)^2$ **O**bservational **P**rototype **E**xperiment] (for more information c.f., e.g., TROPOS [2013] or Löhnert et al. [2015]) whose observations are mainly used for the evaluation of ICON and essential part of the project in its first phase. Circular domains were chosen, too, because it is known that they work better for the boundary data at the triangular grid. The diameter of the parent domain is 330 km and the online nudging zone of the nests is 18 grid points wide. Furthermore, the nesting was chosen to be similar to the StatSim data with grid sizes of 1.25 km, 625 m and 312 m. The additional nesting step has a resolution of 156 m. Due to the icosahedral grid structure, it is only possible to bisect the resolution at this point. Table 2 shows the resulting number of horizontal and vertical grid points for each resolution after cutting out a common domain. Both horizontal directions are about the same size, which is different to the StatSim data, where the x-direction was about twice as big. There are a few more data points available for the first three domains in comparison to the StatSim data from Table 1. The new fourth domain with 156 m resolution provides the highest amount of data. The common domain extends from 5.6° E to 7.3° E and from 50.4° N to 51.4°

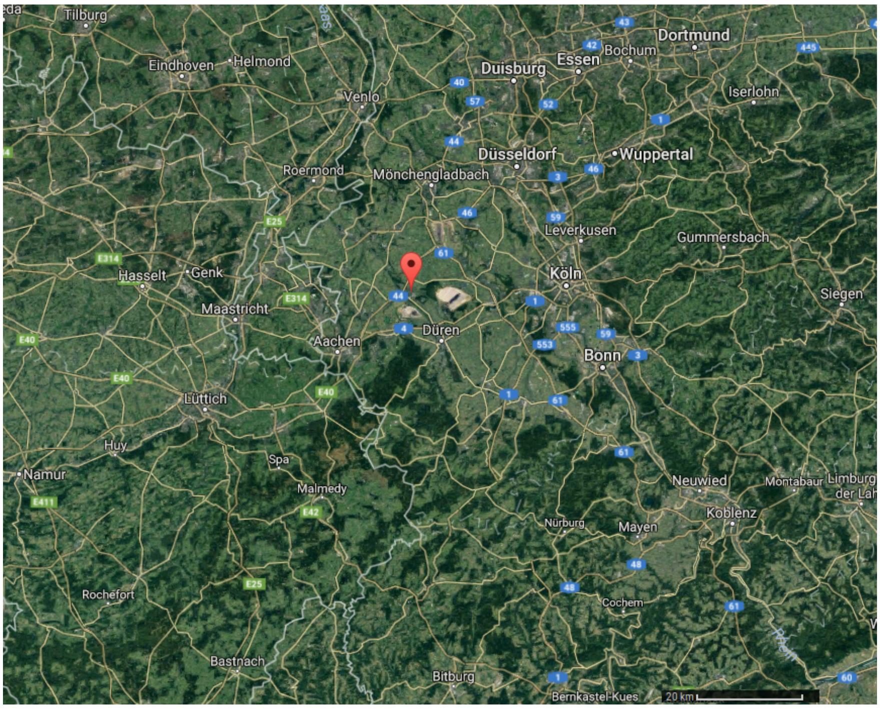

Figure 8. Satellite view of common domain cutout with marked city Jülich. 20 km scale in lower right corner of the figure. Source: maps.google.de.

N, which is about the same size as for the StatSim data set (cf. green box in Figure 6). Figure 8 shows a satellite map of the selected domain. The marking point is the city of Jülich at the center of the new simulation domains. The Rhine is included in the eastern part of the domain as well as the Maas and some water channels and lakes in the western part, running through the Netherlands and parts of Belgium. These water areas can be seen in some patterns of the analysed quantities (cf. Chapter 6). The height over mean sea level, which was used by the model as initial condition for the selected domain of the new simulation, is shown in Figure 9. At about (60,55) km point, a negative height next to a higher situated area is directly noticeable. This area can be also seen in the satellite picture (Figure 8) as two brighter areas around the greenish surrounding. These are opencast mines for brown coal of RWE Power AG (cf. RWE Power AG [2016]) of the locations Inden and Hambach. They have an influence on vertical velocity and resulting grid resolved fluxes. This effect is further explored in Chapter 6.

After having clarified all details, it is about to prepare the simulation. The major tasks are to generate the initialization data for the grids, the external parameters for the grids and the boundary data which is from COSMO-DE, like in the "Status Simulation" setup. The choice and preparation of boundary data, date and time of the simulation is of great importance. The 24th April 2013 was chosen, because it was a

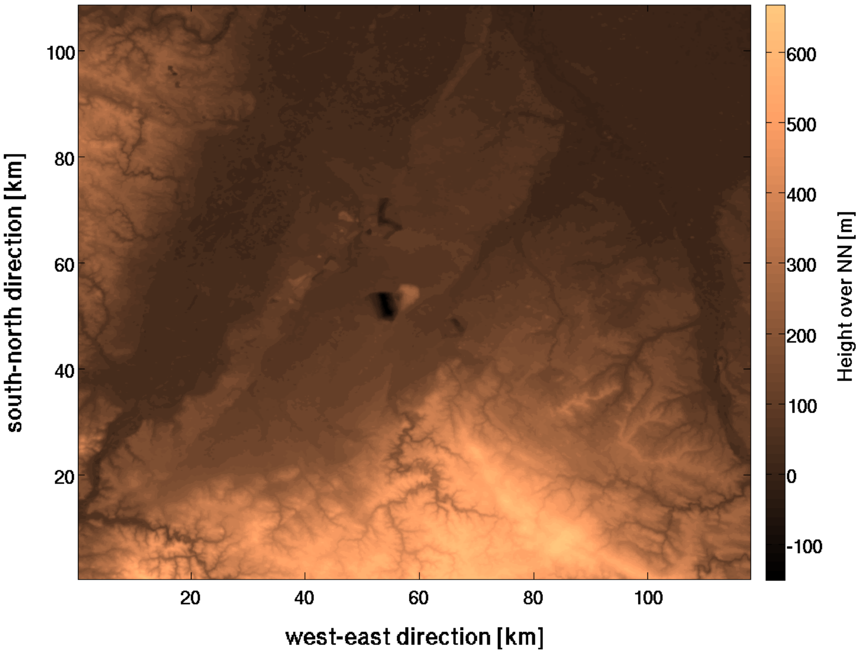

Figure 9. Topography as external parameter of the common domain as height over mean sea level (NN) for the 156 m resolution of the own simulation data.

Table 2. Number of horizontal (x x y) and vertical grid points for each resolution of the new simulations.

Resolution	Horizontal grid points	Vertical grid points
1250 m	95 x 86 = 8170	70
625 m	190 x 172 = 32680	70
312 m	380 x 345 = 131100	70
156 m	749 x 700 = 524300	70

day with no clouds and a normal diurnal circle of temperature. Therefore, it serves as a better source for analysing the consistency of the model as the 25th or 26th of April 2013 with a frontal passage (more on the weather situation in the following Section 4.3)). As already shown in Section 4.1, boundary data are dedicated to high-resolution observational data sets which are gridded on all four ICON grids separately during the model initialization. A maximum height difference of 2000 m, 1000 m, 500 m and 200 m is allowed between adjacent grid points for the new simulation grids, whereas the StatSim data has a fixed height difference of 3000 m.

Also of great importance in terms of memory and output size is the amount of variables that are outputted and at which temporal resolution. The main output quantities needed for this thesis are vertical velocity, potential temperature and the turbulent diffusion coefficient for heat. A big disadvantage is the lack of a direct averaging possibility for output quantities in ICON. Thus, it was decided to run a high frequency simulation with output of one minute and to average it afterwards. In order to keep the output manageable, four hours around noon were selected. As the model needs some spin up time to produce reliable results, the simulation was initialized at 00 UTC at 24th April 2013 without writing output. Writing output started at 10 UTC until 14 UTC, when the simulation time ended. This day was chosen because it proved to be a good day for the purpose of this thesis by looking at the output of the "Status Simulation" (cf. Section 6.1) and by looking at the observations (cf. Section 4.3). Computing time step was ten seconds like in the StatSim data set. All other schemes and settings that are not further specified in this section were the same as for the "Status Simulation".

The first simulation showed a decreasing potential temperature during 10 to 14 UTC at 24th April 2013. Since the observations and the results of the "Status Simulation" show that this is not realistic or is just a very local phenomenon, further investigations had to be done to evaluate possible errors that arose during the simulation or have been made in the model setup. After some testing, it was clear that the restarting process of the model was executed in a wrong way. A test simulation was started to be sure that this is the only reason for the false results. Due to the already stated big amount of output and memory size, the second simulation differs from the first one. In order to check for the whole simulated time period if the results are okay, hourly output from 00 UTC to 15 UTC was written. Hence, only snapshots of one time step of each full hour are available for the second simulation and have to be interpreted carefully. The 'lfeedback' parameter of the namelist was turned off, as it may be too time consuming to have feedback to the parent grid for all nested domains. Another difference is the number of height levels as the coverage of the lower levels was not satisfactorily enough. This applies especially for the 156 m resolution as the vertical extend of the grid box gets much larger than the horizontal extend at some height level. 70 levels instead of 50 levels were chosen with the same top height of 21 km. However, Figure 10 reveals that the coverage is not better at lower height levels when

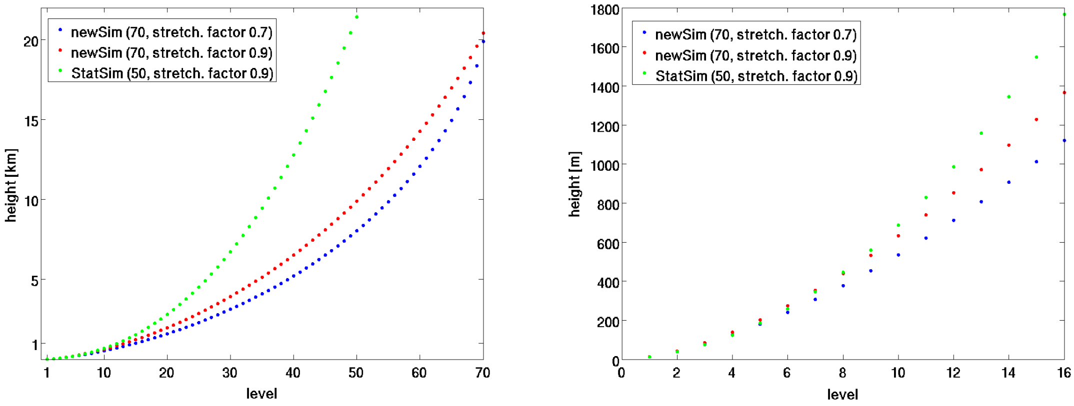

(a) all height levels

(b) height levels in boundary layer

Figure 10. Comparison of height levels for “Status Simulation“ (green) data to the ones of the new simulation with different stretching factors, for (*a*) all levels and (*b*) first 16 levels. Blue indicates new simulation height levels (70) with stretching factor of 0.7, red shows new simulation height level (70) with stretching factor of 0.9 and green shows the StatSim height levels (50) with a stretching factor of 0.9.

using the same stretching factor. Hence, it was assumed that the stretching factor had to be adapted additionally in order to get smaller spacings between the height levels of the lower atmosphere. A stretching factor of 0.7 (blue points in Figure 10) instead of 0.9 (red points in Figure 10) did also not reveal much better results of height level thickness within the boundary layer.

4.3 Weather Situation

This section serves as a short overview of the most important characteristics at the simulation days and for the selected domains. The majority of information was constructed with the help of the archive of Berliner Wetterkarte e.V. [2016] and in addition some maps from webpages, e.g., Wetterzentrale [2016] or wetter3.de [2016] were used to check whether the simulation was in overall accordance with the observations and to choose the more appropriate day for analysis. As a remark, this thesis does not intent to examine the quality of the simulations regarding its concurrence with observations as it aims for exploring the consistency of the model itself by comparing model output of different resolutions.

Mild temperatures of about 18-24°C with just a few high level clouds was the predominant situation over Germany at the 24th April 2013. The night before was rather cold with temperatures down to 2°C in northern Germany, because of dissolving clouds due to high pressure influence. Figure 11(a) shows the satellite image over Europe for the 24th April 2013 at 12 UTC. Germany is nearly free of clouds, which did not change until the evening, where just a few clouds moved into the area which is analysed within this thesis. The surface pressure at 02 UTC is depicted in Figure 11(b) and shows that Germany is mainly under influence of the high-pressure system called 'Paula', which changes slightly during the day when low 'Quirin' moves towards Germany.

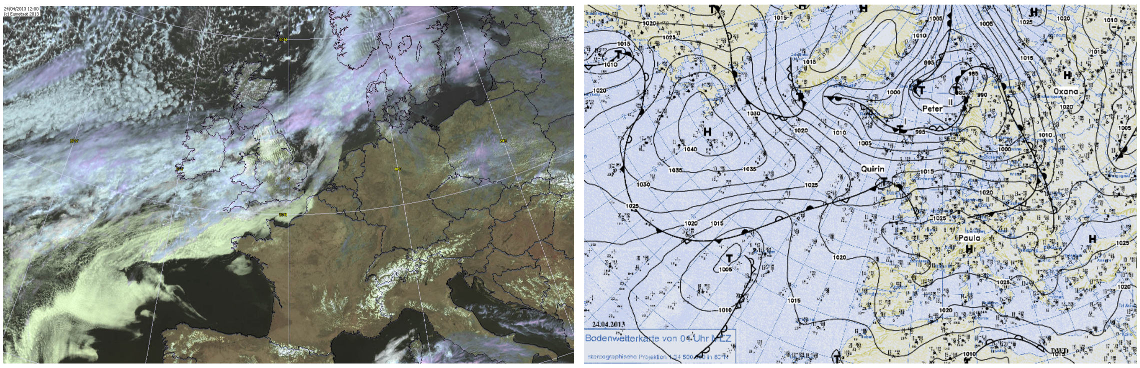

(a) **(b)**

Figure 11. (a) Satellite image of Europe at 24th April 2013, 12 UTC, source: Burton [2006]; (b) surface weather chart of Europe at 02 UTC, source: Berliner Wetterkarte e.V. [2015].

At the 25th, the north of Germany got more and more cloudy with temperatures of around 20°C and up to 25°C in the region of the Rhine. It was clearly colder at the sea with just 12-13°C even at daytime. The clouds stuck in the northern part of Germany, which led to very warm minimum temperatures of 12 to 15°C in that area. During the 26th of April 2013, a cold front crossed Germany. It brought rain over northern Germany in the early hours of that day and moved slowly south-eastwards. Ahead of the cold front, temperatures of over $20°C$ were reached at a bright sky, whereas behind it temperatures of only $10°C$ were measured with a cloudy sky.

Figure 12 combines all the weather information in a meteogram of the days 24th to 27th April 2013 for the station Cologne/Bonn, which lies in the selected area of this thesis. The first row shows observations of temperature $[°C]$ in black, with maximum (red) and minimum (blue) values and the dew point is depicted in green. Most important quantities of the second row are air pressure $[hPa]$ in black and wind gust $[kn]$ in blue. There is also the wind speed, represented by wind flags, in between the first two rows. The third row mainly shows sunshine duration $[min]$ in yellow filled boxes and precipitation $[mm]$ in blue filled boxes, with the black line showing the cloud cover [1/8]. A normal daily cycle of temperature was measured for the first two days. The influence of the cold front at 26th of April can be seen with decreasing temperatures, pressure and starting precipitation at about 10 UTC.

To summarize, the 24th April was nearly free of clouds such that mixing could develop without any external influencing factors like precipitation or clouds. The second day was already more influenced by clouds and decreasing air pressure as the low-pressure system was getting closer. A cold front characterized day, as the 26th was, with different weather situations before and after the passage, resulting in unstable conditions is not appropriate for a general evaluation of the turbulence parameterization. Standard conditions like in case of the 24th of April 2013 are well known in theory and therefore better suitable for analysing a parameterization scheme. Hence, the first day is chosen to be the basis of this thesis. The parameterization has to operate satisfactorily for every weather condition, but the first step is to diagnose whether it is scale independent or not. With this purpose, it is better usable to evaluate the parameterization with the help of a standard condition and being able to compare results to theoretical assumptions and characteristics. Nevertheless, the 26th of April 2013 serves as a comparison data set in order to explore if the scheme is affected by different weather conditions.

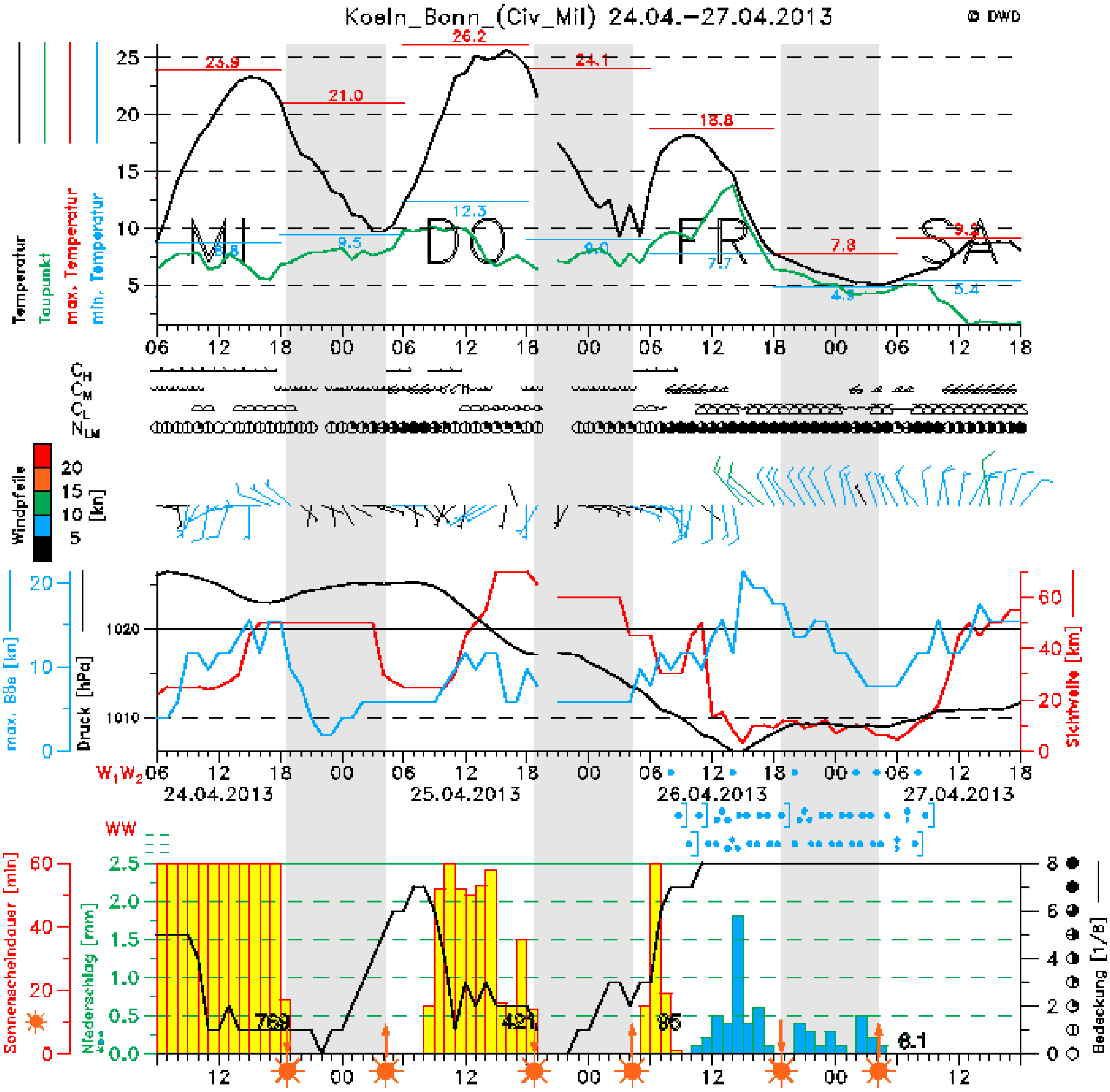

Figure 12. Meteogram of Cologne/Bonn weather station from 24th to 27th April 2013, source: Ermert [2016]. Description in text.

5 Methods

This chapter concentrates on the methods used for analysing data with regard to a quality proof of the simulation data and to investigate the quality of the subgrid parameterization which is implemented in ICON (see Sections 2.3.1 and 2.3.2). First of all, the methods for computing the fluxes are clarified in Sections 5.1, 5.2 and 5.3. Section 5.4 shows a method of computing a flux-matrix with the aim of having more information on which scales contribute the most to the subgrid flux and how the subgrid scales interact between each other.

In order to analyse data with regard to scale consistency of the turbulence parameterization upon the different resolutions, some investigation and calculation is needed. For this purpose, the total vertical heat fluxes are compared, because they represent turbulent behaviour best. Only vertical fluxes will be examined in this thesis as these are of great importance for the planetary boundary layer and the gradients are the largest in that direction. Total heat fluxes in vertical direction will be stated as total heat fluxes only for the sake of simplicity. They can be calculated as the sum of subgrid and grid resolved fluxes. Since the fluxes are not saved during both of the simulations, they have to be computed and some theory is needed. A separate calculation based on each resolution output is useful for an independent comparison of the heat fluxes on every grid scale. Although the fluxes for the coarse resolutions could be computed more accurately using the information of the higher resolution.

5.1 Subgrid Flux

Subgrid fluxes (sgf_x) have to be parameterized using K-theory (see Section 2.2.2):

$$sgf_x = -K_x \frac{d\theta_x}{dz_x}, \tag{53}$$

with $x = 1, 2, 3(,4)$ for each of the resolutions. A positive gradient of $d\theta_x/dz_x$ is coupled with a downward flux as the negative sign of the equation (53) indicates. All variables depend on resolution. Variables K ($'tkhv'$), θ ('θ_mean') and z ('HHL') are direct output variables of the ICON model simulation. The nomenclature of the quantities of the "Status Simulation" are the following:

- $tkvh$ = "turbulent diffusion coefficients for heat" in $[m^2/s]$
- θ_mean = "mean of potential temp" in $[K]$
- HHL = "Geometric Height of the layer limits above sea level(NN)" in $[m]$.

In order to calculate the height differences, height z has to be interpolated on θ-levels by bisecting the height. When fluxes are calculated on level i, the values $d\theta$ and dz are calculated as following, which shows an example for dz:

$$dz = z(:,:,i) - z(:,:,i+1), \tag{54}$$

where the colons stand for both horizontal directions. The lowest model level has the highest level number, e.g., for the StatSim data, level 51 is the lowest model level. The resulting unit of the subgrid flux is $[\frac{K \cdot m}{s}]$. Noteworthy is that '$tkvh$' is not an averaged value, like θ and w. That was realized after the analysis was finished, which exposed the problem of additionally averaging for the new simulation runs.

In case of the new simulations, every variable for calculating the subgrid flux is a direct output. The inverse dz is called 'inv_ddqz_z_half' with a naming description of "metrics functional determinant". Additionally, the '$tkvh$' is "mass weighted turbulent diffusivity" with a unit of $[\frac{kg}{m \cdot s}]$ in this case and a resulting unit of the subgrid fluxes of $[\frac{K \cdot kg}{m^2 \cdot s}]$.

5.2 Grid-scale Flux

Grid-scale fluxes are the ones which are resolved and can be computed as follows:

$$gf_x = (w\_mean_x - \overline{w_x})(\theta\_mean_x - \overline{\theta_x})[\cdot \rho_x], \tag{55}$$

with w_mean_x and θ_mean_x as the mean value of each grid box and $\overline{w_x}$ and $\overline{\theta_x}$ as a spatial mean over the whole considered cutout domain. The density, ρ, is only important for the new simulations. Values $\overline{w_x}$ and $\overline{\theta_x}$ can be calculated with help of:

- w_mean = "mean of vertical velocity" in $[m/s]$
- θ_mean = "mean of potential temp" in $[K]$,

in case of the StatSim data set, which are direct output variables. The new simulations have no averaged values.

Another difference in the calculation for the new simulations is, that equation (55) is additionally multiplied with density, ρ, in the ICON code. This is not severe regarding the calculation of total heat fluxes, because the subgrid flux is also calculated with a mass weighted '*tkvh*' (cf. Section 5.1) such that the resulting fluxes all have a unit of $[\frac{K \cdot kg}{m^2 \cdot s}]$ and thereby not the same as for the StatSim data. Tests by dividing ρ from the grid-scale flux, for example, show that this has not a big influence on the results, especially not on the shape of the curves. Thus, it will be assumed as qualitatively comparable to the StatSim data set.

5.3 Total Heat Flux

Total heat fluxes can be calculated as the sum of subgrid (equation 53) and grid-scale (equation 55) flux:

$$flx_x = \underbrace{-K\frac{d\theta}{dz}}_{\text{subgrid flux}} + \underbrace{(w\_mean_x - \overline{w_x})(\theta\_mean_x - \overline{\theta_x})[\cdot \rho_x]}_{\text{grid-scale flux}}, \tag{56}$$

for $x = 1, 2, 3(,4)$ and, again, a unit of $[\frac{K \cdot m}{s}]$ in case of the "Status Simulation" and $[\frac{K \cdot kg}{m^2 \cdot s}]$ for the new simulation.

5.4 Multiscale Filtering

In order to get a better idea of how the turbulent fluxes behave, it is interesting to look at the behaviour of the fluctuations of the fluxes. Total heat fluxes will be analysed as an example, again. For this purpose, the quantities w and θ are used. To decompose the fluxes into different scales, a multiscale filtering approach is used. It decomposes the original signal into low- and highpass parts. This is done simultaneously for both horizontal directions. Figure 13 shows an example of a decomposition of a data field of either w or θ. Each low-pass is subdivided in one low- and one high-pass again, such that the sum of every high-pass steps and the last low-pass gives the original pattern. Low-passes represent the coarse structure of the pattern, whereas high-passes contain information about small fluctuations.

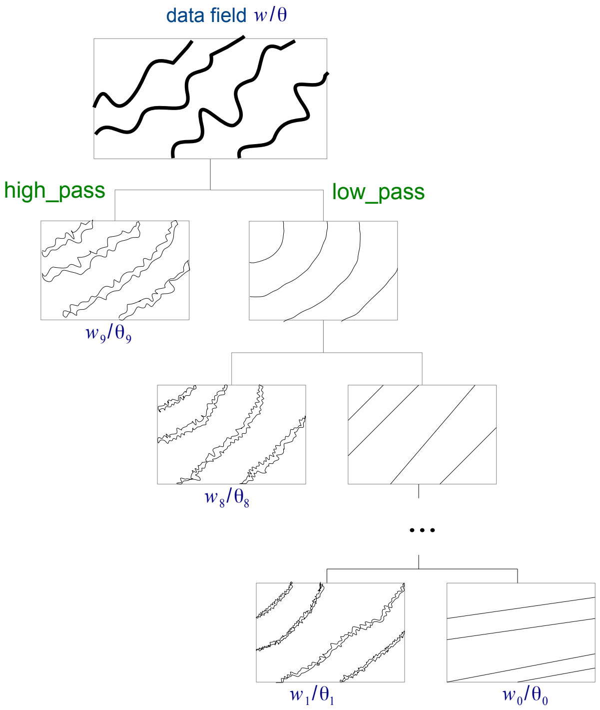

Figure 13. Flowchart for multiscale filtering. A signal of vertical velocity, w, or potential temperature, θ, is decomposed into low-pass (right hand side of the chart) and high-pass (left hand side of the chart). Every low-pass is again decomposed into low- and highpass. The number of filtering steps is limited to the number of grid points. The sum of the last low-pass (w_0 or θ_0) and all high-passes gives the original pattern.

A haar wavelet filter was chosen as it is commonly used for meteorological data. The number of filtering steps is limited to the number of grid points. Each filtering step decreases the resolution of the pattern with a factor of two such that, e.g., starting with a field of 312 m grid size, the resulting first low-pass has a resolution of 625 m.

As the low-pass is always the 'input' field of the next filtering step, the resolution of the high-pass gets also coarser. This will be shown in more detail in Section 6.3.1.

All high-passes and the last low-pass of θ and w are scale dependent and combined to a flux matrix. The theoretical shape of this flux-matrix, **N**, after nine filtering steps (10x10 matrix) is:

$$\mathbf{N} = \begin{pmatrix} w_9 \\ w_8 \\ \vdots \\ w_0 \end{pmatrix} \cdot (\theta_9\ \theta_8\ \cdots\ \theta_0) = \begin{bmatrix} w_9\theta_9 & w_9\theta_8 & \dots & w_9\theta_1 & w_9\theta_0 \\ w_8\theta_9 & w_8\theta_8 & \dots & w_8\theta_1 & w_8\theta_0 \\ \vdots & & \ddots & & \vdots \\ w_0\theta_9 & w_0\theta_8 & \dots & w_0\theta_1 & w_0\theta_0 \end{bmatrix} \quad ,$$

where w_0,θ_0 is the unfiltered signal. Every scale dependent entry $w_{0,1,..,9}$ is multiplied with every $\theta_{0,1,..,9}$ entry. The components of the matrix represent the contributions of the different scales to the flux and the cross-scale contributions, if the decomposition basis is not orthogonal. The upper left corner of the matrix represents the very small scales of both quantities in combination and the lower right corner the larger scales. This matrix has to be interpreted very carefully, because it is not intuitive to understand what the entries of this matrix reveal.

6 Results

This chapter reveals the most interesting results of the analysis for this thesis. To this end, the analysis of 24th April 2013 of the “Status Simulation” serves as the main source for examining how good the model works in terms of reproducing the observations and providing reasonable data in Section 6.1. Data from the new simulations help to validate conclusions of the StatSim data and offers with the fourth and finer resolution some conclusions about the performance of the turbulent closure for resolutions it was originally made for. A comparison to a more convective day is possible through the analysis of the second day of the “Status Simulation”, the 26th April 2013. Section 6.2 deals with results regarding the scale consistency of the subgrid closure upon different resolutions of the ICON model. After that, Section 6.3 is about exploring how the fluxes behave on different scales and to find out which scales contribute the most to the subgrid fluxes. Based on the results, two hypotheses for an improved turbulence closure scheme are stated at the end of this chapter.

6.1 Model Quality

As already described in Section 4.3, the 24th April 2013 date was a day with nearly clear sky and temperatures between 288-294 K at daytime and not much convection in terms of clouds. Whereas the 26th was a day where a cold front passed firstly the north of Germany and moved south-eastwards during the day. The 24th is therefore more suitable for analysis, but the 26th can also serve as a reference and some, but fewer, results are also shown from that day. Noteworthy is the fact that the “Status Simulation“ run was initialized at 00 UTC at 24th April 2013 and the first 6 hours are assumed to be spin up time of the model. Nevertheless, time plots of this run include all time steps since they already look meaningful at least for the state variables. Consequently, analyses of more details are executed for time steps of later hours than 6 UTC. Height information is always, unless stated, in meters above ground, because

ICON uses terrain following vertical coordinates (cf. Section 3.2).

First of all, the time evolution of the mean quantities are important to look at. They reveal information about whether the model works correctly. Figure 14 shows this for all resolutions and for the “Status Simulation“ data at the 24th April 2013 date at the lowest level, which resides at about 10 m in average. Blue indicates the coarsest domain of 1.25 km resolution, red is the 625 m resolution and green represents the finest resolution of 312 m. These colors will represent the just described resolutions throughout the whole thesis. Depicted are domain averages of the common cutout domain. Directly visible is that all the resolutions are in very good agreement and show a daily cycle as expected for a day in April. The lowest potential temperature is 280 K at about 5:40 UTC and the maximum is reached with 292 K at 16 UTC. For a better overview of the potential temperature deviation throughout the lower

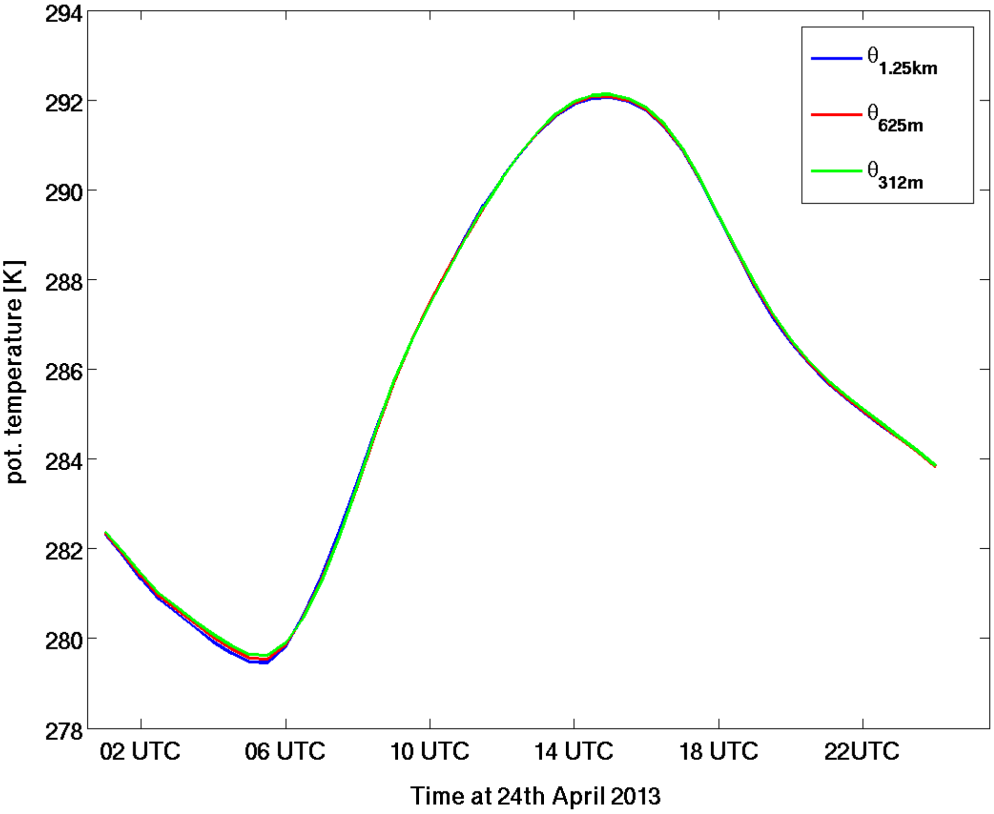

Figure 14. Domain averaged diurnal cycle of potential temperature, θ, of ”Status Simulation” data. Shown are all resolutions at 10 m at 24th of April 2013. Blue lines indicate the 1.25 km resolution, red shows the 625 m resolution and green shows the 312 m resolution.

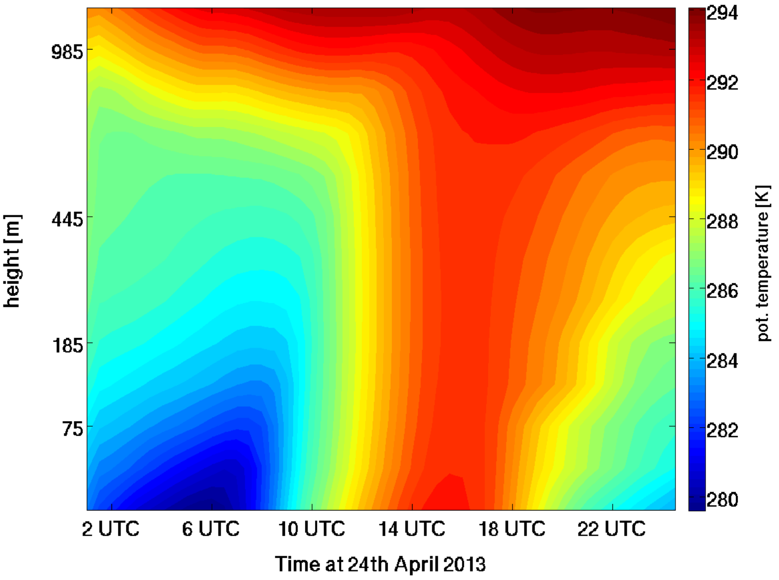

Figure 15. Contours of potential temperature $[K]$ for the "Status Simulation" of 312 m resolution at 24th of April 2013 in dependence of the lower 1000 m of the atmosphere.

atmosphere, Figure 15 shows the time evolution during the 24th of April 2013 for the lower 13 levels and the highest resolution of the "Status Simulation“ data. A normal daily cycle is visible with cold potential temperatures at morning and night hours and a temperature maximum between 13:30 UTC and 18 UTC in the the lowest layer. A maximum temperature of 294 K at the 13th level is reached during 18 to 00 UTC. As expected, potential temperature is greater at higher levels, but between about 10 to 18 UTC gradients are not that big throughout the lower atmosphere.

For the first run of the new simulation setup, the potential temperature does not show a good agreement with observations. Figure 16 shows the temporal development of potential temperature for the 24th April 2013 date of the new simulation. It had a four hour restricted output every minute and was averaged to hourly data in order to make results more reliable. A declining curve from 10 to 14 UTC with 290 K at 10 UTC down to about 284 K at the end of the time period is visible, which is not as expected and as shown by the data of the "Status Simulation“. Comparisons to data simulated by other colleagues using the same ICON branch show the same trend during 10 to 14 UTC and a maximum of potential temperature at about 20 UTC. Observations show that this could not be realistic or is just a very local phenomenon. Further investigations show that the restart process was executed in a wrong way. Although the dynamics of this simulation seems to be realistic and data could be considered as representative of a different simulation day or time period, these results are not further investigated

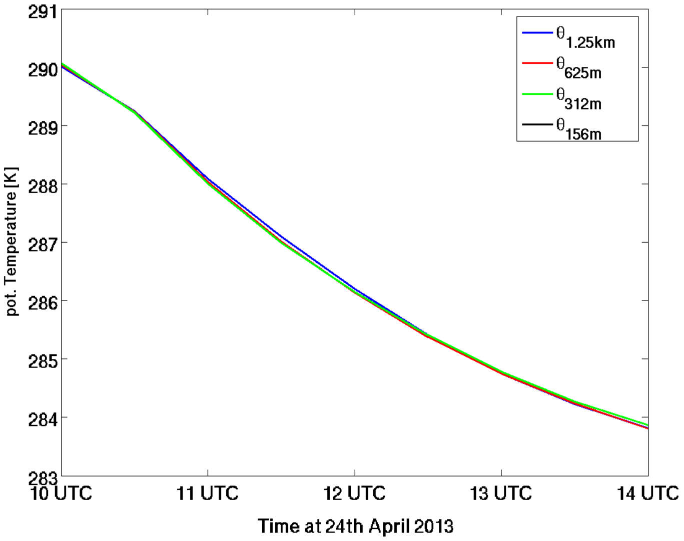

Figure 16. Domain averaged temporal development between 10 to 14 UTC of potential temperature of first own simulation for all resolutions at 10 m. Blue, red and green lines have the same color code as in Figure 14. The black line shows the 156 m resolution.

due to enough data already available. Fortunately, the second simulation produced more reliable output (Figure 17 for virtual potential temperature) and is therefore also further analysed. Noteworthy is that these results contain hourly snapshots of the quantities and the virtual potential temperature instead of potential temperature due to testing purposes.

Having a look at the vertical velocity in Figure 18, the resolutions do not agree well, but minima and maxima occur at about the same time steps. The finest, 325 m, resolution shows always the greatest extremes, both in maxima and minima, and the coarse one has the weakest extreme values, whereas the middle resolution lies in between. Striking is also that from about 8 UTC until 20 UTC all values are positive with a maximum of around 0.009 m/s and negative during the night hours with a minimum of -0.021 m/s. Comparing the timeseries of vertical velocity of the new simulation (Figure 19) with Figure 18, similar shape of the diurnal cycle can be seen. The new simulation shows additionally data until 08 UTC of the 25th April 2013. Positive values reach about the same amplitude of 0.010 m/s, but negative amplitudes are even higher at the new simulation. A minimum of -0.059 m/s is reached at 05 UTC of the 24th April date. The finest resolved grid shows, again, the highest absolute values. Such high vertical wind speeds are not expected, but as already stated in Section 1, ICON is known for overestimating wind speeds.

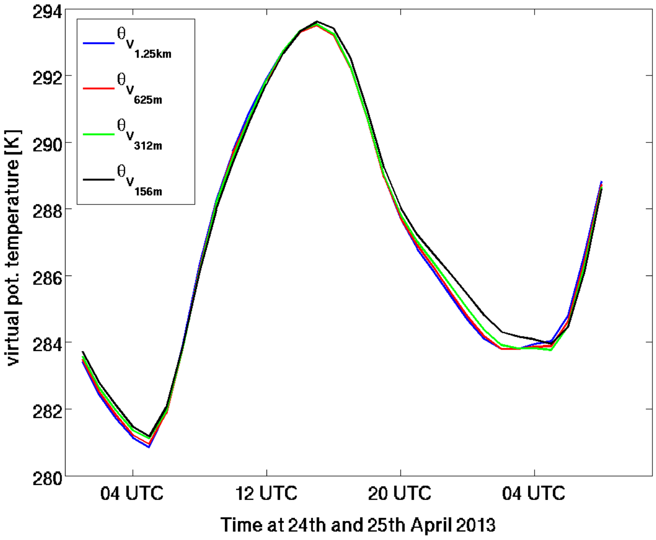

Figure 17. Domain averaged temporal development of virtual potential temperature of correct own simulation run for all resolutions at 10 m level. 00 UTC of 24th April until 08 UTC of 25th April 2013. Colorbar like in Figure 16

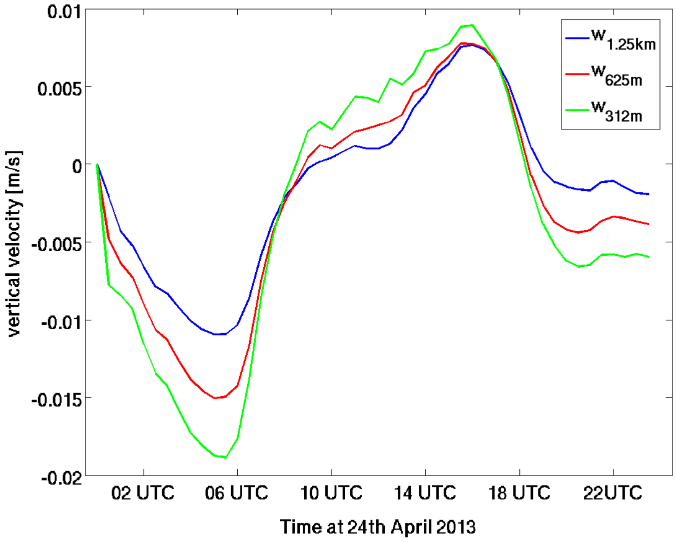

Figure 18. Domain averaged diurnal cycle of vertical velocity, w, for "Status Simulation". Shown are all resolutions at 10 m for 24th of April 2013. Colorbar like in Figure 14.

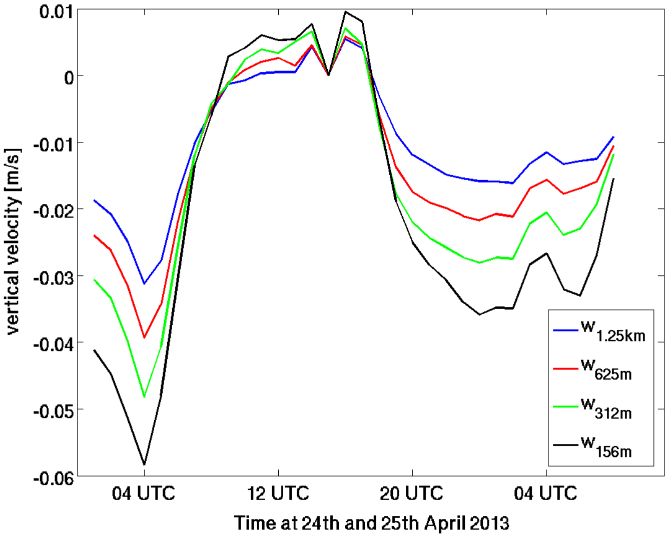

Figure 19. Domain averaged diurnal cycle of vertical velocity, w, for own simulation. Shown are all resolutions at 10 m for 24th of April 2013 to 00 UTC of 25th April 2013. Colorbar like in Figure 16.

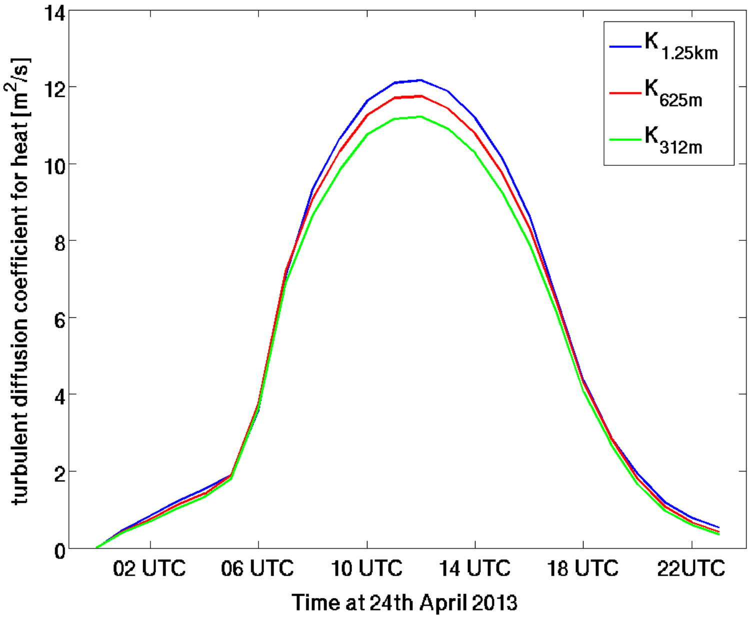

Figure 20. Domain averaged diurnal cycle of turbulent diffusion coefficient for heat, K, of “Status Simulation” date. Shown are all resolutions at 10 m at 24th of April 2013. Colorbar like in Figure 14.

Since the subgrid fluxes are of great importance for this thesis, it is also very interesting to have a look at the turbulent diffusion coefficient (cf. Section 2.3.1), K, which is used for subgrid flux calculation (cf. Section 5.1) and is mostly positive by definition. Some exceptions of negative K values exist, which is already described in more detail in Section 2.2.2. Figure 20 displays the temporal development of K during 24th April 2013 at the lowest model level. A gaussian-shaped curve is visible with a maximum at 12 UTC and a value of 12 m^2/s, whereas it is nearly zero for the night hours. The comparison of the resolutions shows a very good agreement in the night hours and some differences of maximum 1 m^2/s between 9 to 17 UTC. Out of theoretical considerations, K should not be in good agreement upon the resolutions, because different subgrid fluxes are needed to result in the same total heat fluxes. Section 6.2 will clarify more on that. In contrast to the vertical velocity (Figure 18), the plots of K (Figure 20) show the largest maxima at the coarsest resolution.

The temporal development at 24th April 2013 matches the observations stated in Section 4.3 and Figure 21 approves the observations for 26th April 2013 (cf. Figure 12). It shows the temporal development of potential temperature as an example. The cold front passed the selected domain at around 12 UTC with relatively warm morning hours and a maximum of 289 K and a rapid decline of potential temperature down to 279 K at the last time step. Vertical velocity shows a nearly opposed curve progression with negative values until 10 UTC and a good agreement upon the resolutions since that time (cf. Figure 46 in Appendix, Section 8). As a conclusion, it seems that the model produces reliable output of the important quantities and is able to simulate the observed cold front impact.

Looking at contour plots gives an impression of how the quantities and fluxes are distributed over the selected domain. Since the chosen domain center lies in the west of Germany, the domain also includes parts of the Netherlands and Belgium which results in different terrains that could have an impact on the shape of the patterns. Axes are given in kilometers instead of degrees north and east for the sake of assessing sizes of structures more easily and thereby being able to evaluate the reliability of the results directly. Contour plots of potential temperature at 12 UTC for the 24th April 2013 date are displayed in Figure 22 for the lowest model level. Maximum potential temperatures of 292 K appear in the middle and the right bottom of the domain. It is getting colder from south-east to north-west of the domain with a minimum of 287.5 K. Clearly visible is the improvement of resolving individual structures with higher resolutions from 1.25 km to 312 m grid size. There are two vertical lines starting at the top of the patterns of Figure 22. The first one starts at the (60,65) km point and is vertically directed to the south of the pattern. In case of the 312 m resolution, it reaches the bottom of the pattern at the (30,0) km point. The second line starts at the (110,60) km point and is visible until (120,50) km point. This is visible in all patterns, but lesser in the 1.25 km resolution. These lines belong to water in the domain, which was already described in Section 4.2. The right one is the impact of the Rhine and

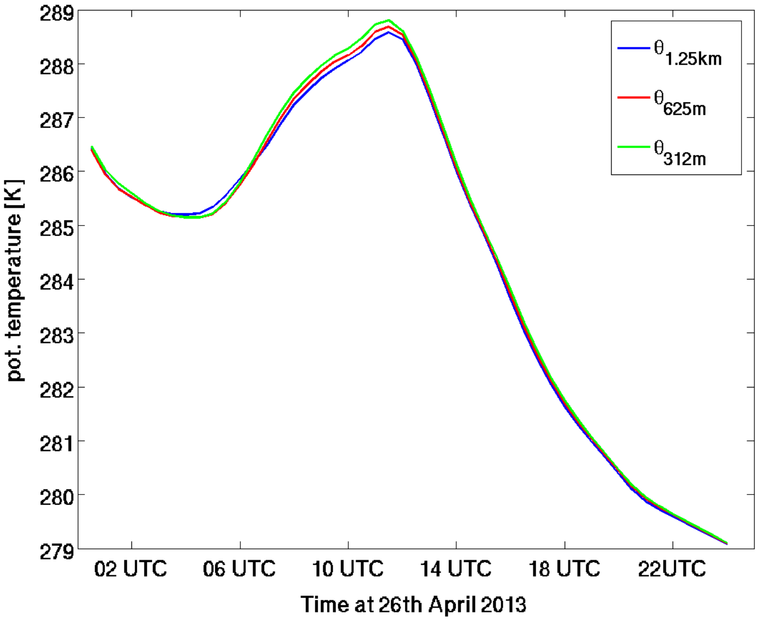

Figure 21. Domain averaged diurnal cycle of potential temperature, θ, for all resolutions at 10 m for 26th of April 2013. “Status Simulation” data with colorbar like in Figure 14.

the left one are some lakes and water channels running through the Netherlands and Belgium.

An improvement of resolving more structures with higher resolutions, is also valid for the new simulations. Figure 23 indicates some differences to the patterns of the StatSim data. It should represent the same day and daytime, but it has a different distribution of θ throughout the pattern. Aside from a slightly different maximum potential temperature of about 293 K, the influence of the lakes and rivers is not visible in this patterns. The structures have also a different shape. Whereas the 1.25 km resolution shows similar longish structures of potential temperature like it can be also seen for the old data set in Figure 22, the other grids for the new simulation reveal rather comb-like structures. Comparison of vertical velocity patterns for both simulations bear no big differences in the distribution of the values throughout the domain at the first model level. The new simulation reaches peak absolute values of about 1 m/s greater than the StatSim data set (not shown here). It was already visible in the time plots in Figures 18 and 19 that vertical velocity is greater for the new simulations in comparison to the StatSim data.

Regarding contour plots of different height levels, some uncertainties attract the attention by looking at vertical velocity. Figure 24 serves as an example for the ”Status

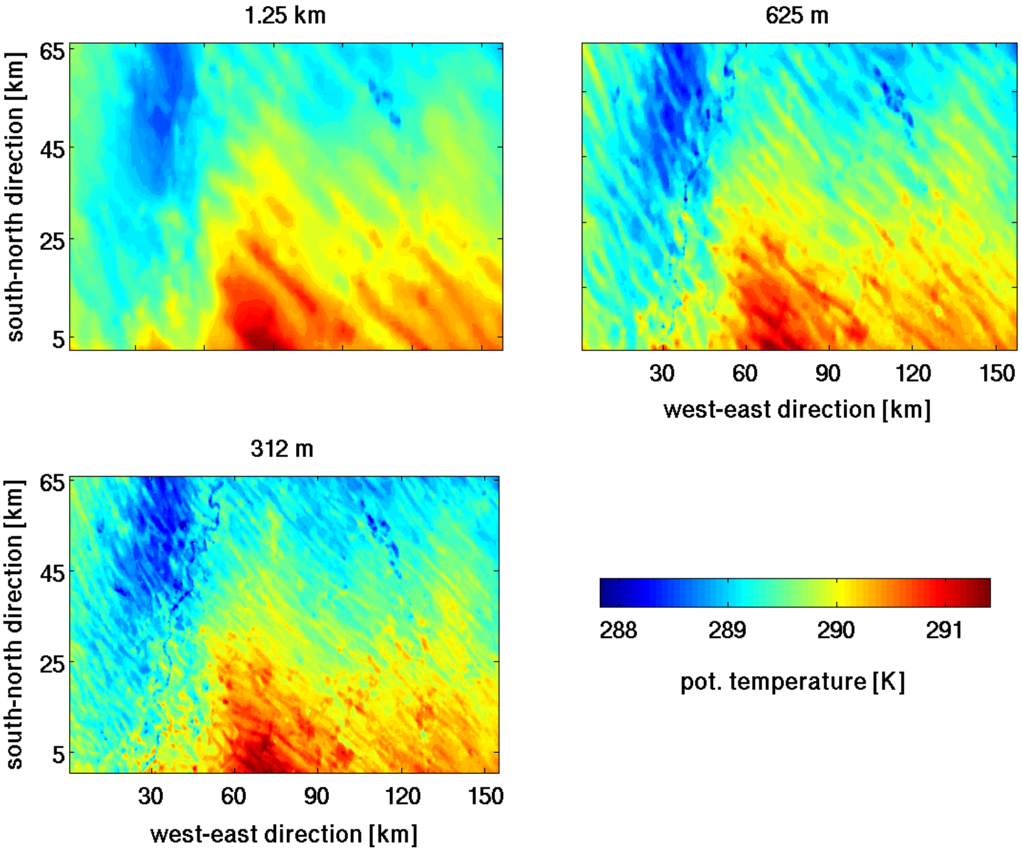

Figure 22. Horizontal patterns of potential temperature contours [K] of the "Status Simulation“. Shown are all resolutions at 24th April 2013 at 10 m and 12 UTC. Axes are given in *km*.

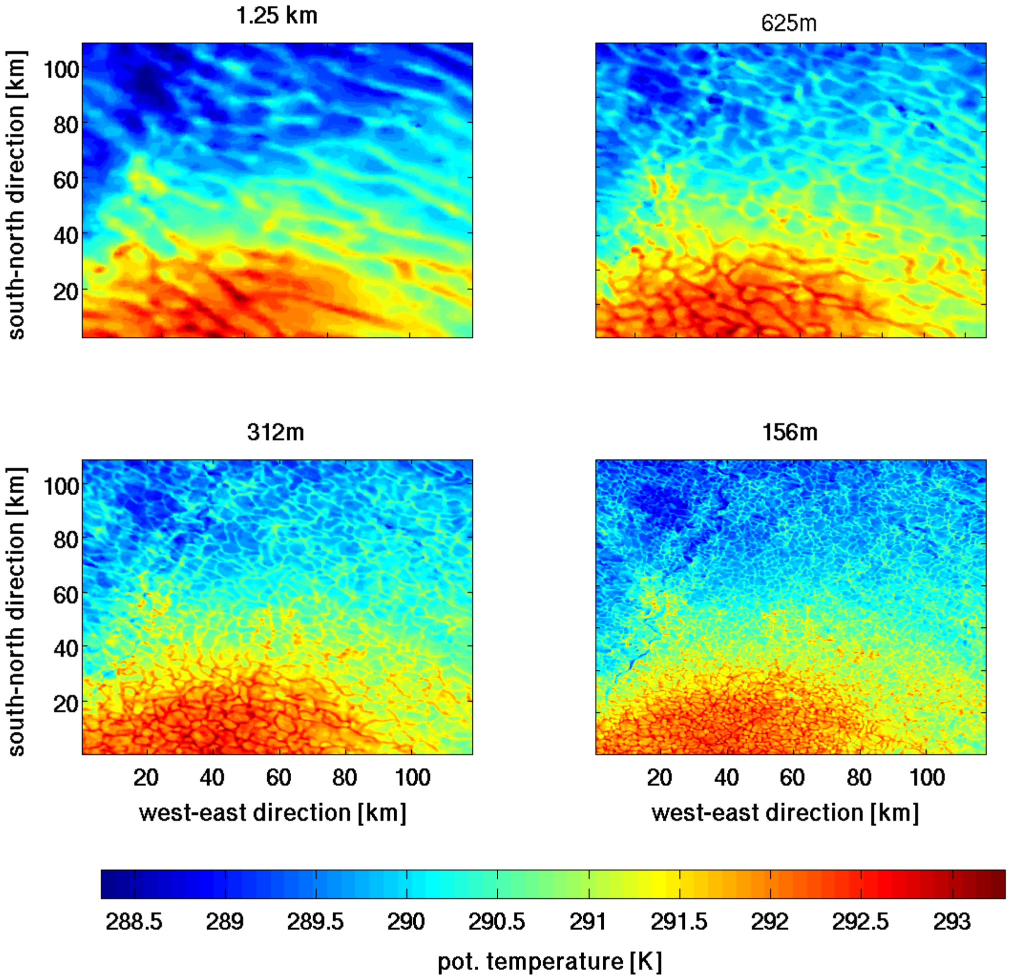

Figure 23. Horizontal patterns of potential temperature contours [K] of the new simulation. Shown are all resolutions at 24th April 2013 at 10 m and 12 UTC.

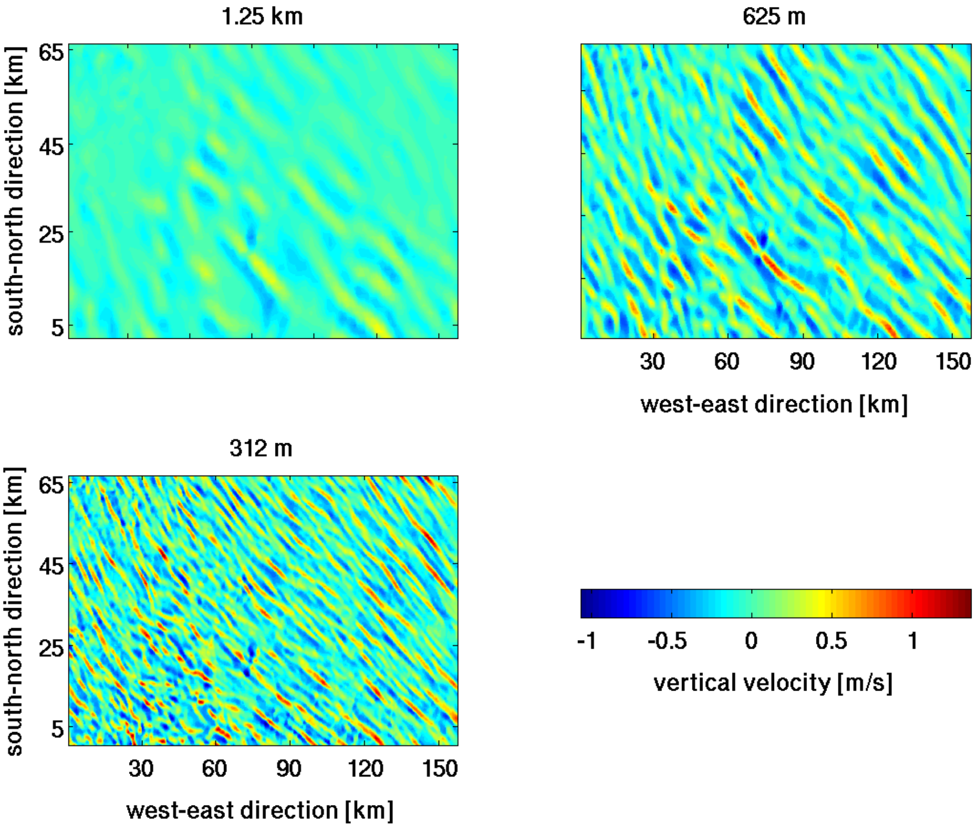

Figure 24. Horizontal patterns of vertical velocity contours [m/s] of the "Status Simulation" data. Shown are all resolutions for 24th April 2013 at 12 UTC and 180 m.

Simulation" data and contains vertical velocity contours for all three resolutions at 12 UTC and about 180m height in average. Wavelike structures dominate the patterns, but they are not noticeable at the lowest model level (see Figure 25). The bulk of values are around zero and structures of non-zero values occur with both, negative and positive values around 1 m/s and therefore diminish in spatial averages. These structures can have an important influence on the results of the calculation of the grid resolved and total heat fluxes (see Section 5 for the calculation of the fluxes). They are also present in contour plots of higher levels of these fluxes. Since these wavelike structures do not seem to result from numerical calculations, it is assumed that there are gravity waves occurring due to a stable atmosphere.

For the sake of completeness, Figures 26 and 27 show contour plots of the turbulent diffusion coefficient for heat, K, of the "Status Simulation" and the new simulation, respectively. Notice the different units due to different output (cf. Section 5.1). Again,

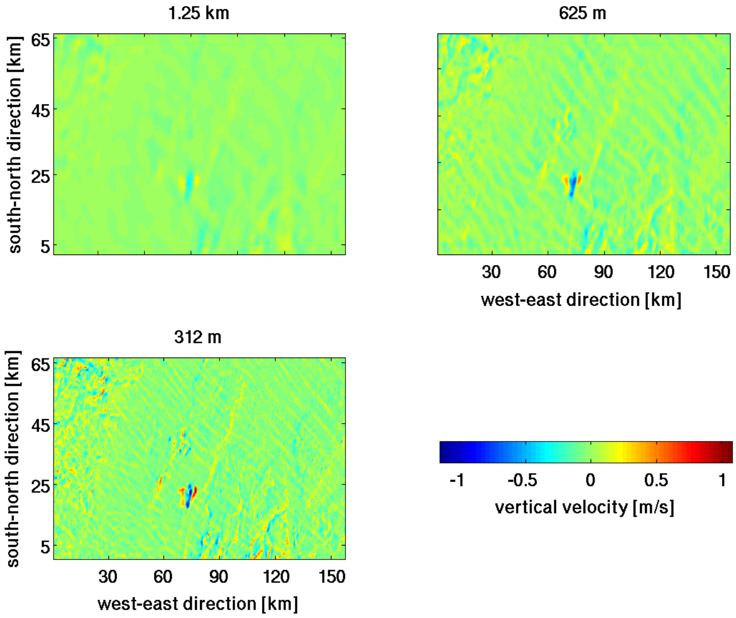

Figure 25. Horizontal patterns of vertical velocity contours [m/s] of the "Status Simulation“ data. Shown are all resolutions for 24th April 2013 at 12 UTC and 10 m.

the figures are for 24th April 2013 and 12 UTC, but at about 445 m height in order to have a comparison to what patterns look like in other height levels. Colorbars are adapted to the widest range of values that occur. In case of K, this is always the coarsest resolution. Figure 47 in the Appendix (Section 8), displays the above stated exception for the lowest model level. K influences subgrid fluxes the most regarding different resolutions (cf. calculation of subgrid flux in Section 5.1) as potential temperature is similar for all resolutions and dz is fixed. Theoretical considerations in terms of subgrid fluxes indicate that these unresolved fluxes have to be greater for coarser resolutions since more area exists within one grid cell compared to higher resolution grid sizes. Taking this into account, patterns of K seem meaningful for both simulations. Comparing the structure of the patterns of the two simulation sources does not reveal big differences. Values are not directly comparable due to different units, as stated before.

Figure 28 shows contour plots of total heat fluxes for the new simulation at all resolutions. The patterns are similar to that of the StatSim (not shown here, but underlying figure of Figure 36 in Section 6.2), but with bigger values. These differences arise due to bigger values for both, grid resolved and subgrid fluxes. This can be explained by the above stated greater values for vertical velocity and differences in the values of the turbulent diffusion coefficient for heat. As already pointed out above (cf. Section 5.2 for further explainations), the fluxes are not directly comparable to each other

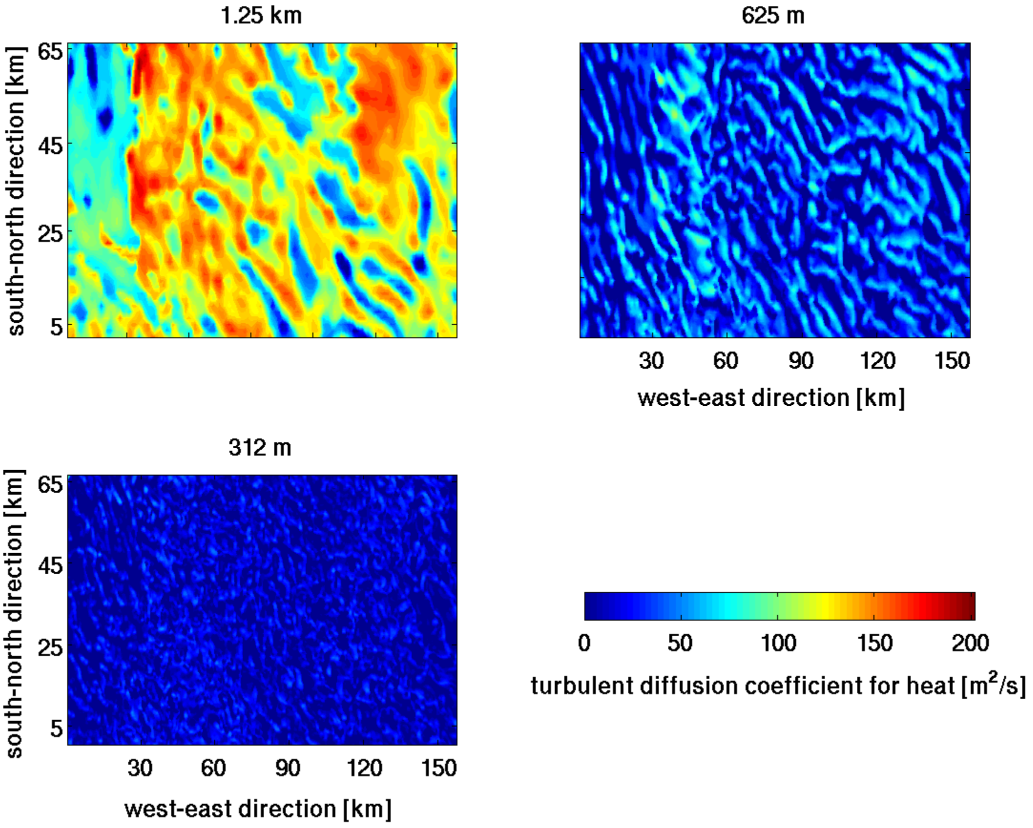

Figure 26. Horizontal patterns of the turbulent diffusion coefficient for heat, K $[m^2/s]$, as contours for all resolutions. Shown are "Status Simulation" data for 24th April 2013 at 12 UTC and 445 m.

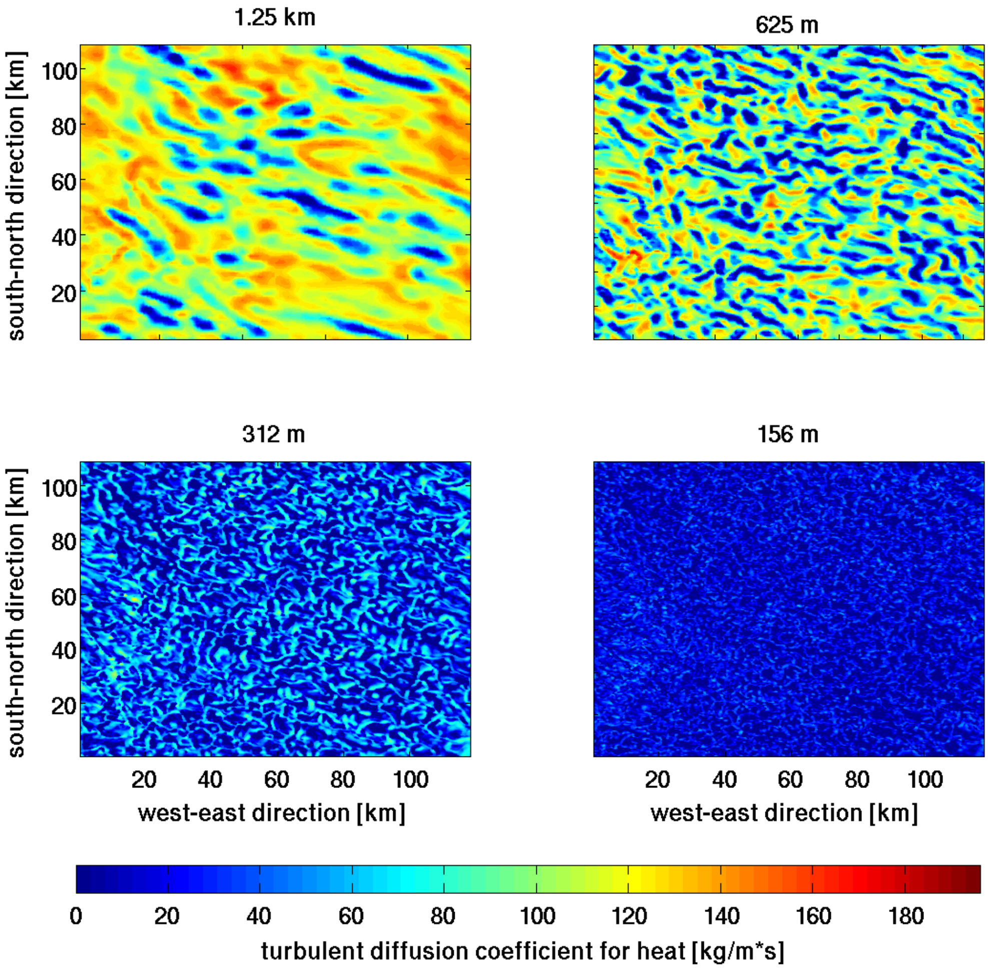

Figure 27. Horizontal patterns of mass weighted turbulent diffusivity, K $[\frac{kg}{m \cdot s}]$, as contours for all resolutions. Shown are data of the new simulation for 24th April 2013 at 12 UTC and 445 m.

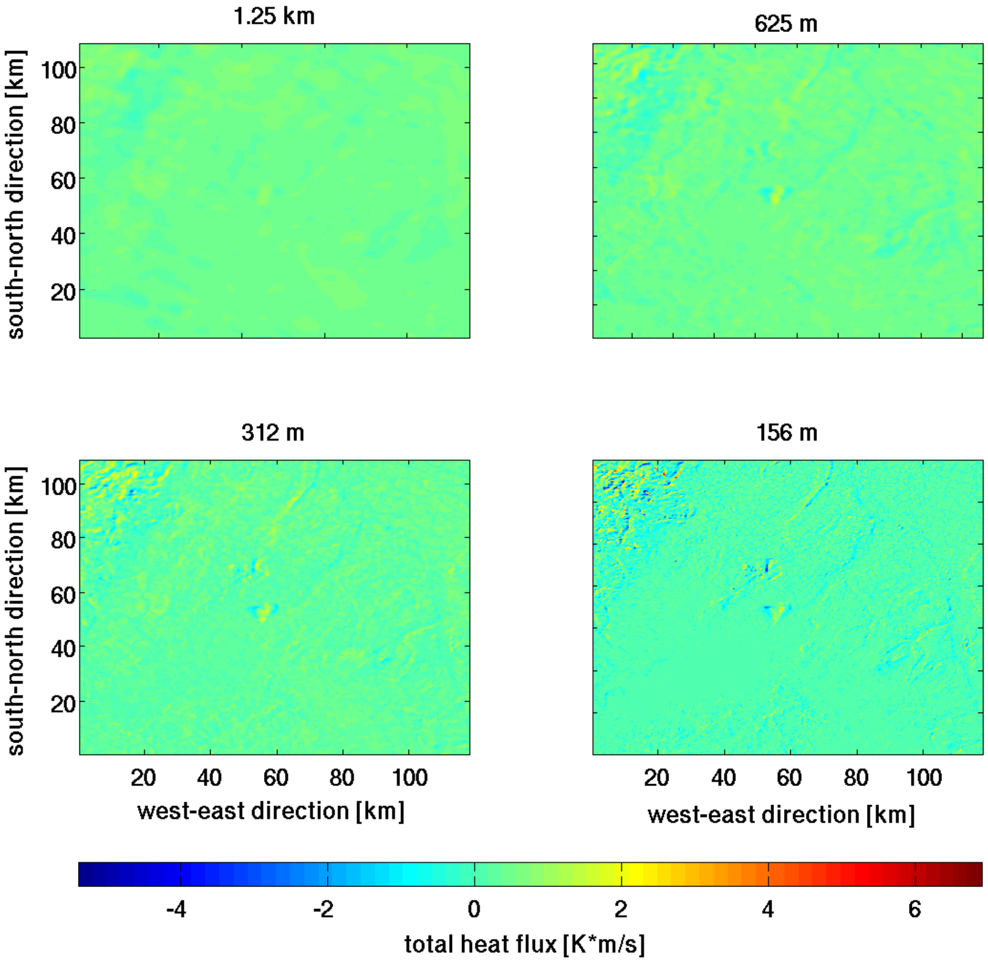

Figure 28. Horizontal patterns of total heat flux $[\frac{K \cdot m}{s}]$ as contours for all resolutions. Shown are data of the new simulation for 24th April 2013 at 12 UTC and 10 m.

due to different units. However, Figure 28 should primarily serve as an example for demonstrating the shape of the horizontal patterns at the lowest model level. It shows an eye-catching point in the middle of the domain where an area of negative and one positive area in western and eastern direction, respectively, are located directly side by side. This was already visible in Figure 25 for vertical velocity of the StatSim data set. This structures can be explained by looking at Figure 8 in Section 4.2. Right at the marking point are two areas of bright soil with more ore less normal nature and some small cities in between. These two areas are opencast mines for brown coal of RWE Power AG (cf. RWE Power AG [2016]) of the locations Inden and Hambach, as already explained in Section 4.2. They are big and outstanding enough to have an impact on the horizontal patterns of vertical velocity. Consequential, they are clearly visible in the horizontal fields of resolved and total heat fluxes for both model simulations.

Based on the results of this section it can be concluded that the ICON model reproduces reliable output for the "Status Simulation“ data in terms of potential temperature in comparison to observations. Time series of θ show a normal daily cycle for the 24th of April 2013 and the frontal passage with falling potential temperatures during the 26th of April 2013. The new simulations are also able to capture a reasonable daily cycle in terms of potential temperature. Time series of vertical velocity show values that seem to be too big for the predominant weather conditions for the 24th April 2013 of both data sets. The new simulations show larger amplitudes than the StatSim data. In contrast, the 26th April 2013 shows a good accordance and reasonable absolute values of vertical velocity for 10 to 23 UTC. Other quantities, like the turbulent diffusion coefficient for heat or total heat fluxes, take on reasonable values by looking at horizontal patterns of both simulations. The patterns reflect the topographic characteristics of the domain, except of some disagreement of K at the lowest model level for the StatSim data set. However, it should be emphasized once again that this thesis has not the purpose of evaluating the ICON model against observations. The main focus lies on the investigation of the consistency of the turbulence closure scheme implemented in ICON regarding different model resolutions.

6.2 Scale Consistency

After having clarified that the model works satisfactorily, it is about to examine whether the output of the ICON model is scale dependent or – and this would be the best case for the model – scale independent and thereby scale consistent. To this end, total heat fluxes were analysed as representative for turbulent behaviour. Total heat flux is calculated as the sum of grid resolved and subgrid flux, whereat both of them have to be calculated with the help of model output quantities. Sections 5.1 to 5.3 demonstrate the equations used for the flux calculations. The closure used for the subgrid scale parameterization is the Smagorinsky closure with Lilly extension (cf. Sections 2.3.1 and 2.3.2) and is primarily valid and developed for only small eddies to be present in the atmosphere. Nevertheless, it is often and commonly used in models even for coarser grid resolutions like it was chosen for the "Status Simulation" with a parent grid of 1.25 km size. Out of comparison and simplicity reasons the closure was also used as parent grid in the new simulation. It should be noticed that most results shown in the following are for 12 UTC, because mixing is known to be fully active at this time. Comparisons of different time steps of one day show that differences of fluxes are present throughout all time steps and especially for higher levels in case of the StatSim data set. Figure 29 is an example of a time series of total heat fluxes at about 180 m of the "Status Simulation". It is conspicuous that the first 6 hours have a relatively good agreement upon the resolutions. This is visible for subgrid fluxes as well and most probable due to the influence of the diffusion coefficient for heat, K. It is likely that this quantity needs some spin up of the model in contrary to potential temperature or vertical velocity (cf. Figures 14 and 18).

Figure 30 shows a height plot of all fluxes calculated for 24th April 2013 from the "Status Simulation" for 12 UTC as a spatial mean over the selected domain. Grey lines indicate the four height levels that were analysed in more detail. They lie at about 10 m, which is the lowest model level, at about 180 m, 445 m and 680 m height above ground. Directly visible is the fact that subgrid and total heat fluxes lie really close to each other. The grid resolved fluxes are very small. Subgrid and total heat fluxes start with positive values near the ground and turn negative from around 450m on, whereas grid fluxes start negative, but remain very small in amplitude throughout all height levels. Total heat fluxes show the highest amplitudes for the coarsest (blue) resolution with up to 100-200 W/m^2 difference in sensible heat fluxes compared to the 312 m resolution. A good agreement upon the resolutions is visible for the lowest two simulation levels. As expected, subgrid fluxes are getting bigger in absolute values with coarser resolutions, but normally grid resolved fluxes should be vice versa in order to receive the same total heat flux at the end. This is not the case for the bulk of height levels when comparing all resolutions. Furthermore, total heat fluxes are mostly driven by the subgrid fluxes as the grid fluxes are small. This is also true for the 26th April 2013 date of the Status Simulation (cf. Figure 48 in Appendix, Section 8), but it is different for the new simulations. Subgrid fluxes are mostly driven by the

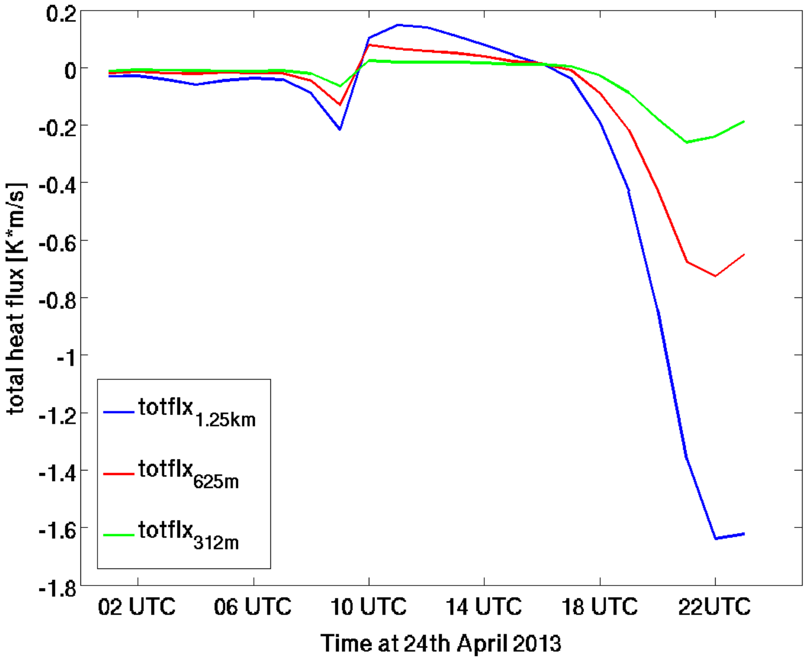

Figure 29. Domain averaged time series of total heat flux for “Status Simulation” data. Shown are all resolutions for the 24th of April 2013 at 180 m. Colorbar like in Figure 16.

turbulent diffusion coefficient for heat, K, and as already pointed out in Section 6.1 this value has a good agreement upon the resolutions at the lower model levels. This is different in other height levels, as is shown in Figure 31. It should be different for the different resolutions, but due to the very small grid-scale fluxes, a good agreement of K results in a good agreement of total heat flux.

Figure 32 displays all fluxes for the four resolutions of the new simulation at 12 UTC more clearly arranged for that amount of curves. Total heat flux is in a better agreement upon resolutions as for the ”Status Simulation” in Figure 30, except for the lowest levels, which were in good agreement for the StatSim data. Furthermore, the highest resolution shows a little perturbation at about 50 m height in Figure 32(c) to smaller values with a steeper slope than all the other resolutions have. From about 200 m height on, it follows almost the same gradient as the others with higher levels. Starting with a total heat flux of about 0.18 $\frac{K \cdot kg}{m^2 \cdot s}$ in case of the 156 m resolution, this differs a lot to the about 0.42 to 0.48 $\frac{K \cdot kg}{m^2 \cdot s}$ of the other resolutions. Looking at the grid flux in Figure 32 (a), the resolutions show the expected arrangement of the biggest absolute values for the highest resolution and the smallest values for the coarsest resolution. This is not exactly true in all heights since the 312 m resolution is bigger than the 156 m resolution at a range of 400 to 800 m height. The grid flux has to be bigger

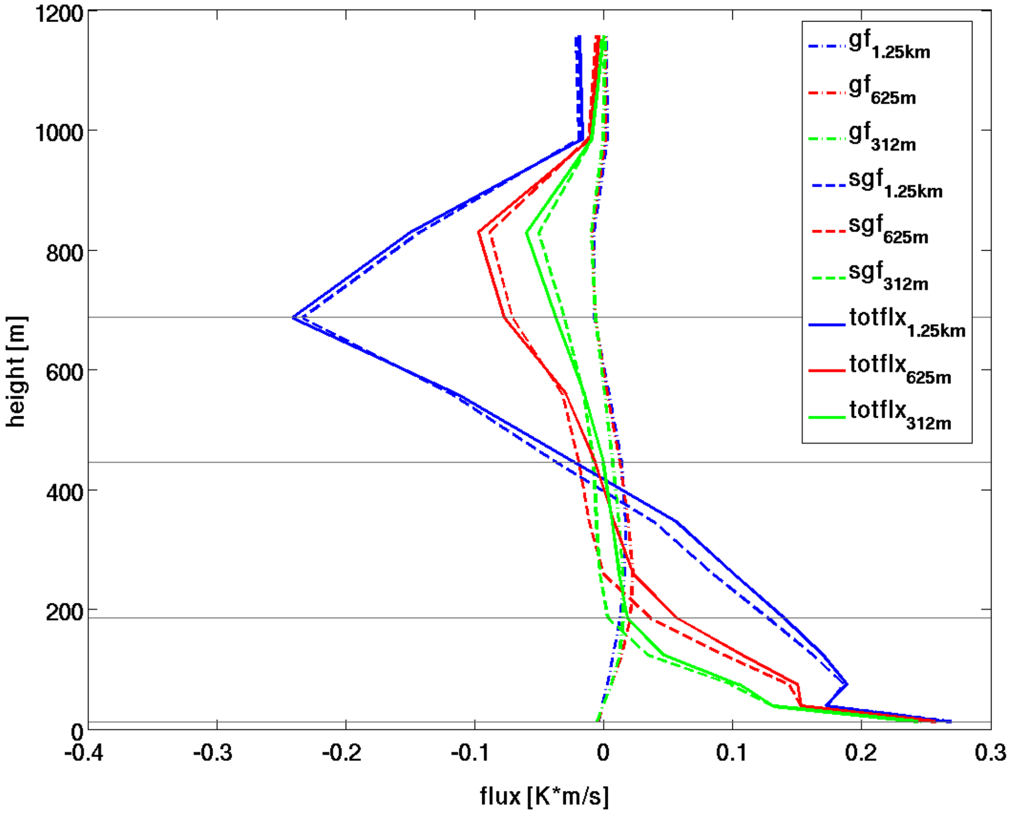

Figure 30. Domain averaged height plot of grid resolved (.-), subgrid (--) and total (-) heat fluxes $[K \cdot m/s]$ of the "Status Simulation" data. Shown are all resolutions at the 24th of April 2013 at 12 UTC. Colorbar like in Figure 16.

for the highest resolution, because more structures are resolved within the smaller grid and bigger grid sizes involve more area that has to be parameterized. This is not true for the StatSim data set and the values are very small in this simulation. Grid resolved values of the new simulation with a maximum of 0.18 $\frac{K \cdot kg}{m^2 \cdot s}$ are much greater than those of the StatSim, which had a maximum of about 0.02 $\frac{K \cdot m}{s}$. It should be again noticed that the values are not directly comparable as the new simulation has mass weighted values, but if multiplying density of about 1.2 $\frac{kg}{m^3}$ to the grid-scale flux, the maximum value for the StatSim data set reaches 0.024 $\frac{K \cdot kg}{m^2 \cdot s}$. Accordingly, the arrangement of the resolutions should be vice versa for the subgrid fluxes and Figure 32(b) proves this for nearly every height level. At a range of about 900 m to 1100 m, the 312 m resolution has some bigger values than the other ones and misses a little peak that all other curves show at about 1000m. Again, the values of the subgrid fluxes are much bigger than those of the grid-scale fluxes as it was already pointed out for the "Status Simulation" data and therefore has the most influence on the total heat fluxes.

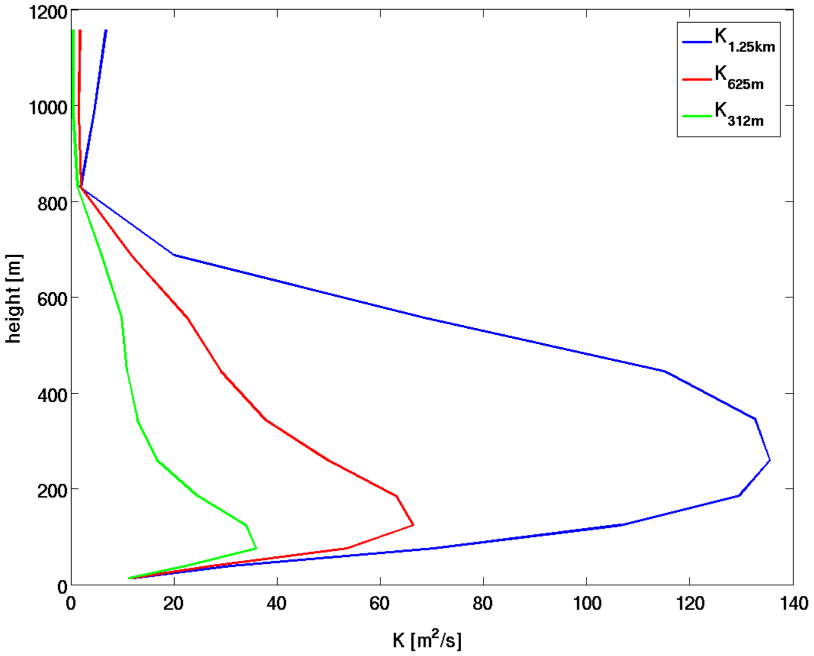

Figure 31. Domain averaged height plot of turbulent diffusion coefficient for heat, K $[m^2/s]$, of the "Status Simulation" data. Shown are all resolutions for the 24th April 2013 at 12 UTC. Colorbar like in Figure 16

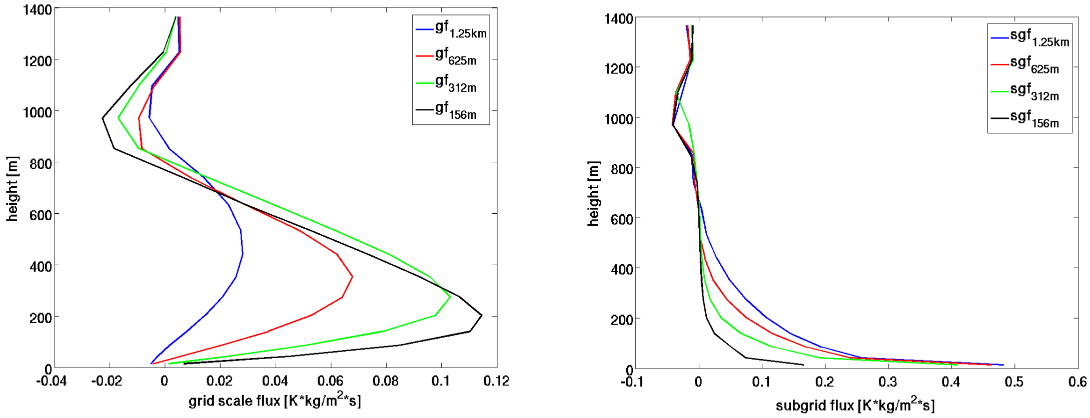

(a) grid-scale flux **(b)** subgrid flux

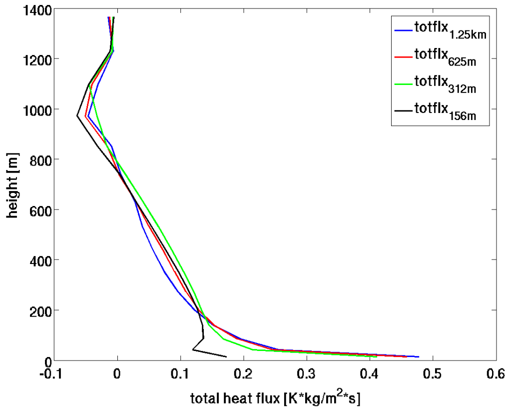

(c) total heat flux

Figure 32. Comparison of domain averaged height plots of (a) grid-scale, (b) subgrid and (c) total heat fluxes $[\frac{K \cdot kg}{m^2 \cdot s}]$ of the new simulation data. Shown are all resolutions for the 24th April 2013 at 12 UTC. Colorbar like in Figure 16.

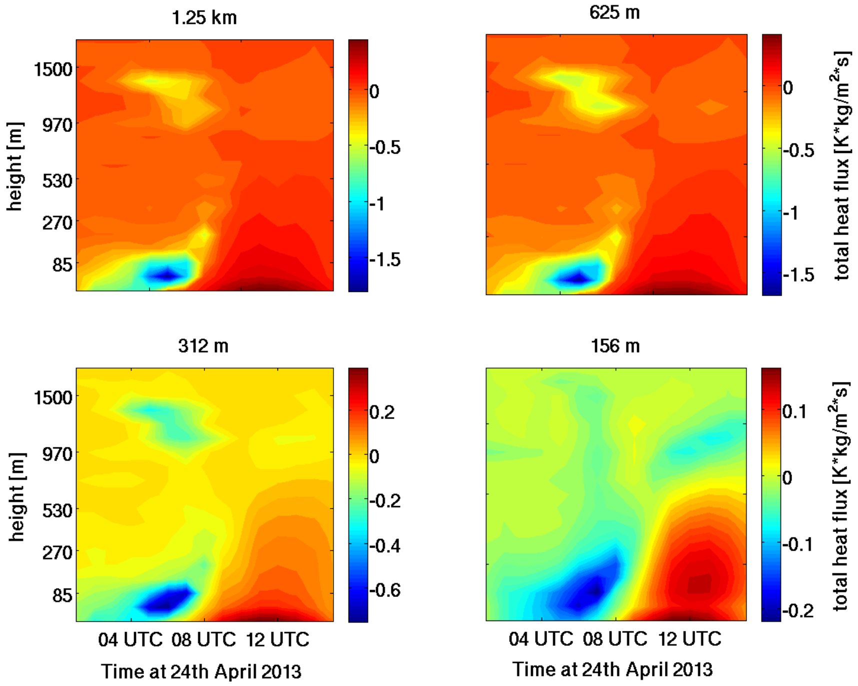

Figure 33. Spatial average of total heat fluxes $[\frac{K \cdot kg}{m^2 \cdot s}]$ contours over height and time. Shown are all resolutions with own colorbar for the 24th of April 2013.

Subgrid scale values of the lowest height level are similar to those of total heat fluxes since the grid resolved fluxes show starting values of nearly zero for all resolutions. It should not be forgotten that these are spatial averages over the selected area for one time step and additionally only one snap shot for the new simulation. Hence, results should be interpreted really carefully and single occasions not overrated.

In order to have a different impression of the data and its temporal evolution, Figure 33 shows the spatial average of total heat fluxes for the new simulation as contour plots over height and time. All colorbars are different in order to be able to see the similar structures of the total heat fluxes through all resolutions as this would not be visible anymore if the widest range of values ascertains the colorbar as it is elsewhere. Biggest values can be found at the lower atmosphere for hours around noon for all resolutions. Smallest values can be found at morning hours and also for the lowest height levels. All resolutions show a round area of smaller values than its surrounding at about 1300 m during 4 to 8 UTC. It should be again noted, that the morning hours are assumed to be spin off time of the model and therefore have to be evaluated with great care. Since the colorbars are chosen to be individual for each resolution, this implies already that total heat fluxes are not in good agreement upon resolutions at all times and height levels.

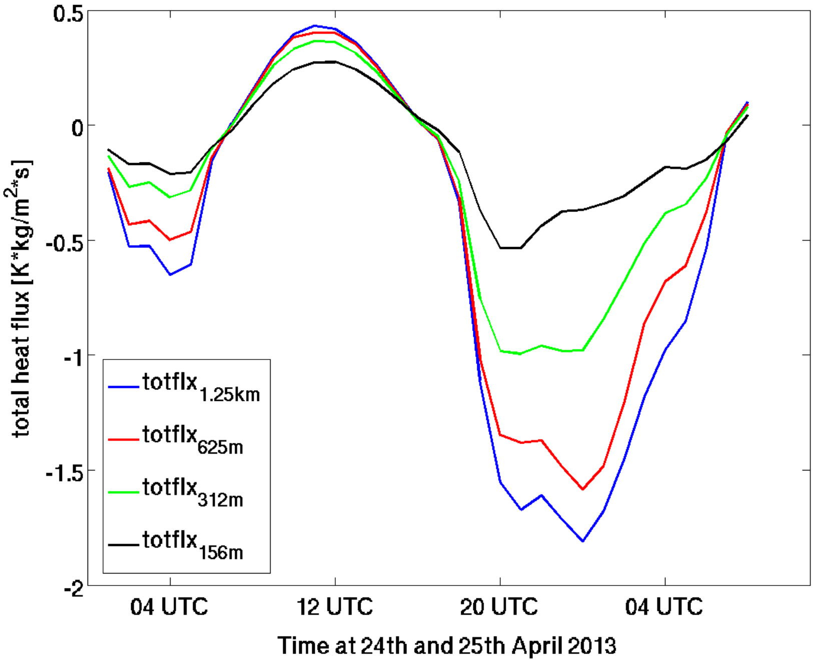

Figure 34. Domain averaged temporal development of total heat fluxes $[\frac{K \cdot kg}{m^2 \cdot s}]$ starting at 00 UTC at 24th until 08 UTC of 25th of April 2013. Shown are all resolutions at 10 m height, with colouring like in Figure 16.

When looking at the temporal development of total heat fluxes in Figure 34 it becomes clear that the 156 m resolution has a much smaller magnitude than the others. This is due to the turbulent diffusion coefficient for heat, K, which is a direct output variable of the model and up to 3 $\frac{kg}{m \cdot s}$ smaller than for the coarsest domain. The temporal development of K for the first model level can be seen in Figure 35. It is clearly visible that the 156 m resolution is different from all coarser resolutions. At this point, it is not clear if the turbulence closure works better for the 156 m resolution or if it is only different. It is also possible that the 312 m resolution remains the most realistic one as it was assumed for the StatSim data. In Figure 34 it can be seen that all resolutions have negative values in the morning hours which corresponds to a flux into the ground and gets positive during daytime and heating of the ground, such that the flux is directed upwards into the atmosphere from about 6 UTC on and turns negative at about 18 UTC, again.

Results so far show a distinct scale dependence of the total heat fluxes and thus of the subgrid scale parameterization. As already pointed out before, the definition and calculation of the turbulent diffusion coefficient for heat, K, seems to have the most important influence on that discrepancy. But with the objective of not drawing conclusions too early, some case studies were conducted with the aim of exploring

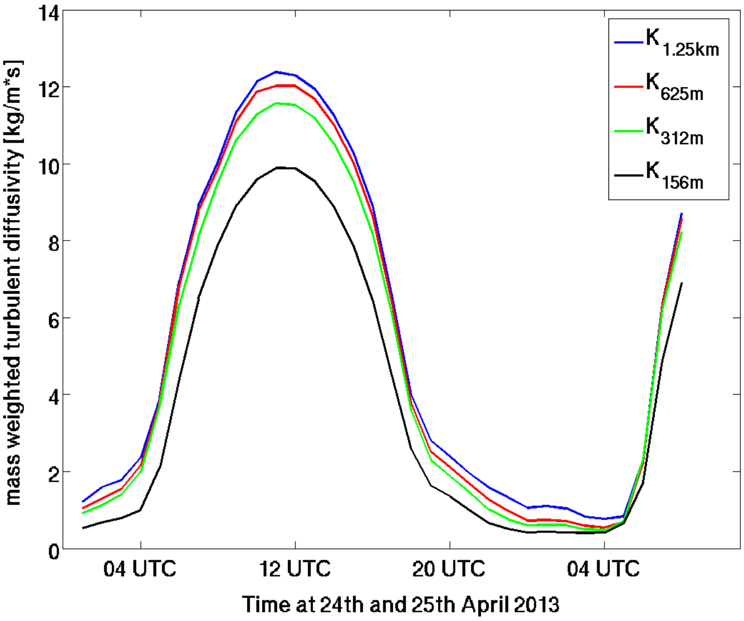

Figure 35. Diurnal cycle of mass weighted turbulent diffusion coefficient for heat $[\frac{kg}{m\cdot s}]$ of the own simulation data at 10 m. Domain averaged for all resolutions starting at 00 UTC at 24th April 2013 until 08 UTC of 25th April. Colorbar like in Figure 16.

the fluxes in different and smaller areas and to see whether other results show scale independence.

6.2.1 Case Studies

In order to be sure that the above explored scale inconsistency is not just a result of averaging over the whole domain, because patterns of all quantities can look completely different at different locations within the domain, some case studies were carried out to explore different regions of interesting turbulent behaviour. To this end, four areas of different total heat flux structures were selected and investigated individually. Figure 36 shows the four areas selected on the basis of total heat fluxes for the 312 m resolution at the lowest model level of the "Status Simulation" data. Case 1 shows the eye-catching point due to the opencast mines (cf. Section 4.2) as regions of outlier values are important for analysing the source of overestimation of total heat fluxes for the coarse resolutions. Case 2 represents an area of total heat fluxes with structures that will not result in an average value of close to zero as it is the case when regarding the whole domain. Cases 3 and 4 are also selected due to containing smaller and bigger values than the average remaining rest of the domain. Additionally, these ar-

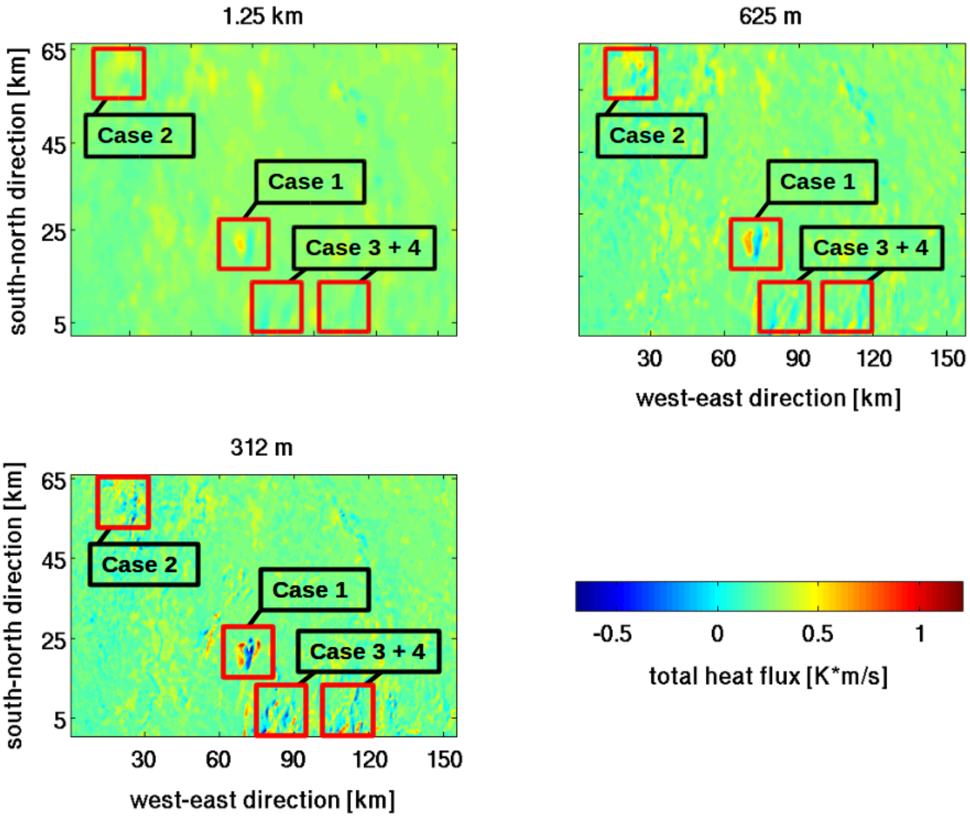

Figure 36. Overview of case selection on the basis of total heat flux $[K \cdot m/s]$ contours of "Status Simulation" data of 24th of April 2013 for all resolutions at 12 UTC and 10 m height.

eas represent the most important challenges for a subgrid parameterization and could reveal helpful information regarding the scale dependence of the Smagorinsky closure. If turbulent heat flux budgets would show good accordance of the resolutions for these or one of these cases, e.g., the turbulence closure could be better classified to certain circumstances.

Looking at height plots of the cases in Figure 37 for subgrid and total heat fluxes, it is visible that all fluxes show qualitatively a similar development throughout the boundary layer. Total heat fluxes agree well upon all resolutions at the lowest height levels, but differ distinctly in nearly all other height levels. Another fact, resulting from the comparison of four different areas, is that the overall shape does not differ

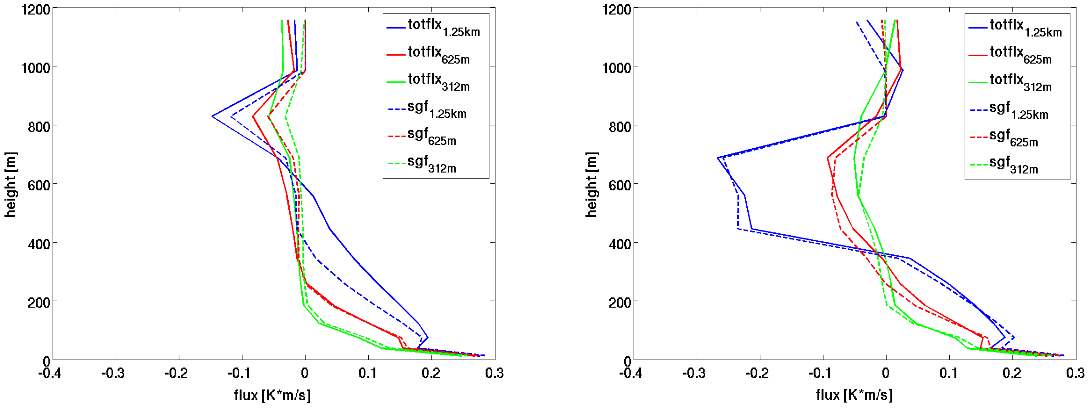

(a) case 1 **(b)** case 2

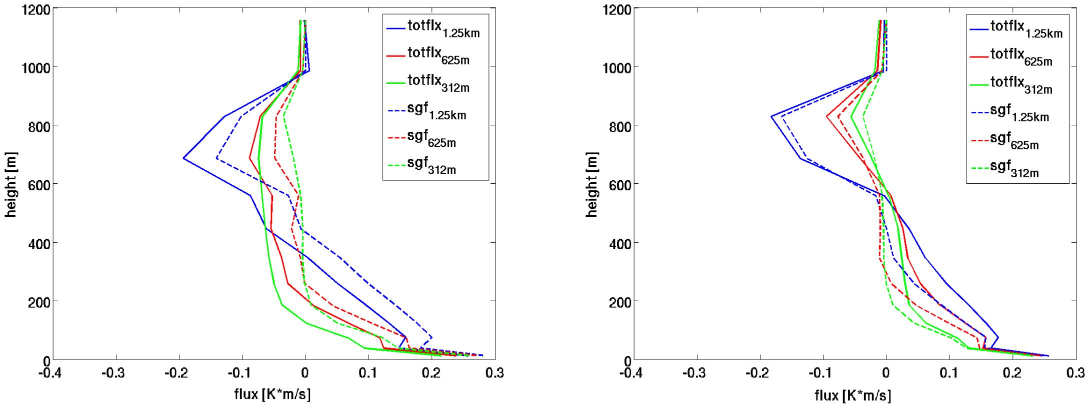

(c) case 3 **(d)** case 4

Figure 37. Comparison of domain averaged height plots for subgrid (--) and total heat (-) fluxes $[K \cdot m/s]$ of "Status Simulation" data. Shown are all cases (1-4) for all resolutions at 12 UTC, 24th of April 2013. Colors of lines like in Figure 14.

significantly from the domain averaged plot of Figure 30. Figure 38 compares the grid resolved fluxes and displays some interesting differences upon the cases. The order of the resolutions should be in the way that the coarsest domain has the smallest values and the highest resolved grid should reveal the greatest values. This was not the case for the averaged values over the whole domain for the StatSim data set (cf. Figure 30). It is also not true for cases 1 and 4, but it is true for case 2 (Figure 38(b)) until about 300 m and changing to the same paradigm as for the other ones in higher levels. Case 3 (Figure 38(c)) has a completely different shape as well as no ascending or descending order of resolutions. For the 312 m resolution, the resolved grid-scale flux reaches the smallest values at nearly every height level. The 625 m resolution reveals the greatest values up to about 800 m and the 1.25 km resolution lies in between the others. Another difference of case 3 compared to all other cases is that the grid resolved fluxes do not start at similar values at the lowest model level as this happens for all other cases. A reason for grid fluxes not to match the theoretical expectations in terms of the order of the resolutions could be due to very small vertical velocity values and especially a domain average of nearly zero. Figure 25 points out that patterns of vertical velocity contain many values around zero or the same absolute value in similar occurrence such that the domain average of vertical velocity adds up to nearly 0 $\frac{K \cdot m}{s}$.

Comparing the 26th April 2013 with the results of two days before, not much differences arise. Total heat fluxes also show a substantial disagreement upon the resolutions, but agree in more of the lower levels than at the other day. This is also visible in the grid scale fluxes, where the expected arrangement of fluxes is also sometimes fulfilled, but for the bulk of height levels it is not.

6.2.2 Probability Density Functions (PDFs)

Frequency distributions give an overview of how the values of the patterns are distributed. Figure 39 serves as an example for the first case at 24th April 2013 at the lowest model level. Note, that frequency and probability density functions (PDFs) have a common axis. The range of values gets larger as the resolution gets higher, which lies within the expectations. Connected with that, peaks are lower as the resolution increases. Red curves are PDFs fitted on to the frequency distributions with the help of a 't location-scale' distribution. It was chosen by a subjective test of different distributions to find out which fits the frequency distribution the best. A PDF is a function that describes the relative likelihood of a variable to take on a given value. The probability density can reach values greater than one and should not be confounded with probability. Hence, higher values of probability density indicate that the value of a quantity is reached more often than values with a lower PDF. Putting the PDFs of all resolutions in one plot, differences are directly visible. Figure 40 shows this for all four cases of the 24th April date at the lowest model level. All cases have in common that the highest peak of the PDF refers to the coarsest resolution, the

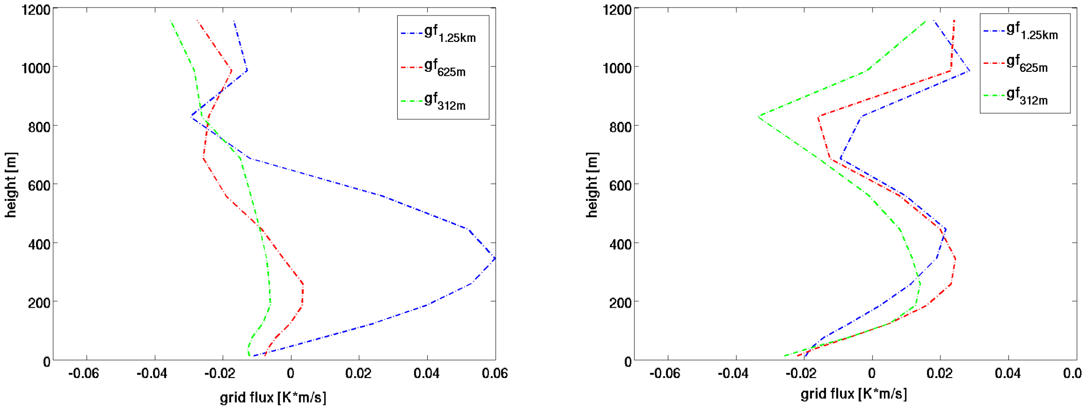

(a) case 1 **(b)** case 2

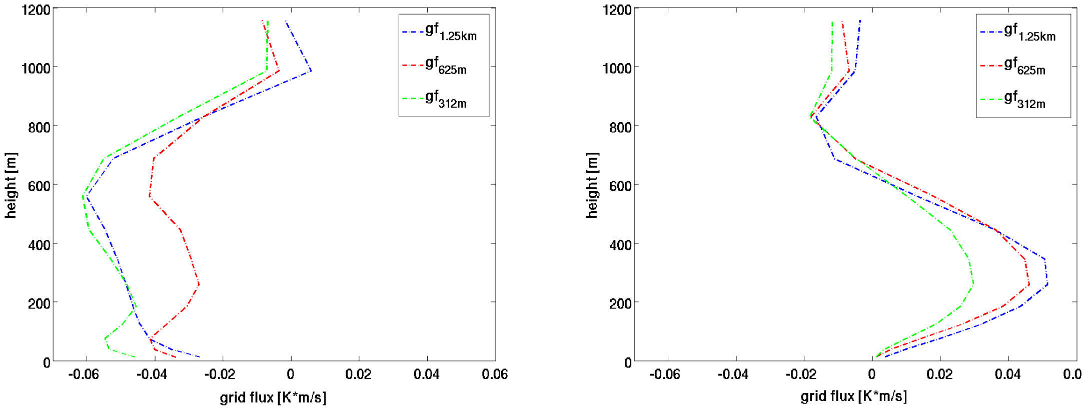

(c) case 3 **(d)** case 4

Figure 38. Comparison of domain averaged height plots for grid resolved fluxes (.-) $[K \cdot m/s]$ of "Status Simulation" data. Shown are all cases (1-4) for all resolutions at 12 UTC, 24th of April 2013. Colors of lines like in Figure 14.

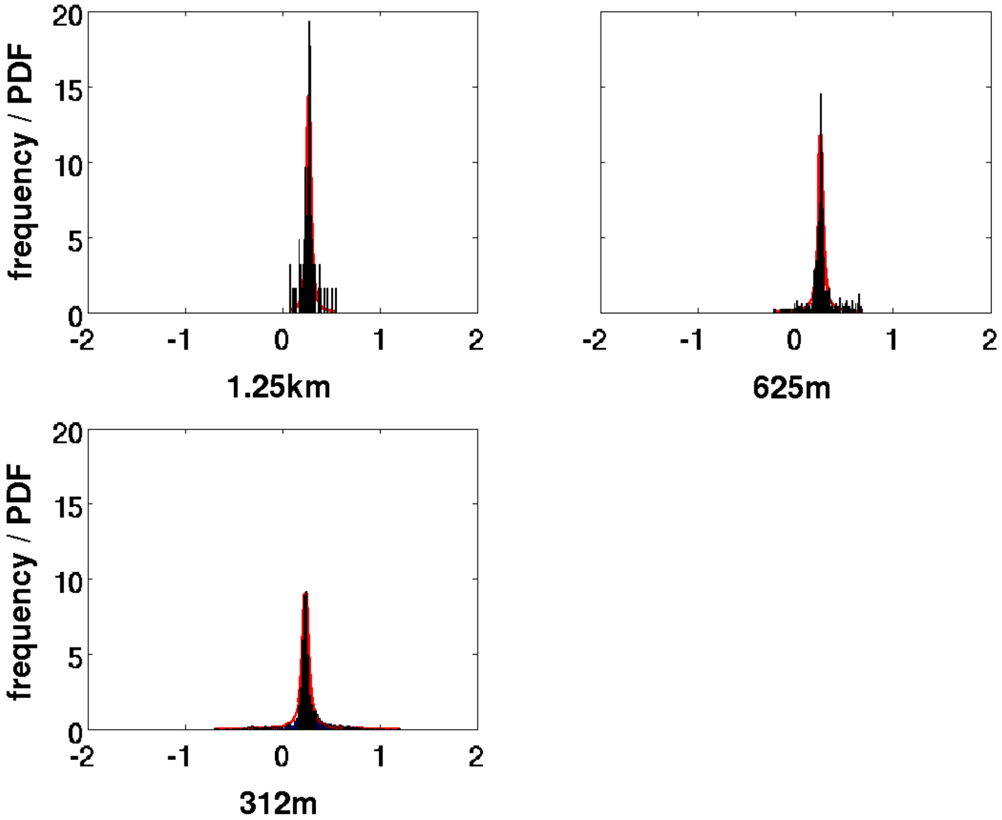

Figure 39. Frequency distribution and PDF of total heat fluxes for all resolutions of the "Status Simulation“ data at 24th April 2013 of case 1 at 10 m height and 12 UTC.

weakest belongs to the highest resolution and the 625 m resolution lies in between. The peak for the 1.25 km resolution is always at a total heat flux value of about 0.25 $\frac{K \cdot m}{s}$ and the peaks for the other grid sizes are slightly shifted to smaller values. As pointed out above, the range of values that occur is wider as the resolution gets higher. The widest range is available for case 1, which can be also seen in Figure 36 which reveals the most intense colors of total heat fluxes.

But as already stated, the lowest model level shows good agreement upon resolutions for almost all fluxes such that it is more interesting to look at other height levels. Figure 41 represents the PDFs of all cases for 680 m. In most of the cases, the arrangement of the resolutions described for Figure 40 is also true, except for case 1. Peaks are at a negative value of $-0.1\ \frac{K \cdot m}{s}$ or zero and also shifted against each other. Furthermore, cases 2 to 4 exhibit a wider range of values for the coarsest resolution at the negative tail in comparison to the highest resolution. Although it is just of small probability density, it should not occur as already stated above. These characteristics are also present for the other height levels that were analysed (cf. Figure 30) and appear also at the 26th April 2013 (not shown here).

As a result of this section can be concluded that the turbulence closure scheme implemented in ICON is strongly scale dependent and needs further improvements in order to fully utilize the possibilities of the scale adaptive grid of ICON. Substantial disagreement exists in terms of total heat fluxes of different resolutions regarding domain averages, contour plots of different height levels and also in the case of taking only small areas into account. In case of the StatSim data, large differences in total heat fluxes are dominant in the middle to upper levels of the atmospheric boundary. Considerable differences on the resolutions also occur for the new simulation data. These differences are dependent on time and are distinct at the lower levels. Grid-scale fluxes do not behave as theoretical considerations evoke, since the order of the different resolutions is not appropriate in case of the StatSim data. The new simulation data proves the theory for the coarsest grid-scale fluxes to reveal the smallest values and the highest resolution to show the biggest values. Subgrid fluxes have the highest influence on the resulting total heat fluxes as they are comparatively larger than the grid resolved fluxes. A comparison of PDFs for all cases at different heights additionally proofs that the scale consistency upon resolutions is not given and, moreover, PDFs are partly not reasonable in terms of theoretical expectations. For example, resolved fluxes are expected to have a wider range of values for the higher resolutions in comparison to coarser grid sizes as they are assumed to reproduce the reality more precisely. They also include more grid points and thus, comprehend more different values. All these findings lead to the need of further investigation of the fluxes in order to understand the processes better and to contribute to an improvement of the turbulence parameterization.

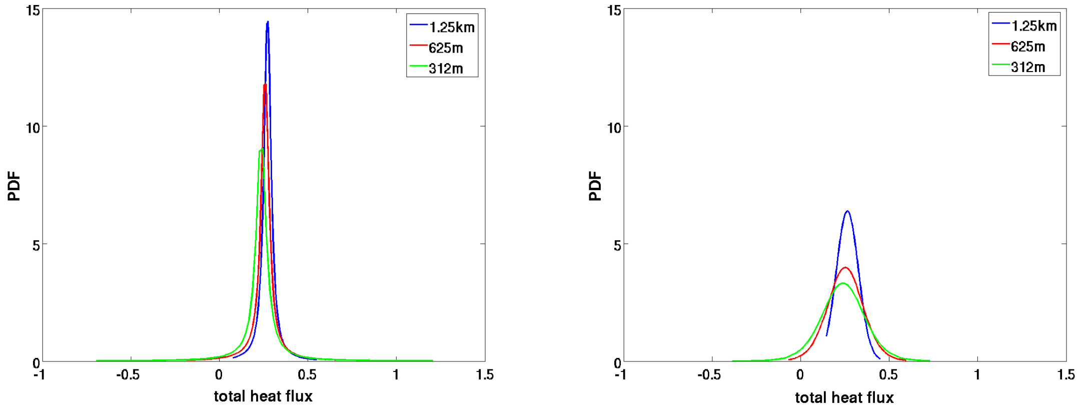

(a) case 1 **(b)** case 2

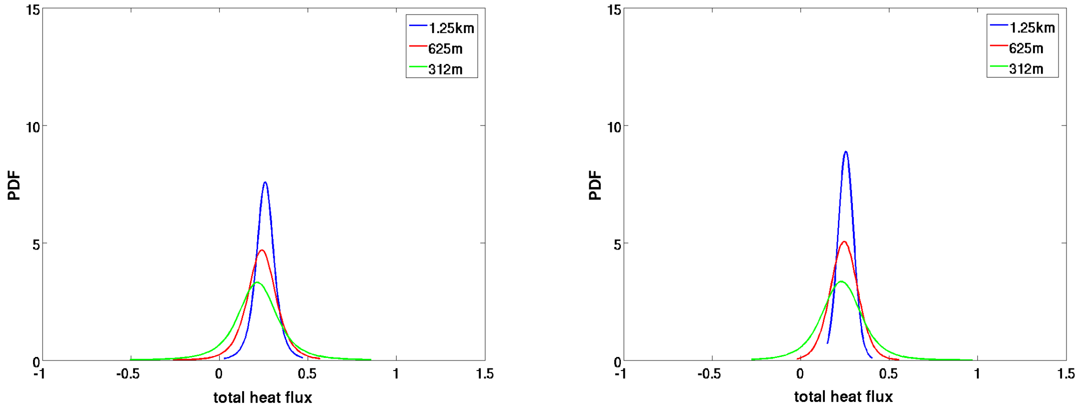

(c) case 3 **(d)** case 4

Figure 40. Comparison of PDFs of total heat fluxes for all resolutions and cases (1-4) of "Status Simulation" data. Shown are all cases (1-4) for all resolutions at 24th April 2103, 12 UTC and 10 m. Colorbar like in Figure 14.

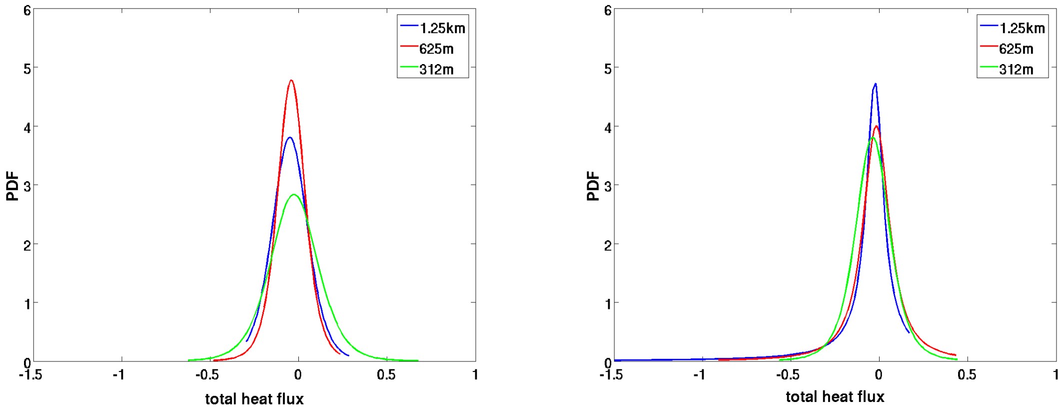

(a) case 1 **(b)** case 2

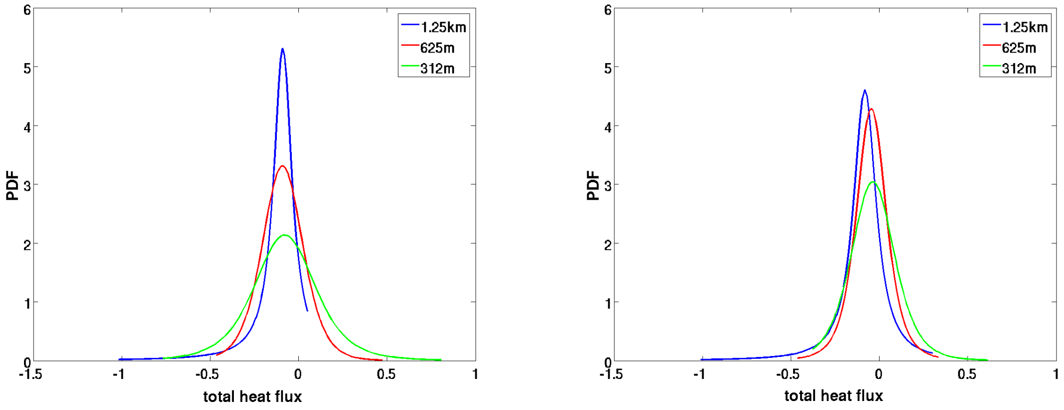

(c) case 3 **(d)** case 4

Figure 41. Comparison of PDFs of total heat fluxes for all resolutions of ”Status Simulation“ data. Shown are all cases (1-4) at 24th April 2103, 12 UTC and 680 m. Colorbar like in Figure 14.

6.3 Flux Behaviour

Now that it is discovered that the subgrid scale parameterization implemented in ICON is scale inconsistent and needs further improvement, different methods, approaches and theoretical considerations are used to explore and understand the flux behaviour better.

6.3.1 Wavelet Analysis

A wavelet analysis was conducted for w and θ separately and put together to a flux matrix (cf. Section 5.4) afterwards. The purpose of this technique is to find out how the fluxes behave on different scales and which scales contribute the most to the subgrid fluxes. Figure 42 displays an overview of how the filtering steps look like for potential temperature at the first day of the “Status Simulation” at 12 UTC for 312 m grid size. For comparison purposes, the colorbars of the input field and all low-passes are the same and all colorbars of the high-passes are the same. Figure 42(a) is the input field of potential temperature and Figures 42(b) and (c) exhibit the first high-pass and low-pass, respectively. The first low-pass shows almost the same pattern as the input field whereas the bulk of values of the first high-pass are zero or around zero. Some small structures ranging from -0.57 K to 0.51 K are mainly present in the western part and some in the north-eastern part of the first high-pass. As an example how the filtering looks like after some further steps, Figures 42(d) and (e) display the fourth filtering step for high-pass and low-pass, respectively. Both patterns are much more coarse than at the first step, but the low-pass pattern is still able to depict the main structures of the input field. The fourth high-pass ranges from values of -0.36 K to 0.40 K and reveals a more or less random pattern with still a high amount of values around zero. Since the last high-pass (θ_1) and the last low-pass (θ_0) are constant fields, the 8th filtering step has very coarse patterns. Thus, Figures 42(f) and (g) exhibit the 7th filtering step. Patterns are already relatively coarse with the high-pass ranging from -0.47 K to 0.61 K and it contains 8 x 3 fields of each the same temperature. 10 of the 24 fields have clearly negative values with 4 additional ones that are around zero. Hence, another 10 fields have positive values with one field of 0.61 K. It is located in the area that reveals the highest potential temperature of the input field. As already described in Section 5.4, the resolution of each low- and high-pass gets coarser with every filtering step. Thus, the 7th low-pass has a resolution of about 40 km. Owing to the axes given in km this could be directly confirmed as the 24 fields of the low-pass reveals 4 complete fields of 40 x 40 km size and four half fields at the bottom of the pattern. Accordingly, Figure 42(e) has a size of 5 x 5 km for the low-pass. The low-pass in Figure 42(g) contains only four complete fields and four half fields with a maximum of 290.67 K and a minimum of 289.62 K. Higher potential temperatures are located at the south-east of the pattern and smaller values are at the northern part and in the west. Hence, it only reveals information on the very coarse potential temperature distribution of this domain and the high-pass of this filtering step adds

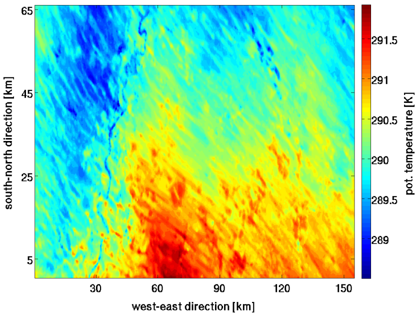

(a) Input field θ_{312m}

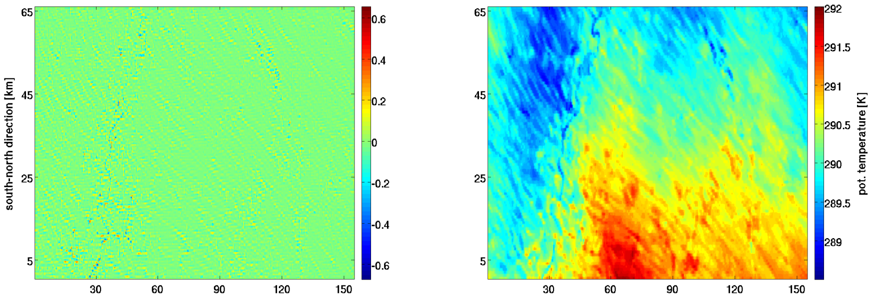

(b) θ_9 (1st high-pass) **(c)** 1st low-pass

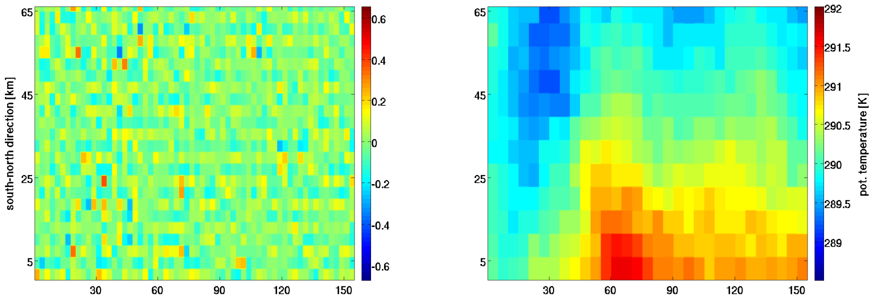

(d) θ_6 (4th high-pass) **(e)** 4th low-pass

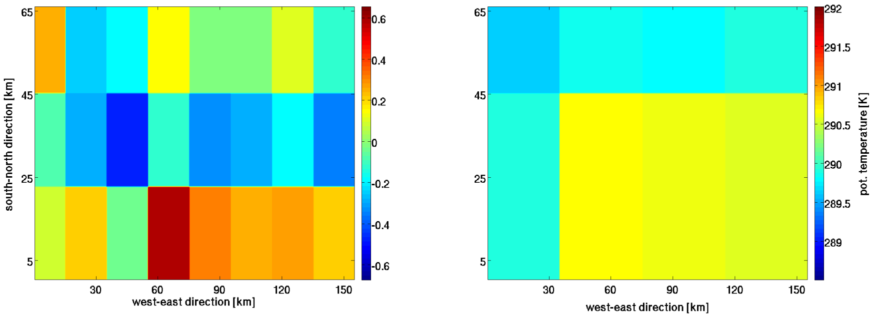

(f) θ_2 (7th high-pass) **(g)** 7th low-pass

Figure 42. Input field θ_{312m} [K] with high- and low-pass examples of "Status Simulation" data at 12 UTC of 24th April 2013 at 10 m. (a) is the original field, (c), (e), (g) are low-pass filtered fields and (b), (d), (f) are the corresponding high-passes.

information on some areas of deviations from the averaged low-pass pattern.

Results of flux-matrices for the 24th, case 1 at 24th and 26th April 2013 date can be seen at the end of this Section in landscape format. Interpreting the values of these matrices has to be done very carefully, because it is not totally clear what, e.g., the multiplication of w_0 with θ_9 really represents. The scales are mixed and resulting values in the matrix could be either highly influenced by one (w_0) or the other scale (θ_9). It could be also the case that they have no physical significance at all. However, some main conclusions based on these flux-matrices can be drawn. Numbers in the lower right corner (highlighted in yellow) are bigger than all others and especially in comparison to the ones of the upper left corner (highlighted in light pink), which are relatively small compared to the rest of values. This pattern of small values in the upper left and bigger ones at the lower right can be explored for every flux-matrix of both days and also for all cases (only one case shown here). Thus, it can be seen as a common behaviour and it is concluded that the larger scales (lower right corner) contribute the most to the subgrid fluxes. This underlines the critical view on the K-theory that is also already stated in the theory Section 2.2.2. K-theory is a local closure and therefore assumes the small scales to contribute the most to the subgrid flux, but this is not true for atmospheres where eddies of larger sizes are present. Flux matrix analysis of ICON modelling data confirms this considerations accompanied by emphasizing the importance of the diffusion coefficient, K.

Flux-matrix for 24th April 2013 of “Status Simulation” data for the 312 m resolution at 10 m with 9 filtering steps.

$$\mathbf{N}_{24th} = \begin{bmatrix}
1,3283e-14 & -1,7330e-13 & -4,7112e-14 & 6,0350e-11 & 1,6116e-10 & -2,9219e-10 & -8,9176e-10 & 2,4035e-08 & 5,4344e-10 & 5,6719e-05 \\
4,6484e-15 & -6,0650e-14 & -1,6487e-14 & 2,1120e-11 & 5,6401e-11 & -1,0225e-10 & -3,1208e-10 & 8,4112e-09 & 1,9018e-10 & 1,9849e-05 \\
-1,2202e-13 & 1,5921e-12 & 4,3279e-13 & -5,5441e-10 & -1,4805e-09 & 2,6842e-09 & 8,1921e-09 & -2,2079e-07 & -4,992e-09 & -5,2104e-04 \\
9,3131e-12 & -1,2151e-10 & -3,3032e-11 & 4,2314e-08 & 1,1300e-07 & -2,0487e-07 & -6,2525e-07 & 1,6852e-05 & 3,8103e-07 & 0,0398 \\
-1,8268e-12 & 2,3835e-11 & 6,4795e-12 & -8,3002e-09 & -2,2165e-08 & 4,0186e-08 & 1,2265e-07 & -3,3056e-06 & -7,4742e-08 & -0,0078 \\
-1,1389e-11 & 1,4859e-10 & 4,0394e-11 & -5,1744e-08 & -1,3818e-07 & 2,50522e-07 & 7,6460e-07 & -2,0607e-05 & -4,6595e-07 & -0,0486 \\
1,4559e-11 & -1,8995e-10 & -5,1638e-11 & 6,6148e-08 & 1,7665e-07 & -3,2026e-07 & -9,7744e-07 & 2,6344e-05 & 5,9565e-07 & 0,0622 \\
-5,2843e-11 & 6,8946e-10 & 1,8743e-10 & -2,4009e-07 & -6,4116e-07 & 1,1624e-06 & 3,5477e-06 & -9,5618e-05 & -2,1620e-06 & -0,2256 \\
7,8652e-12 & -1,0262e-10 & -2,7896e-11 & 3,5735e-08 & 9,5430e-08 & -1,7301e-07 & -5,2804e-07 & 1,4232e-05 & 3,2179e-07 & 0,0336 \\
-3,9282e-10 & 5,1253e-09 & 1,3933e-09 & -1,7848e-06 & -4,7662e-06 & 8,6411e-06 & 2,6373e-05 & -7,1079e-04 & -1,6071e-05 & -1,6774
\end{bmatrix}$$

Flux-matrix for 26th April 2013 of “Status Simulation” data for the 312 m resolution at 10 m with 9 filtering steps.

$$\mathbf{N}_{26th} = \begin{bmatrix}
6,6731e-16 & -5,6027e-14 & 6,8272e-14 & -1,0449e-10 & -2,1259e-10 & -1,5378e-10 & 5,5366e-10 & -1,9420e-08 & 5,2521e-09 & -2,5002e-05 \\
-6,2878e-15 & 5,2792e-13 & -6,4330e-13 & 9,8455e-10 & 2,0031e-09 & 1,4490e-09 & -5,2169e-09 & 1,8299e-07 & -4,9488e-08 & 2,3559e-04 \\
8,8691e-15 & -7,4465e-13 & 9,0739e-13 & -1,3887e-09 & -2,8255e-09 & -2,0439e-09 & 7,3586e-09 & -2,5811e-07 & 6,9804e-08 & -3,3230e-04 \\
4,7893e-13 & -4,0211e-11 & 4,8999e-11 & -7,4992e-08 & -1,5257e-07 & -1,1037e-07 & 3,9736e-07 & -1,3938e-05 & 3,7694e-06 & -0,0179 \\
1,2549e-12 & -1,0536e-10 & 1,2839e-10 & -1,9650e-07 & -3,9978e-07 & -2,8920e-07 & 1,0412e-06 & -3,6520e-05 & 9,8768e-06 & -0,0470 \\
-2,9652e-13 & 2,4896e-11 & -3,0337e-11 & 4,6429e-08 & 9,4463e-08 & 6,8334e-08 & -2,4602e-07 & 8,6292e-06 & -2,3338e-06 & 0,01111 \\
-7,8699e-12 & 6,6076e-10 & -8,0517e-10 & 1,2323e-06 & 2,5071e-06 & 1,8137e-06 & -6,5296e-06 & 2,2903e-04 & -6,1940e-05 & 0,2949 \\
-1,4691e-11 & 1,2335e-09 & -1,5031e-09 & 2,3004e-06 & 4,6803e-06 & 3,3857e-06 & -1,2189e-05 & 4,2755e-04 & -1,1563e-04 & 0,5505 \\
8,5360e-12 & -7,1669e-10 & 8,7331e-10 & -1,3366e-06 & -2,7193e-06 & -1,9672e-06 & 7,0823e-06 & -2,4841e-04 & 6,7183e-05 & -0,3198 \\
-2,8622e-10 & 2,4031e-08 & -2,9283e-08 & 4,4817e-05 & 9,1181e-05 & 6,5960e-05 & -2,3747e-04 & 0,0083 & -0,0023 & 10,7239
\end{bmatrix}$$

Flux-matrix for 24th April 2013 of “Status Simulation” data for the 312 m resolution of case 1 (cf. Section 6.3.1) at 10 m and for 6 filtering steps as further filtering steps are already zero for the high-passes.

$$\mathbf{N}_{24th,c1} = \begin{bmatrix} \text{-4,01e-12} & \text{2,71e-11} & 3,00e-09 & 7,45e-09 & -8,56e-09 & 9,02e-08 & 6,0910e-04 \\ \text{-2,38e-10} & 1,60e-09 & 1,78e-07 & 4,41e-07 & -5,08e-07 & 5,35e-06 & \text{0,0361} \\ -4,33e-09 & 2,92e-08 & 3,24e-06 & 8,03e-06 & -9,23e-06 & 9,73e-05 & \text{0,6568} \\ -1,90e-09 & 1,28e-08 & 1,42e-06 & 3,53e-06 & -4,06e-06 & 4,28e-05 & \text{0,2889} \\ 1,88e-08 & -1,27e-07 & -1,41e-05 & -3,49e-05 & 4,02e-05 & -4.2346e-04 & \text{-2,8591} \\ 4,69e-08 & -3,17e-07 & -3,52e-05 & -8,71e-05 & 1,0020e-04 & \text{-0,0011} & \text{-7,1281} \\ 2,67e-09 & -1,80e-08 & -2,00e-06 & -4,96e-06 & 5,70e-06 & -6,01e-05 & \text{-0,4058} \\ \end{bmatrix}$$

6.3.2 $\widetilde{K}$ vs. K

As all the adjustable information about subgrid turbulence is contained in the turbulent diffusion coefficient for heat, K, this quantity has to be analysed in more detail. A first approach is to examine which K values of the coarser resolutions would be necessary in order to result in the same total heat flux as the highest resolution. Since the highest resolution is assumed to be the best approximation to nature, it is declared to be the reference. In case of the "Status Simulation", total heat flux of the 312 m resolution serves as reference and in case of the new simulation it is the 156 m resolution. Equation (57) demonstrates the calculation of a new turbulent diffusion coefficient for heat, $\widetilde{K}$, for the 1.25 km resolution as an example and uses the notation of the methods Chapter 5.

$$\widetilde{K}_{1.25km} = -\frac{flx_{325m|156m} - gf_{1.25km}}{\frac{d\theta}{dz}_{1.25km}}, \tag{57}$$

where $flx_{325m|156m}$ is the total heat flux for the highest resolution of the chosen data set and $gf_{1.25km}$ is the grid resolved flux of the 1.25 km resolution. In contrast to the assumption that K is a non-negative value (cf. Section 2.2.2), many negative K' values occur. Like it is already described in Section 2.2.2, this can happen when the small-eddy K-theory is used in convective boundary layers where large eddies are present. In addition, negative values can occur out of mathematical considerations if either the potential temperature gradient or the difference of total heat flux and grid-scale flux is positive or if both are negative. Comparing height plots of potential temperatures, e.g., Figure 30 demonstrates that a positive potential temperature gradient is always present above about 400 m height and at this height, spatial averaged total heat fluxes are negative, while grid fluxes alternate around zero. The calculated $\widetilde{K}$ values are plotted against the old K values of the respective resolution as a scatterplot. Expected are two separated point clouds which represent the two basic types of subgrid fluxes, namely the turbulent diffusion type, which is parameterized by the Smagorinsky closure and the convective type that causes non-traditional turbulence and is assumed not to be parameterized satisfactorily in ICON so far.

In order to be able to compare the fields of 312 m resolution in case of the "Status Simulation" data with the fields of, e.g., 1.25 km, the matrices had to be of the same size. To this end, matrices of 625 m and 1.25 km were filled with values to get the same size as the 312 m resolution. This was done in the following way as an example for 625 m grid size:

$\frac{\partial\theta}{\partial z}|_{625m} = \begin{bmatrix} 1 & 2 & 3 \\ 4 & 5 & 6 \end{bmatrix}$ will be extended to

$$\widetilde{\frac{\partial\theta}{\partial z}}|_{625m} = \begin{bmatrix} 1 & 1 & 2 & 2 & 3 & 3 \\ 1 & 1 & 2 & 2 & 3 & 3 \\ 4 & 4 & 5 & 5 & 6 & 6 \\ 4 & 4 & 5 & 5 & 6 & 6 \end{bmatrix},$$

resulting in the same matrix size as the 312 m resolution. In case of the new simulation, all matrix sizes are brought to the 156 m grid size. First results did not reveal any usable plots as they show a scatter of a very wide range of both, positive and negative values which are most dense around zero or small values for nearly all height levels analysed. Furthermore, as many positive as negative values exist, regardless of the height level, day or simulation, except for the lowest model level. Figure 43 shows four plots of calculated $\widetilde{K}$ against model output K for both analysed days and for 1.25 km and 625 m resolution of the "Status Simulation" at the lowest model level. The bulk of the depicted values seem to concentrate around the identity line, (1,1), if K and $\widetilde{K}$ would take on the same values. Note, that the y-axes are chosen to reveal the biggest amount of data and not all data points are shown here. Values on the (1,1) line imply that the same K value would be necessary for both resolutions to result in the same total heat flux. It is assumed that this is not the case for the bulk of values. Figure 43(a) is the only plot that exhibits only a few negative values and seems to reveal meaningful values for $\widetilde{K}$, although the y-axis is limited to a range of values that contains most of the points, as it is also the case for all other plots. The occurrence of some very big outlier points is not unusual, but it was not expected to explore such a big amount of it. Values of, e.g., 7 x 10^4 m^2/s for 26th April and 1.25 km grid size at 680 m level are no exception. All other height levels look similar to Figures 43(b)-(d). Uncertainties that come along with filling the fields are not assessable. Therefore, another possibility was chosen to sustain the same matrix sizes. Averaging fields of the higher resolved resolutions yield the same matrix size as for the 1.25 km resolution. This was done in following manner as an example for the 312 m resolution:

$$\frac{\partial\theta}{\partial z}|_{312m} = \begin{bmatrix} 1 & 2 & 3 & 4 & 5 & 6 \\ 7 & 8 & 9 & 10 & 11 & 12 \\ 13 & 14 & 15 & 16 & 17 & 18 \\ 19 & 20 & 21 & 22 & 23 & 24 \end{bmatrix} \text{ will be averaged to}$$

$$\widetilde{\frac{\partial\theta}{\partial z}}|_{312m} = \begin{bmatrix} 4.5 & 6.5 & 8.5 \\ 16.5 & 18.5 & 20.5 \end{bmatrix},$$

resulting in the same matrix size as the 625 m resolution. Repeating this method leads to the same matrix size as for the 1.25 km resolution. Nearly the same output results are produced with this method, especially in terms of the distribution of $\widetilde{K}$ against K values. Having a closer look on the input fields of total heat fluxes, like displayed in Figure 28, led to a third idea of getting better results. Small phase errors and/or different sizes and shapes of the leading structures of total heat flux pattern may lead

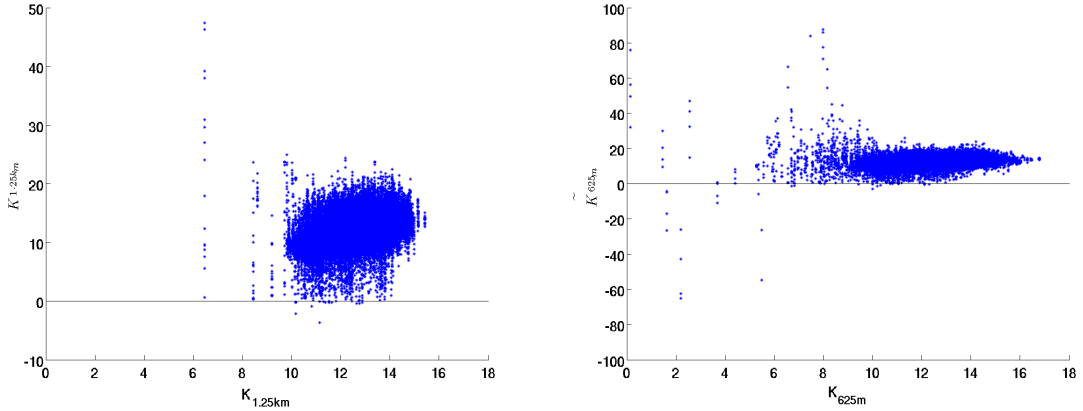

(a) 24th 1.25 km **(b)** 24th 625 m

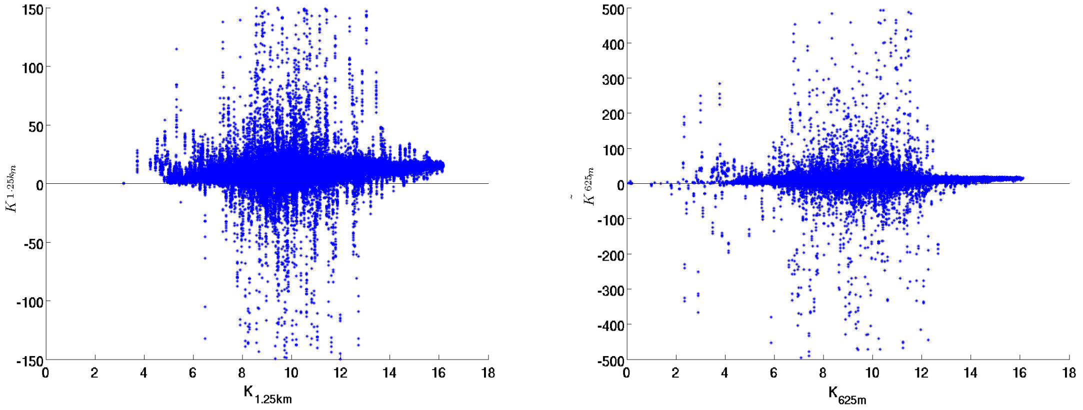

(c) 26th 1.25 km **(d)** 26th 625 m

Figure 43. Calculated $\widetilde{K}$ based on 312 m resolution against model output K for "Status Simulation" data at 12 UTC and 10 m height. (a) for 24th and 1.25 km resolution, (b) for 24th and 625 m resolution, (c) at 26th and 1.25 km resolution and (d) at 26th April 2013 and 625 m resolution. Note the different y-axes ranges.

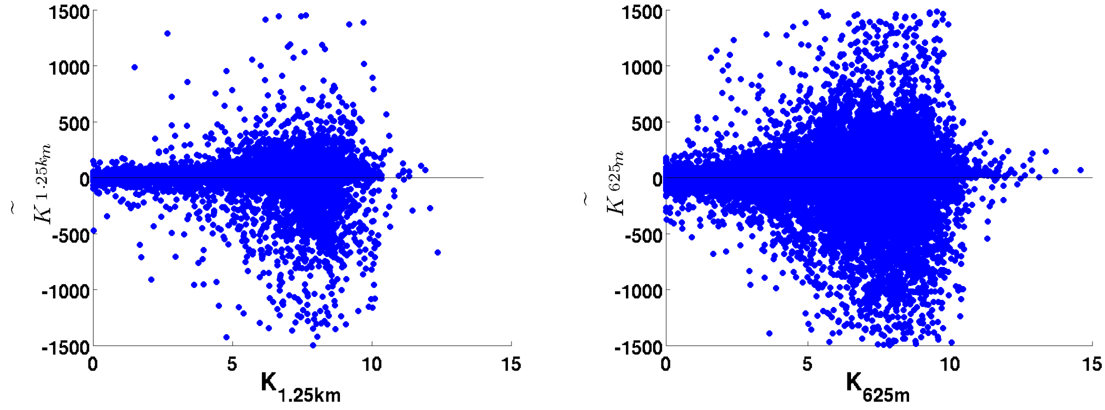

(a) 1.25 km (b) 625 m

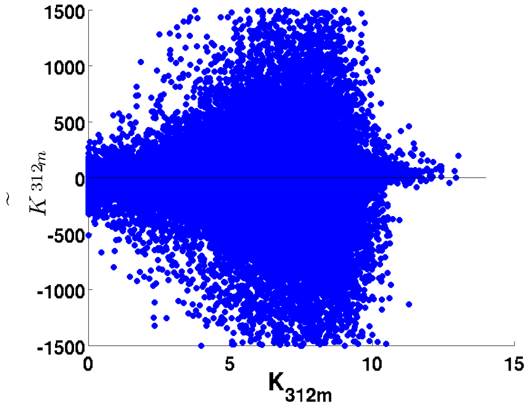

(c) 312 m

Figure 44. Calculated $\widetilde{K}$ based on 156m resolution against model output of 24th April 2013 at 10 m for the new simulation data at 12 UTC and all coarse resolutions (a) 1.25 km, (b) 625 m and (c) 312 m.

to wrong and too much negative values. To tackle this idea, fields of total heat fluxes of the lowest height level were taken as the basis for adjusting the fields of resolutions 625 m and 312 m to the maxima of the coarse pattern. Smaller common fields is the result of shifting the patterns in order to match the maxima at the same location. Both ways of receiving the same matrix sizes after shifting the maxima, led to similar results as before. All input fields were inspected in great detail, but no error could be discovered. Another possible source to cause that amount of negative and large absolute values could be the different shapes of the structures that can not be influenced without distorting the simulation data. Applying this method to cases 1 and 2 (cf. Figure 36 of Section 6.2) did not bring any improvements of the distributions of $\widetilde{K}$ against K values, especially at higher levels.

All the different attempts of obtaining new information about how the K values could be improved led to no useful results. The conclusion is that the structure of the patterns of the quantities are not useful for this methods. Accordingly, this was one reason for the decision to conduct a new simulation with hopefully better results. But data look in principle the same, as it was already pointed out in Sections 6.1 and 6.2. For the sake of completeness, Figure 44 constitutes $\widetilde{K}$ against K values of the new simulation for the lowest model level of resolutions 1.25 km, 625 m and 312 m as they were all based on the 156 m grid size. Again, the bulk of points are centered around the zero line and reach very high absolute values with about the same rate of occurrence in positive and negative values. Again, y-axes are restricted to reveal the most dense amount of points.

During all the investigation of how the fluxes behave, some theoretical considerations came up, which will be explained in detail and summarized in two hypotheses in the following two sections.

6.3.3 Hypothesis 1

The overall aim of a scale independent turbulence closure is that all resolutions have to result in the same total heat flux. As pointed out before, the Smagorinsky closure assumes that the mixing length, l, is proportional to the grid size, Δ:

$$l \propto \Delta \propto (\Delta x \Delta y \Delta z)^{1/3}. \tag{58}$$

This is possibly not valid for the grid sizes used in this thesis and also used by many other colleagues working with ICON-LEM (e.g. Heinze et al. [2017]). The resolutions of the “Status Simulation” data are all larger than the typical size of eddies (c.f. Figure 45). The conceptual drawn energy spectrum of Figure 45 shows a peak caused by turbulent eddies at about 100 m and the utilized grid sizes of 312, 625 and 1250 m are all greater than the 'turbulent scales'. Since the mixing length, l, is a measure of the ability of turbulence to cause mixing (cf. Chapter 2) and the turbulent heat fluxes are overestimated for the coarse resolutions, the first hypothesis is to change the mixing length definition. Taking results of Chapter 6 into account, this hypothesis proposes that it would be a better approximation to use the same mixing length for all three resolutions of the StatSim data. The new simulation data shows a different behaviour of the fluxes for the highest resolution of 156 m. The reason could be that a grid size of 156 m is small enough for the Smagorinsky closure to work better or at least different. Accordingly, the hypothesis is defined for grid sizes that are larger than a critical value, Δ_c, such that an overestimation of the fluxes of the coarser grid sizes could be avoided:

$$l = \begin{cases} (\Delta x \Delta y \Delta z)^{1/3} & \text{for } \Delta < \Delta_c \\ \text{const. } (l_{mix}) & \text{for } \Delta \geq \Delta_c. \end{cases} \tag{59}$$

Based on the considerations so far, Δ_c can be about 200 m, but this value has to be further explored with the help of simulations with higher resolutions. Being able to compare smaller grid sizes as the 156 m resolution to the results of this thesis could provide more information on the explored differences for the 156 m resolution compared to the coarser grid sizes. The hypothesis can be tested by taking the initial conditions of the new simulation and changing the definition of the mixing length to a constant value. This value could be further specialized by running different simulations with different values. Suggested values are, e.g., 1/2, 1/4 and 3/4 of the boundary layer height or a dependence on the resolution which is assumed to be the reference grid size that is closest to reality. In case of the StatSim data, this would be the 312 m resolution. It is more difficult for the new simulations, since it is not known if the turbulence closure works better or only different for the 156 m resolution. Accordingly, both resolutions, 156 and 312 m, should be tested in different simulation runs.

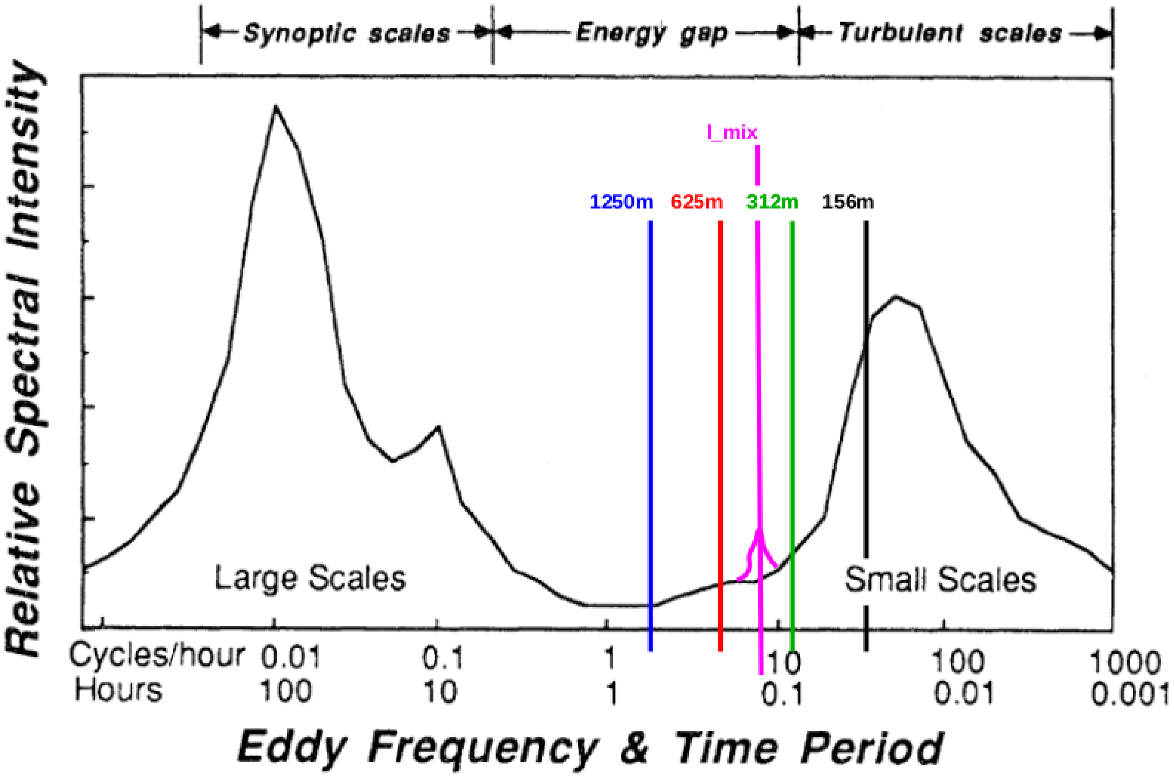

Figure 45. Conceptual plot of energy spectrum for turbulence with added resolutions used in this thesis and a mixing length scale (l_{mix}), which is independent of the grid resolution. Source of basic figure: Stull [1988].

6.3.4 Hypothesis 2

As already pointed out before, it is necessary to have a closer look at the Smagorinsky parameterization scheme used in the ICON model in order to find out where possible errors arise. It was also emphasized that the turbulent diffusion coefficient for heat, K, has the largest influence on the subgrid fluxes. As a conceptual view, equation (60) shows how K is determined in the ICON model code.

$$K \propto f(Ri) \cdot D_{ij} \cdot \Delta \tag{60}$$

D_{ij} is the mechanical production term (c.f. Section 2.3.1) and it is unlikely that the observed differences are related to this term as it only consists of prognostic variables. Two other parts are remaining which could have some influence on the results. At first, $f(Ri)$, a function of the Richardson number (Ri), describes in essence if the turbulence is increasing or decreasing, or in a descriptive way: if the flow is laminar or turbulent and out of this, if further turbulence will be produced or if turbulence will decline. This part is probably not the dominating term, although a little chance remains that this could cause the deviations, because the critical Richardson number is rather arbitrary and may cause differences in results. The precise form of $f(Ri)$ is as follows (source: ICON code, module 'mo_sgs_turbulence.f90'):

$$f(Ri) = \sqrt{(1 - Ri/Pr)}, \tag{61}$$

with the Richardson number defined as in equation (62) and $Pr = \frac{c_p \mu}{k}$ as Prandtl number with c_p as specific heat, μ as dynamic viscosity and k as thermal conductivity.

$$Ri = \frac{g}{\theta} \cdot \frac{\frac{\delta\theta}{\delta z}}{D_{ij}} \tag{62}$$

Further simplifications are made in the ICON code, e.g., replacing the Richardson number by a term of the Brunt-Vaisala frequency. This means that the function $f(Ri)$ contains some assumptions made on fluid properties and has not a big influence regarding equation (61), because $Pr \sim 0.7 - 0.8$ and $Ri < 1$ are for a turbulent atmosphere always very small numbers such that they will not have a big influence. The last remaining part is the proportionality to the grid size, Δ, and coupled with that, again the mixing length (cf. hypothesis 1 in Section 6.3.3). The definition of this relation could be a possible explanation for the overestimation of the coarser resolutions, because it influences the result distinctly.

Further considerations of possible error sources go back to the basic idea behind the Samgorinsky-type of closure. Equation (60), e.g., demonstrates that the fluxes are determined by scale turbulence of similar size as the grid spacing. The introduction of $f(Ri)$, does not change this concept as it only makes the intensity of the subgrid turbulence to be dependent on thermal stability. This concept fails in situations when subgrid mixing occurs on a scale, l_{mix} (cf. Figure 45), which is independent of grid resolution, or if the subgrid mixing occurs on several scales, one with l_{mix} which does not depend on grid resolution, and one with l_{con} which does change with grid resolution. For example, l_{con} may be related to convection or topographic effects. Accordingly, another idea is that regions with small subgrid activities or topography effects which cause non-traditional turbulence are not considered in the Smagorinsky closure. Furthermore, no additional convection scheme is used in the ICON-LEM, because it is assumed that convection is fully resolved in LES configuration.

To concretise the above stated ideas, total heat fluxes (F_Λ) of a given resolution, Λ, can be divided into motion close to the grid scale (meso-scale convection) and motion far from the grid scale (turbulence):

$$F_\Lambda = F_{\Lambda_1} + F_{\Lambda_2}, \tag{63}$$

with F_{Λ_1} as meso-scale convection and F_{Λ_2} as turbulence. The latter one can be computed using the improved closure of hypothesis 1 with a better chosen mixing length definition. The meso-scale convection depends on atmospheric stability and is not always present in the atmosphere. An occurrence probability, α_1, for meso-scale convection to develop has to be added to the calculation. An equation based on this ideas gives a formulation of the second hypothesis:

$$F_{\Lambda_1} = -\alpha_1 K_1 \frac{\partial \overline{\theta}}{\partial z}, \tag{64}$$

with K_1 such as adapted for hypothesis 1 as a first simplification.

To summarize the concept of both hypotheses, the Smagorinsky turbulence closure implemented in ICON is assumed to be sufficient enough and needed for regions with strong subgrid activities like the conceptual figure of the energy spectrum (Figure 45) denotes as 'turbulent scales'. But this closure leads to an overestimation of the coarse resolutions when weak subgrid activities are additionally present, like it is observed for the highest resolution of the “Status Simulation” data and presumably for the 156 or 312 m resolution of the new simulations. Thus, the definition of the mixing length has to be adapted and it has to be additionally accounted for non-traditional turbulence caused by topography or convection. To this end, an additional probability for meso-scale convection to occur has to be introduced.

7 Conclusions

This chapter concludes all gained results and hypotheses in Section 7.1, with regard to investigating ICON model output and contributing to an improvement of the turbulence closure scheme. Section 7.2 gives an outlook to future steps and some further improvements that could be made in order to have better and more reasonable results as a basis for the hypotheses. In addition, it proposes some investigations that could be conducted with the available data sets concerning an improved turbulence parameterization.

7.1 Summary and Discussion

The aim of this work is to investigate the turbulence closure scheme implemented in the newly developed ICON model with regard to scale consistency and to contribute to an improvement of the parameterization scheme. This is of great importance due to the scale adaptive capability of the icosahedral grid of this model and the accompanied new requirements on a scale independent solution for the subgrid scales. For this purpose, simulation data of the ICON model was evaluated against a rough overview of observations and own simulation data was conducted. Furthermore, two data sets were analysed with regard to scale consistency of the different grid resolutions used. To this end, different tools like probability density functions or operating case studies were utilized. After being able to conclude that the turbulence closure is not scale consistent upon all resolutions, methods were developed to investigate the behaviour of subgrid turbulence as it is very important to understand the underlying processes better. Especially the turbulent diffusion coefficient for heat, K, is of big importance for the subgrid parameterization and needs to be investigated in more detail. In the end, two hypotheses are proposed to improve the representation of K in the turbulence closure scheme.

Conducting simulations with ICON is not always intuitive. Some of the variables needed for this thesis and analysis, such as subgrid quantities, have to be additionally stored by the user, because there is only a pre-defined set of variables available. Much effort has been done to implement the calculation of subgrid and grid resolved heat fluxes in the ICON code. But in the case of subgrid fluxes, results were always zero and in the case of grid resolved fluxes, results showed no reasonable values. Furthermore, the output did not show the already explained and expected order of resolutions for grid resolved fluxes. The order was the opposite of what is expected, with the coarser resolutions having the highest absolute values and the smallest for the finest resolution. However, calculating the grid resolved flux with help of vertical velocity and potential temperature led to good and reasonable results. In order to find out if the location of the calculation in the model code was disadvantageous, some quantities like vertical velocity and virtual potential temperature were outputted twice. One output directly via the namelist choice of the pre-programmed quantities and the other one by directly writing the quantity for output after the calculation in the code. It could be possible that the quantity is used and overwritten in the simulation process after the storing location in the code. Results show that the location does not reveal considerable differences between, e.g., virtual potential temperature output via the namelist and added virtual potential temperature in the model code. In the end, it was decided to store all the data that is necessary to compute the subgrid and grid-scale fluxes. Moreover, the calculation of the fluxes was also necessary for the StatSim data, because there was only a fixed set of variables available which were most valuable for all project members.

For the StatSim data set, vertical velocity and potential temperature are directly available as averaged quantities. This is only due to an “experiment“ of the conductor of the StatSim and the author of these routines deleted them. Much effort has been put into implementing an averaging routine in the ICON model code for nested simulations. Averaged output is especially important for quantities like vertical velocity or, in general, for quantities that change rapidly during short time frames. Having only snapshots at some point in time weakens the significance of the results. A reference to some existing averaging routines for simulations with one domain was tried to fit to a nested simulation with more than one domain. This routine is deeply rooted in the model, which made it impossible to run it successfully for several domains, even with help from different experts. According to that, the new conducted simulations contain many compromises that had to be made as, e.g., having hourly snapshots instead of averages of the quantities and calculating fluxes with the help of output quantities.

Regarding the step of analysing StatSim data and self conducted simulations with respect to model quality, some problems arose by looking at vertical velocity. It seems to take on unrealistic high values as it would not be expected from meteorological knowledge, mainly valid for the own simulations. This occurrence would have to be partly accompanied by very big horizontal wind speeds, which were not detected during the simulation period. These high values could be explained by difficulties of the model with a general overestimation of wind speeds for coarser resolutions, like it is concluded by Heinze et al. [2017]. Additionally, results of the own simulation data have a temporal resolution of hourly snapshots, instead of averaged values like in case of the "Status Simulation" data. Consequently, this source of uncertainty has to be kept in mind when evaluating results and could have some influence on the perceived differences between the two data sources. However, it should be again noticed that the simulation setup of these two data sets are not totally equal and chosen to be as similar as possible for comparison reasons. Some restrictions with regard to additionally benefit from certain advantages are accepted to be different to the old setup of the $HD(CP)^2$ project. For example, there was an improved ICON model branch available at the beginning of the new simulation run, which already includes modifications by the project members. Accordingly, results are not directly comparable when looking at minimum or maximum values of the quantities, but the overall trend and daily cycle should be similar. Having only temporal snapshots for the new simulation is also due to a wrong executed restart at the first conducted simulation. It was decided to have output every minute and to average afterwards. Results showed a declining potential temperature during daytime, which could not be physically explained. In order to identify the problem, the new simulations contain hourly output of a longer time period which is increased to 32 hours at the end. Compromises had to be made as simulation time and memory are limited. Nevertheless, results show that the model captures the mean flow characteristics satisfactorily, such that both simulation data sets are acknowledged to be suitable for the intended analysis.

Looking at potential temperature fields and domain averaged diurnal cycles, shows that all resolutions are in good accordance and capture the daily cycle well. Also during the frontal passage at 26th April 2013, potential temperature shows a declining temperature for all resolutions in the same manner. Horizontal patterns of potential temperature contours have a different shape for StatSim and own simulation data. Noteworthy is that the domains are not exactly the same, but have a big overlapping area, e.g., around the opencast mines. Horizontal patterns of the turbulent diffusion coefficient for heat fulfill the expectations that they are different for the different resolutions, except for the lowest model level in case of the StatSim. This value has the largest influence on the subgrid fluxes, such that it is of great importance that it looks realistic. When taking domain averaged diurnal cycles of the turbulent diffusion coefficient for heat into account, it is conspicuous that the 156 m resolution of the new simulations shows a much bigger difference to the coarser resolutions than all others. This could be an indication of the closure to behave different in case of the 156 m resolution in comparison to all other resolutions.

Since this thesis is not aiming at analysing ICON model data with regard to a comparison to observations and how good they are in agreement, some papers were consulted that investigated this issue. The most recent paper on that topic is the one of Heinze et al. [2017]. It is also the only one working with real case data of the ICON model so far. They compared ICON model data with other well-established LES models like, e.g., PALM and UCLA-LES. Despite the detection of too high wind speeds for the ICON model, which was already stated above, they also concluded that it simulates temperatures about 2 to 4 K too cold and a too high specific humidity. Generally, ICON profiles seem too stable with too low planetary boundary layer (PBL) heights. Furthermore, it has considerably higher peak sensible heat and latent heat fluxes of about 100 to 200 W/m^2. Thus, ICON provides more energy output at the surface, which can lead to larger thermals, stronger turbulence and a deeper PBL. The surface energy balance largely impacts the properties and time evolution of the PBL, such that errors in the surface fluxes can also be due to errors in the simulation of PBL moisture, temperature and dynamics. Nevertheless, these results could explain the detected uncertainties in, e.g., vertical velocity, but they do not declare the scale inconsistency upon the different resolutions. Scale consistency should always be present, regardless of the quality of the simulations compared to observations.

Although the model captures mean flow characteristics satisfactorily, different model resolutions are not scale consistent. This becomes clear when looking at total heat fluxes as representative for turbulence. They are calculated with the help of grid resolved and subgrid fluxes which should add up to the same total heat fluxes for all resolutions in an ideal case. This can not be explored for the StatSim data by looking at domain averaged height profiles as well as domain averaged time series and horizontal patterns of the different resolutions. An exception is the lowest model level, which results in nearly the same total heat fluxes for all resolutions due to the above stated similar values for the turbulent diffusion coefficient for heat in combination with a small grid resolved flux. Especially the higher levels show differences of sensible heat fluxes of about 100 to 200 W/m^2 between the coarsest and the finest resolution as it was also detected by Heinze et al. [2017]. A different behaviour is visible for the new simulation data. Varying time steps shows different accordance upon the resolutions. Taking the 12 UTC domain averaged height plot of total heat fluxes into account, leads to the conclusion that the resolutions are in good agreement, except for the lower levels. But looking at different height levels and time steps reveals some considerable differences which are also present for the StatSim data. Due to the above stated conspicuousness of the turbulent coefficient for heat in case of the 156 m resolution, total heat fluxes of the new simulations show much smaller values for this resolution compared to the coarser ones. This is primarily visible when looking at the domain averaged temporal development of total heat fluxes for the new simulations. Henceforth, it is not clear if the turbulence closure works better for the 156 m resolution or if it is only different and maybe even the 312 m resolution should be considered as more realistic. The latter idea arises out of theoretical considerations, because it seems that total heat fluxes are getting smaller as the resolution increases and this could result in almost no or very small fluxes when refining the grid further. This would not be physically explainable, because total and sensible heat fluxes are present in the atmosphere and do not vanish by refining the grid size. Due to the analysis and the recommendation of Heinze et al.

[2017] to use the 156 m resolution for assessing turbulent and moist processes when evaluating and developing climate model parameterizations, a conclusion of regarding the highest resolution as the most realistic could be more appropriate. Furthermore, the comparison to observations in Heinze et al. [2017] also pointed out that ICON provides too much energy input at the surface, which leads to an overestimation of turbulence.

Case study analysis of limited areas of the "Status Simulation" data does not lead to a different view on the agreement of total heat fluxes for the resolutions. They were carried out in order to investigate whether the scale inconsistency is only a result of very small domain average values, which are detected when considering the whole domain. Regions of strong total heat flux activities possibly behave different upon the resolutions as the whole domain does. Thus, the subgrid closure possibly works fine for restricted regions, but not for a big data field. But all cases show similar discrepancies throughout the resolutions as the analysis of the whole domain does. Different behaviour of the grid resolved fluxes with respect to the order of the resolutions can be seen, but grid scale fluxes remain small and have not much influence on the total heat fluxes. Hence, it can be concluded that total heat fluxes are also scale dependent for some restricted small areas and this is not only the result of a very small domain average of the whole common domain. Looking at the PDFs of the resolutions for total heat fluxes, proves the scale dependence of the output on the resolutions. They show considerable differences in peak values and also partly a wider range of values for the coarser resolutions, which would be expected from the finest resolution with the biggest amount of grid points and the most accuracy in total heat flux values.

Being able to conclude that the model results are scale dependent reveals the necessity of improving the subgrid scale parameterization as the grid resolved fluxes only depend on prognostic variables. To this end, the understanding of the underlying processes needs to be better and an investigation of the subgrid flux behaviour is advantageous. A wavelet analysis of vertical velocity and potential temperature was conducted and put together to a flux matrix afterwards. This matrix shows the interaction of the fluxes on different scales, but the resulting matrix has to be interpreted carefully. All matrices of all days and resolutions show the same pattern of small values in the upper left corner and big values in the lower right corner. The latter represents the larger scales, whereas the upper left corner shows influences of the small scales. Thus, it can be concluded that the larger scales have the most influence on the subgrid fluxes and not the smaller ones as it is assumed in the K-theory, which is the underlying concept of the subgrid closure used in the ICON model.

The need of a better representation of the subgrid fluxes is made clear several times and since the turbulent diffusion coefficient for heat, K, contains all the adjustable information of turbulence, this quantity has to be analysed in more detail. The finest resolution is assumed to be the most realistic, since it resolves more processes than the coarser resolutions. Thus, this resolution is used as reference for the other resolutions. A method is developed to compute theoretical values for K for the coarser resolutions to result in the same total heat fluxes as for the finest resolution. This could provide further information on the behaviour of the resolutions among each other. Except for the lowest model level of the "Status Simulation" data and the coarsest resolution, all scatter plot comparisons of old K values to new calculated values ($\widetilde{K}$) do not show any usable information. Very high values are reached at a wide range of positive and negative $\widetilde{K}$ without any observable trend or accumulation which was expected to be present. The expectations were two separated accumulations of K vs. $\widetilde{K}$ values that represent the two basic types of subgrid fluxes. One should be the turbulent diffusive type, which is assumed to be parameterized by the Smagorinsky closure and one should be present according to the convective type of turbulence which causes non-traditional turbulence and is assumed not to be parameterized satisfactorily in the closure of the ICON model so far.

Based on all results and conclusions drawn, two hypotheses can be proposed to contribute to an improvement of the turbulent subgrid closure used in the ICON model. The first hypothesis is based on the determination that turbulent heat fluxes are overestimated for the coarser resolutions. Looking at a conceptual energy spectrum for turbulence, all utilized resolutions of the StatSim data lie beyond the scales for which the Smagorinsky closure was originally invented. The mixing length is a measure of the ability of turbulence to cause mixing and it is assumed to be proportional to the grid size in the Smagorinsky closure. Thus, the hypothesis proposes to keep the mixing length constant until a critical value to avoid an overestimation of the total heat fluxes of the coarser resolutions. This critical value can be, e.g., 200 m grid size or a even higher resolution. Different values can be tested in order to have a more reliable declaration of this critical value. Since it was already pointed out that the 156 m resolution is possibly working better for the currently used closure of the ICON model, the proposed value could be realistic. Nevertheless, different values for a constant mixing length have to be tested to investigate the significance of this hypothesis.

The second hypothesis is continuing the considerations regarding the K vs. $\widetilde{K}$ expectations that are already stated above. A closer look at the Smagorinsky closure reveals possible error sources for the calculation of the turbulent diffusion coefficient for heat, which is mainly influencing the subgrid fluxes. It is worked out that the most probable factor influencing this value is the proportionality to the grid size. The Smagorinsky closure determines the fluxes by scale turbulence which is of similar size as the grid spacing and fails in situations when subgrid mixing occurs on scales which are independent of grid resolution (l_{mix}) or if it occurs on several scales. There could be two scales, one with l_{mix} and one which is dependent on grid resolution (l_{con}). The latter one may be related to convection or topographic effects and occurs with a pre-defined probability as this is not always present in the atmosphere. Hence, the problem of not accounting for other scales of subgrid activities within the currently implemented parameterization could possibly be closed with the proposed enhancement of the turbulence closure scheme.

All things considered, this work helped to identify a number of issues, which led to new tasks regarding the handling of the ICON model, such that much effort on non-predictable additional work was needed. The first bigger problem was the not fully comprehensible data available from the "Status Simulation“. Too much basic settings of the simulation were unclear, such that the results were not fully reliable in a way that is necessary for an analysis of the turbulence parameterization scheme. In order to have new data with the knowledge of all underlying fundamentals, it was decided to run own simulations with the ICON model. As the handling of the model is still relatively new for non-inventors and the documentation still lacks of basic information, it was a new challenge to conduct simulations with a manual adjustment to the purposes of this thesis. Several difficulties like having no direct possibility of averaging implemented in the ICON model code and finding the error source for the problem with wrong results of grid resolved fluxes arose. This caused various simulations which all had to underlie the above stated constraints in order to keep the output and memory manageable. The new simulation data shows similar results as for the StatSim data such that it is concluded that the prior data is also usable for the analysis of this thesis. As a result of the execution of ICON model simulations, two hypotheses are proposed. Explicit suggestions for different values and equations for the implementation into the ICON code are stated. Accordingly, further investigations of both hypotheses are realizable in a comprehensive and straightforward way, which are outlined in the following Section 7.2.

7.2 Outlook

The first and most important step for the future would be to test the hypotheses by implementing them into the ICON model code and conducting new simulations similar to the ones that were used before. A good approach would probably be to test hypothesis 1 with different values first and see if this is already improving the results satisfactorily. If not, hypothesis 2 can be tested with the help of the stated equations and to further develop the underlying idea by conducting different simulations with several probabilities. When both or one of the hypotheses emerge to be a good improvement to the data of this thesis, all results should be compared to observations. In order to examine if the improved closure is also appropriate and conferrable to other weather situations, different boundary conditions or other topography can be tested in different setups of simulations. This could increase the significance and reliability of the improved subgrid closure scheme.

For the purpose of further improving the investigations of this thesis, changes of the simulation setup could be made by, e.g., choosing bigger domains or other topography with the objective of having more data and other influences of the ground. Following up on that, it would be very helpful to have data of different weather situations like stable and unstable stratification or a cloudy sky could have another influence on the results. The 26th April 2013 is an example for a convective and cloudy day with rain and a frontal passage, but this is a very special case and other cloudy days, e.g., could lead to a different assessment of the turbulence parameterization. The 26th April 2013 does not give different content to the conclusions as already stated in Section 7.1. An exception for that is the domain averaged diurnal cycle of vertical velocity which seems to be more reliable under the conditions of the frontal passage than for the predominant weather conditions of the 24th April 2013. The turbulent diffusion coefficient for heat, K, or especially the Richardson number (c.f. Section 6.3.4) is dependent on the stratification of the atmosphere. Hence, differences in weather situation could have a distinct influence on the performance of K and the model in general.

To go along with the idea of other modeling conditions, different boundary conditions like no or respectively flat terrain or a constant temperature field reveals more possibilities of testing the old and the improved parameterization in a well known and easier assessable setup. However, it was decided to evaluate real data simulations out of two main reasons. On the one hand, the work for this thesis was part of the $HD(CP)^2$ project, in which the first simulation results should be examined with respect to model performance of the newly developed code. On the other hand, the Smagorinsky parameterization has to operate satisfactorily in real cases and is already well tested for theoretical and ideal cases by many authors.

A critical point that remains especially when interpreting data of the 156 m resolution of the new simulations is the vertical resolution. The "Status Simulation" data had only 50 levels for a 21 km top height of the domain, which was increased to 70 level for the new simulations. But this did not end up with much thinner layers near the ground, even after correcting the so called stretching factor to 0.7 instead of 0.9 (c.f. Figure 10 in Section 4.2). It was also tested to have a lower top height of the modeling domain, but the radiation scheme always had a problem with the last layer and there was not enough time to correct the adjustments to a successful simulation. Accordingly, the top height was retained and further increasing of the number of model levels would have been too time and memory consuming for the available resources. Colleagues of the $HD(CP)^2$ project run simulations with 150 layers in the meantime, which would be a great enhancement of the investigation of this thesis. When looking at the 156 m resolution, it becomes directly clear that with higher altitude, the vertical extend of a grid box gets bigger than the horizontal dimensions which could lead to a wrong behaviour and interactions within the grid box and thus ends up with bad results.

Another improvement for a better basis of the analysis of the parameterization scheme with regard to scale independence would be more and different resolutions. Thinking of a simulation in a numerical weather prediction setup and further decreasing grid size due to some area of special interest is the main driver for the evaluation of this thesis. Hence, it would be very helpful to have also some coarser grid sizes of about 10 km or even bigger and down to about 100 m, what is nearly reached with the 156 m resolution of the new simulations. It is not easy to conduct such a data set with one model and/or with the same area, boundary conditions, etc. in order to have comparable data. The coarsest domain should be simulated with a model in NWP mode and grid refinement or nesting would end in a LES mode. This should be realistically convertible with the help of a switch to other parameterizations etc. with ICON, but to the knowledge of the author this is not sufficiently tested or practicable with the ICON model, yet. Furthermore, this would cost a lot of simulation time, memory and computer capacity, because only bisecting grid size is possible as already described before. This would lead to many resolutions in between the ones of interest and would probably only be realizable in the framework of a big project with enough resources available.

8 Appendix

A.1 – Figures

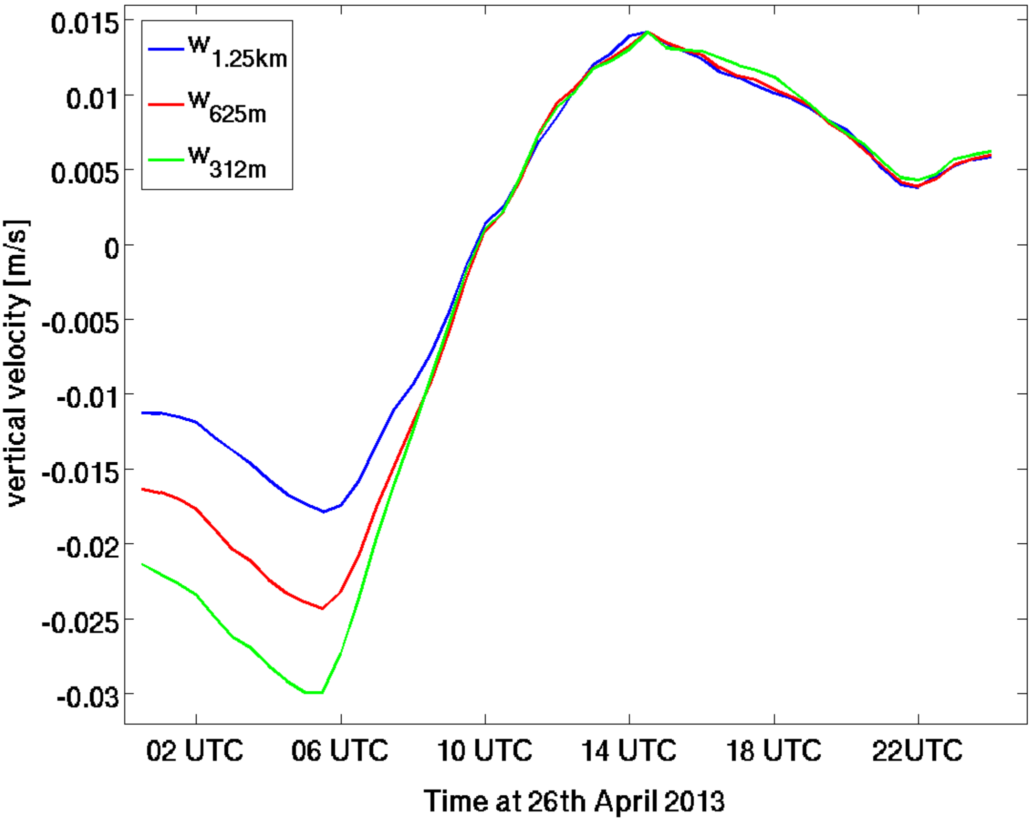

Figure 46. Domain averaged diurnal cycle of vertical velocity, w $[m/s]$, for the "Status Simulation". Shown are all resolutions at 26th April 2013 at 10 m level, 12 UTC. Blue lines indicate the 1.25 km resolution, red shows the 625 m resolution and green shows the 312 m resolution.

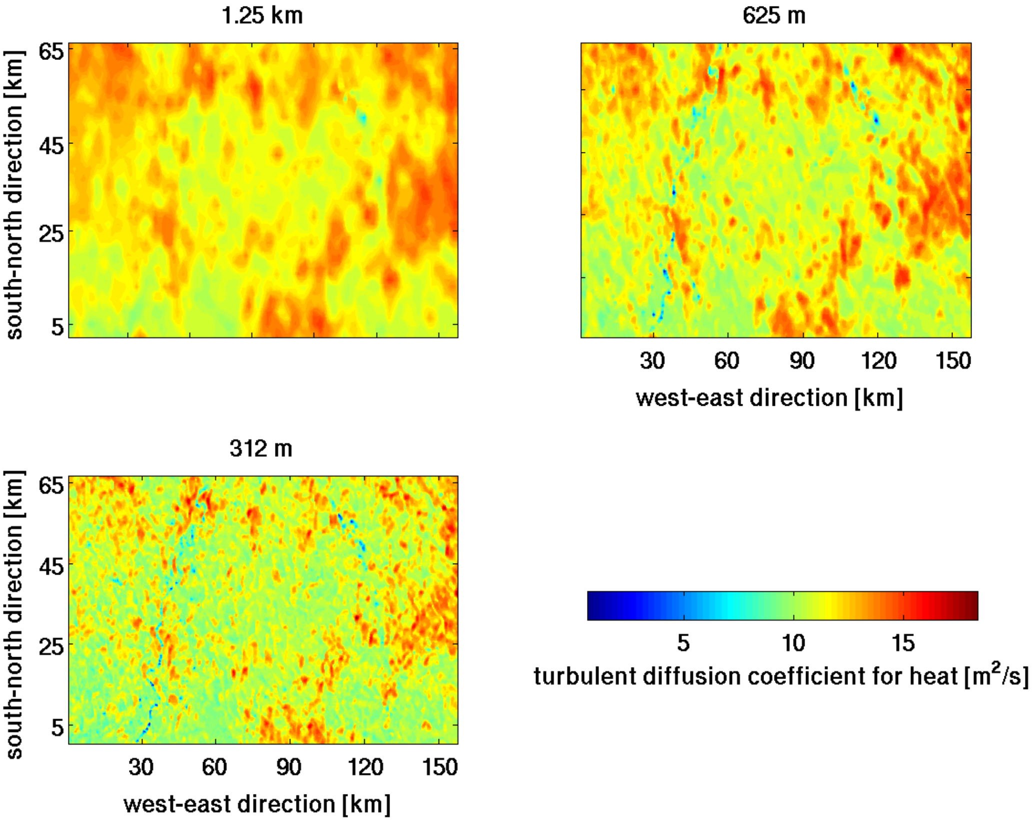

Figure 47. Horizontal patterns of turbulent diffusion coefficient for heat, K $[m^2/s]$, contours of “Status Simulation” data. Shown for are all resolutions at 24th April 2013 at 10 m level, 12 UTC.

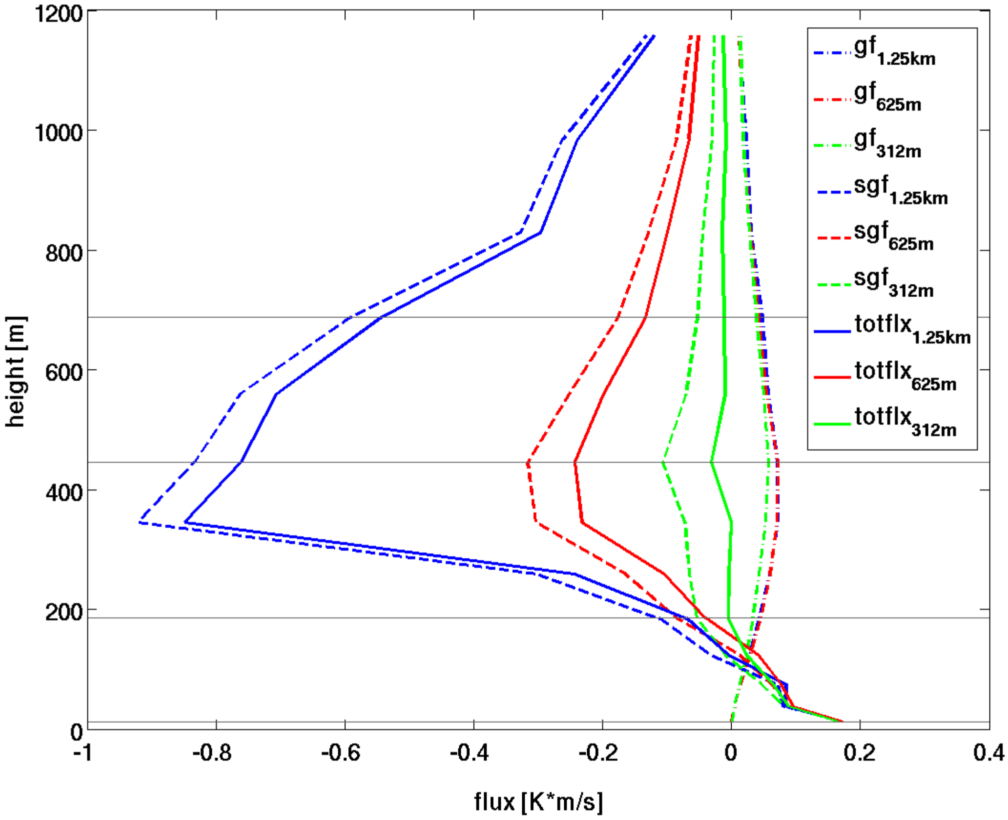

Figure 48. Domain averaged height plot of grid resolved (.-), subgrid (--) and total heat fluxes (-) $[K \cdot m/s]$ for all resolutions at 26th April 2013, 12 UTC. Colors of the different resolutions like in Figure 46.

9 References

R. Berkowicz and L. Prahm. Generalization of k-theory for turbulent diffusion. part 1: Spectral turbulent diffusivity concept. *Journal of Applied Meteorology*, 18:266–272, 1979.

Berliner Wetterkarte e.V. Bodenwetterkarte von 01 uhr mez (europa und nordatlantik). Website, 2015. `http://wkserv.met.fu-berlin.de/archiv/archiv_index.php?current_year=2013`, Accessed: 25.06.2015.

Berliner Wetterkarte e.V. Website, 2016. `http://wkserv.met.fu-berlin.de/archiv/archiv_index.php`, Accessed: 12.10.2016.

A. Blackadar. The vertical distribution of wind and turbulent exchange in a neutral atmosphere. *Journal of Geophys. Research*, 67, No. 8:3095–3102, 1962. doi: 10.1029/JZ067i008p03095.

E. Bou-Zeid, N. Vercauteren, M. Parlange, and C. Meneveau. Scale dependence of subgrid-scale model coefficients: An a priori study. *Physics of Fluids*, 20, 115106, 2008. doi: 10.1063/1.2992192.

B. Burton. Wokingham weather; hrpt and msg satellite image archive. Website, 2006. `http://www.woksat.info/wos.html`, Accessed: 12.10.2016.

P. Davidson. *Turbulence - An Introduction for Scientists and Engineers.* Oxford University Press, 2004.

Deutscher Wetterdienst. Regionalmodell cosmo-de. Website, 2016a. `https://www.dwd.de/DE/forschung/wettervorhersage/num_modellierung/01_num_vorhersagemodelle/regionalmodell_cosmo_de.html`, Accessed: 17.11.2016.

Deutscher Wetterdienst. Icon (icosahedral nonhydrostatic) model. Website, 2016b. `https://www.dwd.de/EN/research/weatherforecasting/num_modelling/01_num_weather_prediction_modells/icon_description.html`, Accessed: 07.07.2016.

A. Dipankar, B. Stevens, R. Heinze, C. Moseley, G. Zängl, M. Giorgetta, and S. Brdar. Large eddy simulation using the general circulation model icon. *Journal of Advances in Modeling Earth Systems*, 7:963–986, 2015. doi: 10.1002/2015MS000431.

G. Doms, J. Förster, E. Heise, H.-J. Herzog, D. Mironov, M. Raschendorfer, T. Reinhardt, B. Ritter, R. Schrodin, J.-P. Schulz, and G. Vogel. *A Description of the Nonhydrostatic Regional COSMO Model, Part II: Physical Parameterization*, 2011.

V. Ermert. Stündliche wetterbeobachtungen deutscher, synoptischer stationen. Website, 2016. `http://www.uni-koeln.de/math-nat-fak/geomet/meteo/winfos/dwdstuendl/index.html`, Accessed: 18.10.2016.

A. Gassmann and H. Herzog. Towards a consistent numerical compressible non–hydrostatic model using generalized hamiltonian tools. *Quaterly Journal of the Royal Meteorological Society*, 65:1597–1613, 2008. doi: 10.1002/qj.297.

M. Germano, U. Piomelli, P. Moin, and W. Cabot. A dynamic subgrid-scale eddy viscosity model. *Phys. Fluids A*, 3, No. 7:1760–1765, 1991. doi: 10.1063/1.2401626.

M. Giorgetta and P. Korn. Icon (icosahedral non-hydrostatic) general circulation model. Website, 2015. `http://www.mpimet.mpg.de/en/science/models/icon.html`, Accessed at 22.01.2015.

M. Giorgetta, G. Zängl, K. Fröhlich, A. Gassmann, M. Köhler, P. Korn, L. Linardakis, S. Lorenz, L. Kornblueh, R. Müller, R. Redler, T. Reinhardt, D. Reinert, P. Ripodas, H. Wan, L. Bonaventura, and M. Restelli. New climate models: The icon modeling system. Max Planck Institute for Meteorology (MPI-M) and German Weather Service (DWD), 2011.

P. Griewank. A conservative scheme for the multi-layer shallow-water system based on nambu representation and the icon grid. Diploma thesis, Institute for Meteorology, University of Berlin, 2009.

$HD(CP)^2$. High definition clouds and precipitation for climate prediction – mission. Website, 2016. `http://hdcp2.zmaw.de/index.php?id=2261`, Accessed: 11.07.2016.

R. Heikes and D. Randall. Numerical integration of the shallow-water equations on a twisted icosahedral grid. part ii: A detailed description of the grid and an analysis of numerical accuracy. *Monthly Weather Review*, 123:1881–1887, 1995a. doi: 10.1175/1520-0493(1995)123⟨1881:NIOTSW⟩2.0.CO;2.

R. Heikes and D. Randall. Numerical integration of the shallow-water equations on a twisted icosahedral grid. part i: Basic design and results of tests. *Monthly Weather Review*, 123:1862–1880, 1995b. doi: 10.1175/1520-0493(1995)123⟨1862:NIOTSW⟩2.0.CO;2.

R. Heinze, A. Dipankar, C. Henken, C. Moseley, O. Sourdeval, and S. T. et al. Large-eddy simulations over germany using icon: A comprehensive evaluation. *Quarterly Journal of the Royal Meteorological Society*, 2017. doi: 10.1002/qj.2947.

J. Hinze. *Turbulence*. McGraw-Hill Book Company, New York, 2nd edition, 1975.

H.-Y. Huang, B. Stevens, and S. Margulis. Application of dynamic subgrid-scale models for large-eddy simulation of the daytime convective boundary layer over heterogeneous surfaces. *Boundary-Layer Meteorology*, 126:327–348, 2007. doi: 10.1007/s10546-007-9239-9.

W. Langhans, J. Schmidli, and B. Szintai. A smagorinsky-lilly turbulence closure for cosmo-les: Implementation and comparison to arps. *COSMO Newsletter*, 12:20–31, 2011.

D. Leuenberger, M. Koller, O. Fuhrer, and C. Schär. A generalization of the sleve vertical coordinate. *Monthly Weather Review*, 9:3683–3689, 2010. doi: 10.1175/2010MWR3307.1.

D. Lilly. On the numerical simulation of buoyant convection. *Tellus*, 14, Issue 2: 148–172, 1962. doi: 10.1111/j.2153-3490.1962.tb00128.x.

D. Lilly. A proposed modification of the germano subgrid-scale closure method. *Phys. Fluids*, A 4:633–635, 1992. doi: 10.1063/1.858280.

L. Linardakis, D. Reinert, and A. Gassmann. Icon grid documentation. *Tech. Report, Max-Planck Institute for Meteorology, Hamburg, Germany*, 2011.

U. Löhnert, J. Schween, C. Acquistapace, K. Ebell, M. Maahn, M. Barrera-Verdejo, A. Hirsikko, B. Bohn, A. Knaps, E. O'Connor, C. Simmer, A. Wahner, and S. Crewell. Joyce: Jülich observatory for cloud evolution. *American Meteorological Society*, 96:1157–1174, 2015. doi: 10.1175/BAMS-D-14-00105.1.

M. Giorgetta – MPI-M Website. Challenges and motivations in developing the icon atmosphere model. Website, 2016. `http://www.mpimet.mpg.de/en/communication/news/focus-on-overview/challenges-and-motivations-in-developing-the-icon-atmosphere-model/`, Accessed: 07.07.2016.

M. Giorgetta, P. Korn and G. Zängl. Icon – developing a new generation of climate and weather forecasting models. Website, 2017. `http://www.mpimet.mpg.de/en/communication/news/focus-on-overview/icon-development/`, Accessed: 27.01.2017.

P. Mason. Large-eddy simulation of the convective atmospheric boundary layer. *Journal of the Atmospheric Sciences*, 46, No. 11:1492–1516, 1989. doi: 10.1175/1520-0469(1989)046⟨1492:LESOTC⟩2.0.CO;2.

C. Meneveau and J. Katz. Scale-invariance and turbulence models for large-eddy simulation. *Annu. Rev. Fluid Mech.*, 32:1–32, 2000. doi: 10.1146/annurev.fluid.32.1.1.

J. Milovac, K. Warrach-Sagi, A. Behrendt, F.Späth, J. Ingwersen, and V. Wulfmeyer. Investigation of pbl schemes combining the wrf model simulations with scanning water vapor differential absorption lidar measurements. *Journal of Geophysical Research*, 121:624–649, 2016. doi: 10.1002/2015JD023927.

E. Mlawer, S. Taubman, and S. Clough. *RRTM: A Rapid Radiative Transfer Model*, 1995.

Namelist Overview. *Guide stored in ICON model folder*, 2015.

P. Peixoto and S. Barros. On vector field reconstructions for semi-lagrangian transport methods on geodesic staggered grids. *Journal of Computational Physics*, 273:185–211, 2014. doi: 10.1016/j.jcp.2014.04.043.

R. Pielke and R. Pearce. *Mesoscale Modeling Of The Atmosphere.* American Meteorological Society, 1994.

R. A. Pielke. *Mesoscale Meteorological Modeling.* Academic Press, 2nd edition, 2002.

S. Raasch and M. Schröter. Palm – a large-eddy simulation model performing on massively parallel computers. *Meteorologische Zeitschrift*, 10, No.5:363–372, 2001. doi: 10.1127/0941-2948/2001/0010-0363.

T. Ruppert. Vector field reconstruction by radial basis functions. Master's thesis, Technical University Darmstadt, 2007. Department of Mathematics.

RWE Power AG. Website, 2016. `http://www.rwe.com/web/cms/de/60026/rwe-power-ag/energietraeger/braunkohle/standorte/tagebau-inden/`, Accessed: 24.10.2016.

A. Seifert and K. Beheng. A double–moment parameterization for simulating autoconversion, accretion and selfcollection. *Atmospheric Research*, pages 265–281, 2001. doi: 10.1016/S0169-8095(01)00126-0.

J. Smagorinsky. General circulation experiments with the primitive equations. i. the basic experiment. *Monthly Weather Review*, 91(3):99–164, 1963. doi: 10.1175/1520-0493(1963)091⟨0099:GCEWTP⟩2.3.CO;2.

G. Smiatek, B. Rockel, and U. Schättler. Time invariant data preprocessor for the climate version of the cosmo model (cosmo-clm). *Meteorologische Zeitschrift*, 17(4):395–405, 2008. doi: 10.1127/0941-2948/2008/0302.

B. Stevens, C.-H. Moeng, and A. A. et al. Evaluation of large-eddy simulations via observations of nocturnal marine stratocumulus. *Monthly Weather Review*, 133:1443–1462, 2005. doi: 10.1175/MWR2930.1.

R. Stull. *An Introduction to Boundary Layer Meteorology.* Kluwer Academic Publishers, 1988.

H. Tomita, M. Saton, and K. Goto. An optimization of the icosahedral grid modified by spring dynamics. *Journ. of Computational Physics*, 183:307–331, 2002. doi: 10.1006/jcph.2002.7193.

TROPOS. Leibniz institute for tropospheric research. Website, 2013. `https://www.tropos.de/en/current-issues/current-measurement-campaigns/hdcp2-hope-2013/`.

Universität Hamburg. Icon-les status simulation. Website, 2017. Figure by A. Lammert, `http://icdc.cen.uni-hamburg.de/1/projekte/hdcp2/model-data/icon-les-status-simulation.html`, Accessed: 03.02.2017.

H. Wan, M. Giorgetta, G. Zängl, M. Restelli, D. Majewski, L. Bonaventura, K. Fröhlich, D. Reinert, P. Ripodas, L. Kornblueh, and J. Förstner. The icon-1.2 hydrostatic atmospheric dynamical core on triangular grids - part 1: Formulation and performance of the baseline version. *Geoscientific Model Development*, 6:735–763, 2013. doi: 10.5194/gmd-6-735-2013.

wetter3.de. Website, 2016. `http://www1.wetter3.de/Archiv/`, Accessed: 12.10.2016.

Wetterzentrale. Website, 2016. `http://www.wetterzentrale.de/`, Accessed: 12.10.2016.

Y.-N. Young, M. Miesch, and N. Mansour. Subgrid scale modeling in solar convection simulations using the ash code. *Center for Turbulence Research*, 2003.

G. Zängl, D. Reinert, P. Ripodas, and M. Baldauf. The icon (icosahedral non-hydrostatic) modelling framework of dwd and mpi-m: Description of the non-hydrostatic dynamical core. *Quaterly Journal of the Royal Meteorological Society*, 141:563–579, 2015. doi: 10.1002/qj.2378.

Acknowledgments

I would like to express my gratitude to my supervisor Prof. Dr. Yaping Shao, who guided me through this challenging research topic and inspired me with many helpful discussions. I appreciate his trust in me for selecting me, besides the work for this thesis, as helping hand in administration operations and budget controlling. I would also like to thank my co-supervisor Dr. Hendrik Elbern, who was very inspiring with helpful input and an always critical view in many discussions. I also thank Dr. Mark Reyers for being observer in the defense of this thesis.

The work for this thesis was funded by the Bundesministerium für Bildung und Forschung (BMBF) within the framework of the $HD(CP)^2$ project, S1, subproject 4 “Multiscale turbulence diagnostics” with ’Föderkennzeichen’ 01LK1213D. I would like to thank especially Dr. Armin Mathes from DLR for the effort he puts in the possibility to extend my subproject. But I also thank all the project members for helpful input and the friendly atmosphere at the annual meetings and also the colleagues from the ICON course in Langen. A special thank goes to Dr. Anurag Dipankar who helped me very much in every question I had regarding the model or the model setup for the “Status Simulation” data I used.

Special thanks go to Dr. Vera Schemann, who provided the initial, external and boundary data for my own simulation with ICON. She also had an open ear at every time for every kind of questions and helped me a lot in solving problems with the model setup and running the simulation. I thank Dr. Michael Hintz for proof-reading this thesis and by this, giving a very useful new perspective on my text. I also thank Dr. Jörg Burdanowitz for proof-reading with a helpful view from an outside prospect. I would like to thank Dr. Sven Ulbrich for many discussions about data analysis and help in every kind of computer problems. Additionally, I want to thank all the group members and colleagues of the institute, who changed from time to time during my work at the institute, for the discussions in group meetings or personally. I thank Ralf

Müller from MPI-M Hamburg for his help in trying to write averaged values in the output and Dr. Patrick Ludwig and Larisa Seregina for providing me with computing time on Mistral at DKRZ Hamburg.

Very special thanks go to my partner Dirk, who motivated and inspired me through all ups and downs I had during this work. I really appreciate his support and his loving way of handling me and my moods. I want to thank my best friend Ramona for motivating and supporting me and for proof-reading this thesis. Last but not least, I want to thank my family and my old and new friends for their support, understanding and many delightful hours throughout these years in a new environment.

Erklärung

Ich versichere, dass ich die von mir vorgelegte Dissertation selbständig angefertigt, die benutzten Quellen und Hilfsmittel vollständig angegeben und die Stellen der Arbeit – einschließlich Tabellen, Karten und Abbildungen – , die anderen Werken im Wortlaut oder dem Sinn nach entnommen sind, in jedem Einzelfall als Entlehnung kenntlich gemacht habe; dass diese Dissertation noch keiner anderen Fakultät oder Universität zur Prüfung vorgelegen hat; dass sie – abgesehen von unten angegebenen Teilpublikationen – noch nicht veröffentlicht worden ist, sowie, dass ich eine solche Veröffentlichung vor Abschluss des Promotionsverfahrens nicht vornehmen werde. Die Bestimmungen der Promotionsordnung sind mir bekannt. Die von mir vorgelegte Dissertation ist von Herrn Prof. Dr. Yaping Shao betreut worden.

Köln, den